Cross-Section Measurement of ^{2}H(n,np)n at 16 MeV in Symmetric Constant Relative Energy Configurations

Alexander Hoff Couture

A dissertation submitted to the faculty of the University of North Carolina at Chapel Hill in partial fulfillment of the requirements for the degree of Doctor of Philosophy in the Department of Physics and Astronomy.

Chapel Hill
2011

Approved by:

T. B. Clegg, Advisor

C. R. Howell, Advisor

H. J. Karwowski, Reader

J. Lu, Reader

J. Engel, Reader

Abstract

ALEXANDER HOFF COUTURE: Cross-Section Measurement of ^{2}H(n,np)n at 16 MeV in Symmetric Constant Relative Energy Configurations. (Under the direction of T. B. Clegg and C. R. Howell.)

The neutron-deuteron (*nd*) breakup reaction serves as a fertile testing ground for theories of three nucleon dynamics and meson exchange descriptions of nuclear systems. The three-body kinematics of the *nd* breakup reaction allow observables to be studied in a variety of exit-channel configurations to test nucleon-nucleon potential models as well as three-nucleon force models. Over the last two decades there have been significant advances in modeling three-nucleon dynamics using empirical nucleon-nucleon potential models [Glö96]. These calculations have shown excellent agreement with most experimental data. However, there remain some exceptions where serious discrepancies arise. We have undertaken new cross-section measurements to provide further insight into one of these discrepancies, the space-star anomaly.

The space-star configuration is a special case of the symmetric constant relative energy (SCRE) configuration in *nd* breakup. The SCRE configuration occurs when the three outgoing nucleons have the same energy and are separated by 120° in the center-of-mass frame. The space-star configuration occurs when the plane containing the outgoing nucleons is perpendicular to the incident beam. The other SCRE configuration measured in this experiment is the coplanar-star, in which this plane contains the incident beam.

The space-star anomaly is a discrepancy between theoretical predictions and experimental measurements for the *nd* breakup differential cross sections; the data are systematically higher than theory at all energies where measurements have been taken. This anomaly has been established by eight previous measurements taken at neutron beam energies of 10.3, 13.0, 16.0, and 25.0 MeV. Three of these experiments were performed in Germany at Bochum [Ste89] and Erlangen [Str89, Geb93], one at the Chinese Institute of Atomic Energy [Zho01], and four at TUNL [Set05, Cro01, Mac04]. All previous measurements were taken with essentially the same experimental setup, the common features being: (1) the scatterer was a deuterated scintillator, (2) two neutrons were detected in coincidence, (3) the target-beam integrated luminosity was determined through *nd* elastic scattering by detection of the scattered neutron. To determine if there could be a common experimental error in previous measurements, our experiment utilizes a technique similar to the one developed by Huhn *et al.*[Huh00b] to mea-

sure the nn scattering length. The primary distinctions between our technique and those used in previous SST measurements are: (1) the deuterated target was a thin foil, (2) a neutron was detected in coincidence with the scattered proton, and (3) the integrated target-beam luminosity was determined by nd elastic scattering via detection of the scattered deuteron.

To compare the results of this experiment with theoretical predictions, a Monte-Carlo simulation of the experiment was developed which averaged point-geometry Faddeev calculations over the finite geometry of the experimental apparatus [Taj10]. Along with this averaging process several other effects were simulated including: the energy loss and attenuation of charged particles in our system, background events from low energy neutrons in the beam, the time resolution of the detectors and electronics, and kinematic constraints in breakup events. The effective experimental cross section produced by the Monte-Carlo simulation was then used to predict the number of counts expected as a function of detected neutron energy which could be directly compared with the experimental measurement. This method has the advantage that statistical and systematic uncertainties are clearly separated between experimental measurement and theoretical prediction, respectively.

Table of Contents

List of Tables

List of Figures

1 Introduction

Models of the nuclear force naturally begin by considering the interaction between a pair of nucleons. An extensive compilation of proton-proton (pp) and neutron-proton (np) scattering observables has been cataloged over the last half century. Pure neutron-neutron (nn) observables are lacking since neutron targets have not been developed. Nuclear force models are tailored to describe these two-nucleon (2N) observables. The first logical place to test these models is the three-nucleon (3N) system; the nd system, in particular, is ideal since the Coulomb interaction is not present, leaving the nuclear interaction as the dominant effect.

There are three classes of reactions which may occur from an nd interaction: elastic scattering, neutron capture forming a triton, and the breakup of the deuteron. A measurement of the five-fold differential cross section, $d^5\sigma/d\Omega_p d\Omega_n dE_n$, for the neutron-induced deuteron (nd) breakup reaction, $^2H(n,np)n$, taken at an incident neutron energy of 16.0 MeV forms the basis of this thesis. This chapter will first discuss the kinematics of the breakup reaction and describe the exit-channel configurations studied. The problems that have been encountered in calculating 3N observables will then be addressed. The history of nd breakup measurements which motivated this experiment will conclude the chapter.

1.1 Experimental Overview

The three-body kinematics of nd breakup allow the outgoing nucleons to arrange themselves in a wide variety of exit-channel configurations, restricted only by conservation of energy and momentum. This provides a fertile testing ground for the application of nucleon-nucleon (NN) potential models as well as three-nucleon forces (3NF). The cross sections for two particular exit-channel configurations, both representative of the symmetric constant energy (SCRE) configuration depicted in Figure 1.1, were explicitly investigated. These were the

space-star configuration (SST) and the coplanar-star configuration (CST). Here, the SCRE configuration of nd breakup is defined as an exit channel where the momentum vectors of the three outgoing nucleons have the same magnitude and lie in a common plane separated by 120° in the center-of-mass (CM) frame. The SST configuration occurs when this plane is perpendicular to the incident neutron beam axis. In the CST configuration, this plane contains the beam axis.

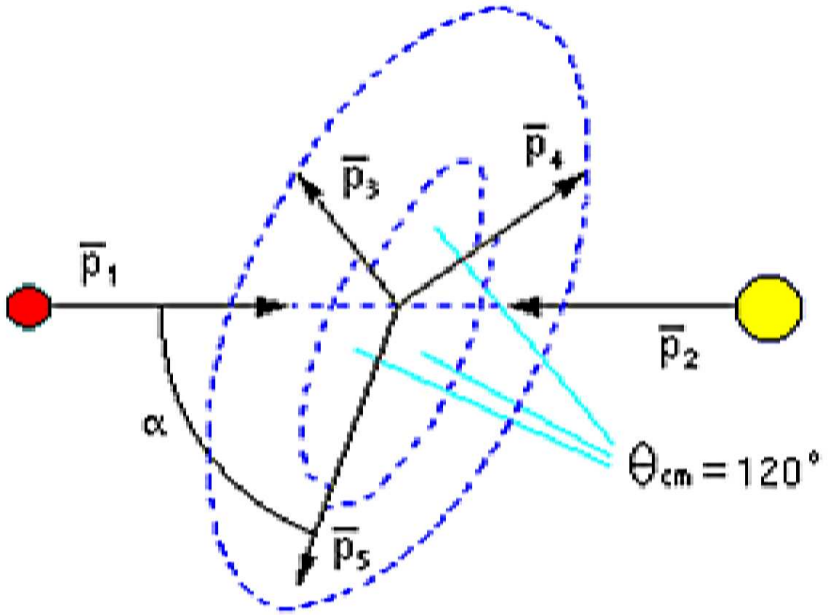

Figure 1.1: Diagram of the symmetric constant relative energy configuration of nd breakup. In the center-of-mass frame, the momentum vectors of the three outgoing nucleons have the same magnitude, lie in a plane, and are separated by 120°. The angle defining the tilt of the scattering plane with respect to the incident neutron beam axis is denoted as α. For the SST(CST) configuration, $\alpha = 90°(\alpha = 0°)$.

The kinematics of the 3N system are specified by nine degrees of freedom, the three components of each nucleonic momentum vector. When considering the final state of the nd breakup reaction, four of these components are restricted by energy and three-dimensional momentum conservation. These are characterized by the initial state which in the laboratory frame is described by a neutron traveling along the beam axis with a specific energy and a stationary deuteron with a binding energy of 2.224 MeV. The remaining five parameters are typically specified by the energies and polar angles with respect to the neutron beam axis, E_1, θ_1, E_2 and θ_2, for two of the outgoing nucleons and the azimuthal separation between them, ϕ_{12}. The knowledge of these nine parameters completely specifies the final state, with one caveat:

since the initial state possesses azimuthal symmetry about the neutron beam axis, the final state must as well. Thus any description of the final three-nucleon configuration must be independent of rotations about this axis.

In performing a kinematically complete *nd* breakup measurement, two detectors are placed in specific positions relative to the target, and the neutron beam energy is controlled. In any coincidence between outgoing detected nucleons following a collision which causes a target deuteron to break up, the outgoing nucleons must have energies which lie along a well-defined kinematic locus or S-curve in the $E_1 - E_2$ plane, as shown in Figure 1.2. This kinematic locus may be parameterized by an arc length, S, defined such that it increases counterclockwise and S=0 is located at the maximum value of E_1 where the locus intersects the E_1 axis. There are configurations where the locus never intersects this axis; in this case S=0 is defined as the point on the locus where the sum, $E_1 + E_2$ is minimized. Two sample loci pertaining to these two conditions are included in Figure 1.2.

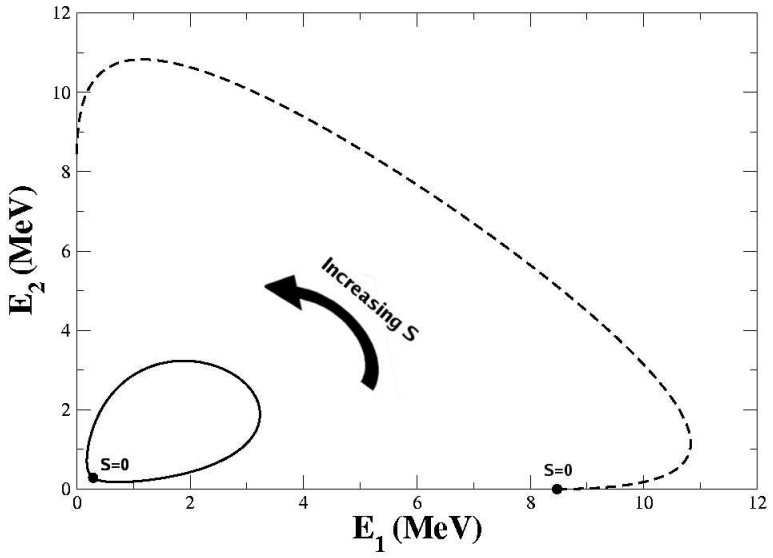

Figure 1.2: Examples of *nd* breakup kinematic loci for an incident neutron beam energy of 16 MeV. The dots show the location of S=0 for the two configurations. The configuration shown by the solid line corresponds to the angles $\theta_1 = \theta_2 = 35°$ and $\phi_{12} = 180°$ and obviously does not intersect the E_1 axis. Its S=0 location is defined by the minimization of $E_1 + E_2$. The configuration shown by the dashed line corresponds to the angles $\theta_1 = \theta_2 = 70°$ and $\phi_{12} = 180°$. Here S=0 is defined by the E_1 intercept. In both cases S increases counterclockwise.

1.2 The Three-Nucleon Problem

The interaction between two nucleons has been well characterized over the last half century. Phenomenological NN potential models based on meson exchange, such as the CD-Bonn [Mac01a], the AV18 [Wir95], and Nijmegen [Sto94] potentials, describe two-nucleon (2N) systems with extreme accuracy. When these models are applied to 3N systems in a pairwise fashion, the results agree well with experimental observations in most cases. However, there are some notable exceptions: the triton binding energy defect, the nucleon-deuteron analyzing power puzzle, and the space-star anomaly. Attempts have been made, with varying degrees of success, to resolve these problems with the inclusion of a 3NF. A 3NF is an interaction between the three nucleons which cannot be reduced into iterations of 2N interactions. Notable 3NF models include the Tuscon-Melbourne [Coo79], the Urbana [Car83], and Brazil [Coe83] models, all of which have been updated several times since their initial formulations. The triton binding energy defect and the analyzing power puzzle will be summarized in this section, while the space-star anomaly will be discussed extensively in the next.

Potential Model	Binding Energy (MeV)	
	^{3}H	^{3}He
AV18	7.624	6.925
Nijm II	7.651	6.994
CD-Bonn	7.998	7.263
AV18+UIX	8.479	7.750
CD-Bonn+TM	8.474	7.720
Exp. Value	8.482	7.718

Table 1.1: Calculations of the ^{3}H and ^{3}He binding energies using the hyperspherical harmonic variational method [Kie08] with various phenomenological NN and 3NF potentials.

The binding energy of the triton (^{3}H) has been experimentally determined to be 8.482 MeV. Calculations of the ^{3}H binding energies using modern NN phenomenological potentials have been performed by several different methods [Kie08]. All such potentials fit the Nijmegen phase shift data to about the same level of precision [Mac01a]. Calculations made with the CD-Bonn potential come closer to the ^{3}H binding energy than many of the other modern potential models, however the CD-Bonn model still underbinds the triton by about 0.5 MeV. The inclusion of the most recent version of the TM 3NF [Coo01] with the CD-Bonn potential reproduces the binding energy exactly using the Faddeev method [Nog03]. The combination of the AV18 with the Urbana IX 3NF [Pie01] yields similar results. This is not surprising since the free parameters in these 3NF's are specifically tailored to reproduce this binding energy. However, when these NN+3NF models are used to calculate the binding energy of ^{3}He nucleus, the results reproduce the experimental value to better that 0.5%. A summary

of calculated ^{3}H and ^{3}He binding energieg is included in Table 1.1.

The nucleon-deuteron (Nd) analyzing power puzzle is defined by the failure of rigorous 3N calculations to reproduce experimentally measured Nd vector analyzing powers (A_y) for elastic scattering at low energies [Tor08]. The observable A_y is a measure of the difference in differential cross section when a nucleon beam is in a spin-up versus a spin-down polarization state. The following equation defines $A_y(\theta)$:

$$A_y(\theta) = \frac{\frac{d\sigma}{d\Omega}_{\uparrow}(\theta) - \frac{d\sigma}{d\Omega}_{\downarrow}(\theta)}{\frac{d\sigma}{d\Omega}_{\uparrow}(\theta) + \frac{d\sigma}{d\Omega}_{\downarrow}(\theta)}, \tag{1.1}$$

where the up and down arrows indicate the spin state of the fully polarized nucleon beam. At energies below 16 MeV, theoretical calculations underpredict the maximum value of $A_y(\theta)$ by 20-30%. The choice of NN potential model and the inclusion of a 3NF have only minor effects on these discrepancies. The A_y puzzle diminishes as the incident nucleon energy increases past 16 MeV until it vanishes at about 40 MeV, where NN calculations agree with data. Figure 1.3 illustrates the A_y puzzle below 16 MeV.

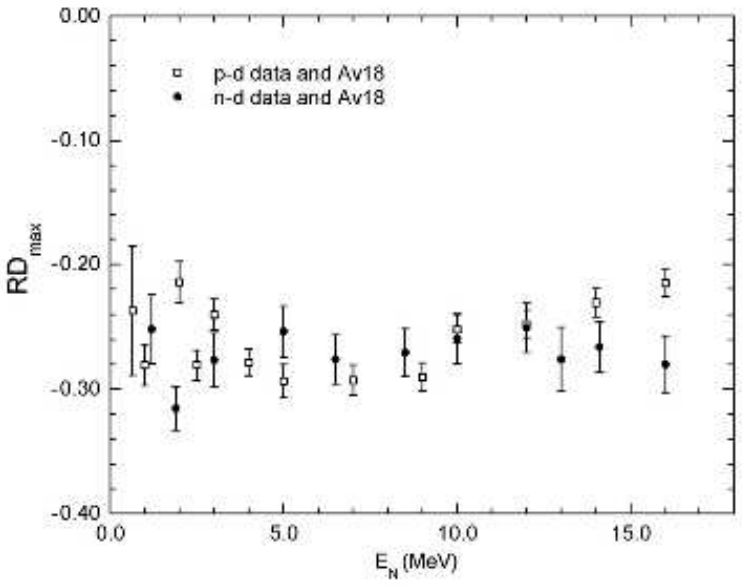

Figure 1.3: Relative difference between vector analyzing power data and theoretical predictions based on the AV18 potential at the angle where A_y is at its maximum value for that energy [Tor08]. The solid dots and open squares represent neutron and proton discrepancies, respectively.

A major issue with all modern phenomenological NN interaction models and their 3NF

corrections is that they treat the nucleons as elementary particles. Nucleons are actually composite systems consisting of quarks interacting via the exchange of gluons. The interactions between quarks and gluons are described by the strong theory of quantum chromodynamics (QCD). Nuclear systems should be described using QCD through the residual strong interaction between nucleons in a fashion similar to the van der Waals forces between neutral molecules. However, the strong coupling constant, α_S, between the quark and gluon fields is too large to allow perturbative calculations to be made in the low-energy regime of nuclear systems [Epe09]. A low-energy approximation of QCD, which treats nucleons and pions as the effective degrees of freedom, known as chiral effective field theory (χEFT), has been developed over the past twenty years. In the framework of χEFT, 3NF's arise naturally and potential models based on this theory have been implemented in 3N calculations [Epe06]. However, chiral potentials have yet to resolve completely either the A_y puzzle or the space-star anomaly.

1.3 Motivation

The space-star anomaly in nd breakup is a discrepancy between theoretical predictions and experimental measurements of the five-fold differential cross section, $d^5\sigma/d\Omega_1 d\Omega_2 dS$. The data are systematically higher than theory at all energies where measurements have been made. This anomaly has been established by eight previous measurements taken at incident neutron beam energies of 10.3, 13.0, 16.0, and 25.0 MeV. Three of these experiments were performed in Germany at Bochum [Ste89] and Erlangen [Str89, Geb93], one at the Chinese Institute of Atomic Energy [Zho01], and four at TUNL [Set05, Cro01, Mac04]. Figure 1.4 shows the history of these SST cross-section measurements compared with Faddeev calculations [Glö96] based on the CD-Bonn potential [Mac01a]. Another notable discrepancy in nd breakup occurs in neutron-neutron (nn) quasifree scattering (QFS), a configuration where the proton is left at rest after the breakup reaction. Cross-section data for nn QFS have been taken at beam energies of 25.0 [Rua07] and 26.0 MeV [Sie02]. Theoretical calculations fall short of the data by about 20% in both these measurements.

All previous measurements were taken with essentially the same experimental setup, the common features being: (1) the scatterer was a deuterated scintillator allowing the energy of the outgoing proton to be measured, (2) the two outgoing neutrons were detected in coincidence, and (3) the target-beam integrated luminosity was determined through $^2H(n,n)^2H$ elastic scattering. By measuring the momentum of the two neutrons and the energy of the recoil proton, this technique over constrained the kinematics of the reaction. To determine if there could be a common experimental error in previous measurements and alter the sensitivity of the data to systematic uncertainties, our experiment utilizes a technique similar to the one developed by Huhn *et al.* [Huh00a, Huh00b] to measure the nn scattering length. This

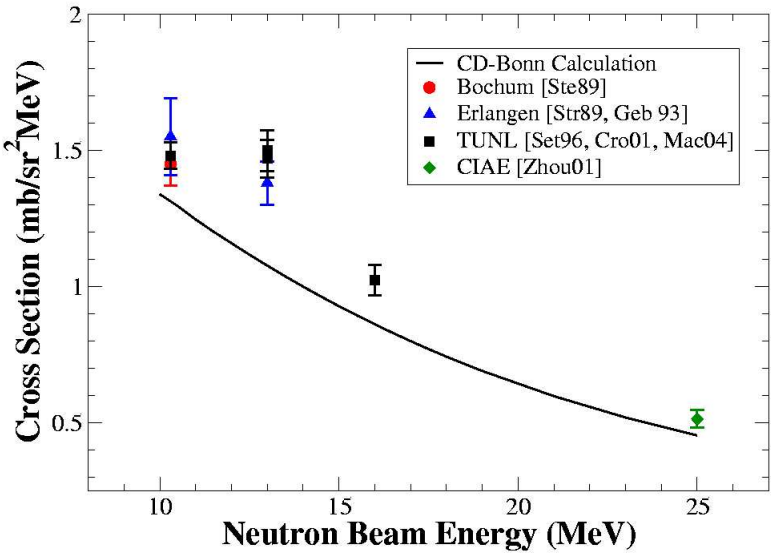

Figure 1.4: History of previous nd breakup space-star cross-section measurements. Measurements have been made at 10.3, 13.0, 16.0, and 25.0 MeV incident neutron energy. All measurements reported on this graph detected the two neutrons in coincidence.

method fully determines the kinematics of the reaction, but does not have redundant kinematic measurements as is the case in the previously used method. The primary distinctions between our technique and those used in previous SST measurements are: (1) the deuterated target was a thin CD_2 foil allowing the outgoing proton to exit the target, (2) the outgoing proton was detected in coincidence with one of the neutrons, and (3) the integrated target-beam luminosity was determined by $^2H(n,d)n$ elastic scattering. Previous measurements as well as most theoretical calculations report the breakup cross section as a function of S. This is advantageous, as an S-value uniquely defines an exit channel while an E_n or E_p value may correspond two different channels. The choice of reporting the results of this experiment as a function of E_n was spurred by the relatively poor proton energy resolution obtainable using our experimental technique. The resolution of the proton energy measurement is mostly determined by the thickness of the CD_2 target foil. Projecting the data onto the detected neutron energy axis removes most of the experimental uncertainty from poor proton energy resolution.

The previous $^2H(n,nnp)$ SST cross sections measured were all flat along the S-curve in the region of the SCRE condition. This allows the measured cross section to be averaged over a relatively large region. Measurements of the $^2H(n,np)n$ SST cross section sample a

different region of the reaction phase space at locations on the S-curve other than the SST point. Therefore, the region along the S-curve over which the SST data may be averaged is more restrictive than for the two-neutron coincidence method. The asymmetry introduced by final-state interactions between the undetected neutron and the proton on one side of the SCRE condition and the two neutrons on the other skews the cross section. The SCRE condition is the only point which may be compared between the current measurement and the previous 16 MeV SST measurement of A. Crowell [Cro01]. Figure 1.5 shows the calculated cross sections as a function of length along the S-curve at 16.0 MeV for the two experimental techniques as well as the experimental results from Crowell.

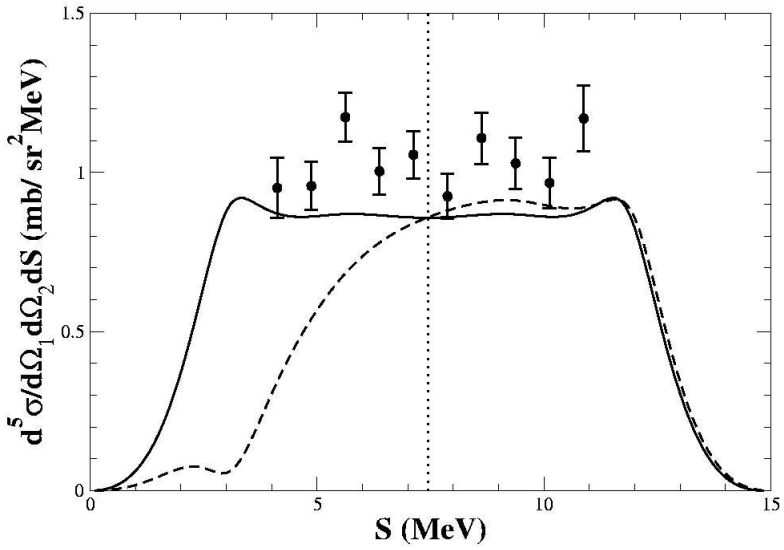

Figure 1.5: Cross sections for *nd* breakup in the SST configuration. Data points are measurements from the *nn* coincidence experiment performed by A. Crowell [Cro01]. The solid line is a theoretical point geometry calculation for his experiment based on the CD-Bonn [Mac01a] potential. The dashed line similarly gives the cross-section calculation for an *np* coincidence measurement of the same reaction. The vertical dotted line shows the location of the SCRE condition, the only place where the *nn* and *np* cross sections are identical and may be compared.

Many of the experiments mentioned above which measured SST cross sections also made CST measurements simultaneously, also by detecting the two neutrons in coincidence. Coplanar star data have been taken at incident neutron energies of 10.3 MeV [Mac04], 13.0 MeV [Mac04, Set05, Str89], and 16.0 MeV [Cro01]. Unlike the SST configuration, which contains complete

symmetry as the three outgoing nucleons are rotated about the axis perpendicular to the plane containing them, the CST configuration obeys no such symmetry. Even in the CM frame, the slight mass difference between protons and neutrons breaks this symmetry. When observed in the laboratory frame, these rotations of the CST produce vastly differing results. The CST experiments listed above have all measured either two neutrons detected symmetrically about the beam axis [Cro01, Mac04] or the scenario where one neutron exits the reaction perpendicular to the beam axis in the CM frame and the other at a more forward angle [Set05, Str89]. This latter choice is advantageous as a neutron detector may be shared by both the SST and CST measurements and the neutron at the forward angle will have greater energy in the laboratory frame allowing a larger kinematic region to be probed. A comparison of laboratory cross sections and kinematic loci for these two scenarios at an incident neutron energy of 16 MeV is shown in Figure 1.6. The CST configuration measured in the current experiment is similar to this latter configuration differing only in that the proton shares its detector with the SST configuration. Unfortunately the 16 MeV $^2H(n,nnp)$ CST measurement [Cro01] was made in the symmetric scenario; thus the results may not be directly compared with the present measurement. However, the 16 MeV beam energy of this experiment explores kinematic regions unavailable to the previous 13 MeV asymmetric CST measurements [Set05, Str89].

The remainder of this thesis will consist of five additional chapters. In the first of these, Chapter 2, various nuclear potential models will be discussed, along with the methods used to make 3N cross-section calculations with them. The following chapter will discuss the experimental setup. Monte-Carlo simulations were required to take the theoretical calculations based upon point geometry and apply them to the experimental setup. These simulations will be addressed in Chapter 4. The details of the data analysis applied to this experiment will then follow in Chapter 5. The final chapter will present the experimental results and discuss their implications.

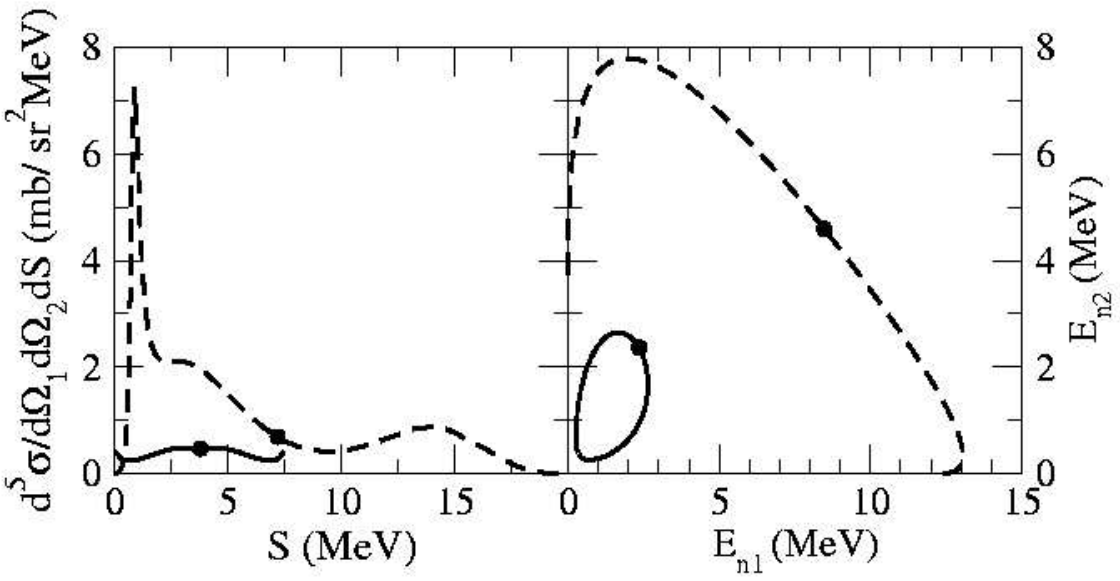

Figure 1.6: Comparison of CST configurations with incident neutron beam energies of 16 MeV rotated by 30° from one another about an axis perpendicular to the plane of the outgoing nucleons in the CM frame. The graph on the left compares the differential cross sections as a function of S. The graph on the right compares kinematic loci. The solid line corresponds to the configuration where the two outgoing neutrons are symmetric about the beam axis ($\theta_{n1} = \theta_{n2} = 71.2°$, $\phi_{12} = 180°$). The dashed line is for the configuration where the momentum of one of the outgoing neutrons is perpendicular to the beam axis in the CM frame and the other is at a forward angle ($\theta_{n1} = 51.5°$, $\theta_{n2} = 16.8°$, $\phi_{12} = 180°$). The solid dots indicate the locations of the SCRE condition.

2 Theoretical Background

2.1 Introduction

Theoretical cross sections were produced to compare with the results of this experiment. In order to do this, one must begin with a model of the interaction between the nucleons involved in the *nd* breakup reaction. A number of high-precision nucleon-nucleon potential models are currently available, as well as models which include three-nucleon forces (3NF). The Charge-Dependent Bonn (CD-Bonn) potential [Mac01a] was used for the brunt of theoretical predictions used in this project; however calculations were made with many other models as well for comparison.

Once a potential model is selected, it must be inserted into the Faddeev equations [Fad61] which are essentially a three-body extention of the Lippmann-Schwinger equation [Lip50] in order to obtain transition (T) matrix elements. The Faddeev equations may not be solved analytically, so numerical calculations were performed by Henryk Witała of the Bochum-Cracow theory group [Glö96]. Theoretical cross sections may then be derived rather simply from the T-matrix.

This chapter will begin with a discussion of various potential models used to describe the nuclear interaction. This will be followed with an explanation of two- and three-body scattering theory and the calculation of the T-matrix. It will conclude with the procedure for obtaining cross sections for three-nucleon processes.

2.2 Potential Models

Any potential model attempting to simulate the nuclear force must replicate the empirical features of this interaction which have been experimentally determined since the discovery of

the atomic nucleus nearly a century ago. Five of the most important features will now be presented [Mac89].

1. *The nuclear interaction has a finite range.* Since electromagnetic forces alone successfully describe observed phenomena on a molecular level, the nuclear force must have a significantly shorter range than interatomic distances. However a more restrictive limit may be placed on the range of this interaction by examining the binding energy of nuclei. Above A=4, the binding energy per nucleon remains relatively constant as well as their density. This indicates that nucleons are only interacting with their nearest neighbors in a nucleus to first order. Based upon the evidence that the energy per bond in light nuclei (A$\leq$4) does increase with A, the range of the nuclear interaction has been estimated to be roughly equal to the radius of the alpha particle (r$\approx$1.7 fm) [Wig33].

2. *The nuclear interaction is attractive in its intermediate range.* The evidence for this postulate is most clearly illustrated by the existence of atomic nuclei containing multiple nucleons. There must be some attractive interaction between nucleons because of these bound systems. The phrase "intermediate range" is meant relative to the entire range of the nuclear force. The nuclear interaction can not be described by a single process over its entire range, thus it is advantageous to subdivide it into different regions. A division of the nuclear force into three regions was proposed by Taketani, Nakamura, and Sasaki [Tak51]. They proposed short ($r \leq 1\ fm$), intermediate ($1\ fm \leq r \leq 2\ fm$), and long ($r \geq 2\ fm$) range regions. Additional evidence of an intermediate range attractive interaction comes from the analysis of low energy NN scattering which indicates positive S-wave phase shifts [Arn83].

3. *The nuclear interaction has a repulsive core.* Evidence of this is also derived from S-wave NN phase shifts. High energy scattering probes more deeply into the core of the nucleon. At laboratory energies above 250 MeV, the S-wave phase shifts become negative indicating repulsion [Arn83]. This range of the repulsive region is estimated to be about 0.6 fm.

4. *The nuclear interaction contains a tensor component.* The most compelling evidence for a tensor force in the nuclear interaction comes from the deuteron wavefunction. A tensor force which mixes the D- and S-wave components of the nuclear interaction is required to explain the quadrupole moment of the deuteron wavefunction [Kam83]. Additional evidence for the tensor component comes from the non-zero magnetic moment of the deuteron [Pri47].

5. *The nuclear interaction contains a spin-orbit component.* Once again evidence of this property comes from the phase shift analysis of NN scattering [Arn83]. The high energy triplet P-waves can only be reproduced by the inclusion of a spin-orbit interaction along

with the central and tensor components. For completeness, it should be mentioned that nuclear interaction should also include spin-spin terms though they are considerably weaker than the other terms.

2.2.1 Meson Exchange Theory

Any discussion of meson exchange theory must begin with the work of Hideki Yukawa who developed a theory to explain the finite range of the nuclear force [Yuk35]. He postulated that the interaction field between the proton and neutron was mediated by a heavy particle. He developed this theory by analogy with quantum electrodynamics (QED) where the force carrier is the massless photon. Let's begin by examining the Poisson equation of classical electromagnetism for a point charge, e, fixed at the origin:

$$\nabla^2 V(\mathbf{r}) = -e\delta^3(\mathbf{r}). \tag{2.1}$$

The solution to this equation is the Coulomb potential with infinite range, given as follows:

$$V(\mathbf{r}) = \frac{e}{4\pi}\frac{1}{r}. \tag{2.2}$$

Yukawa introduced a wave equation for the nuclear potential, U($\mathbf{r}$,t), containing two constants, g and λ, having the units of electric charge ($\mathrm{m}^{\frac{3}{2}}\mathrm{kg}^{\frac{1}{2}}/\mathrm{s}$) and m^{-1}, respectively. It is given by the following:

$$\left\{\nabla^2 - \frac{1}{c^2}\frac{\partial^2}{\partial t^2} - \lambda^2\right\} U = -g\tilde{\Psi}\frac{\tau_1 - i\tau_2}{2}\Psi. \tag{2.3}$$

Here τ_i denotes the Pauli matrices and Ψ is the wavefunction of the nucleons and is a function of time, positions, spin, and isospin. In the limit of heavy, non-relativistic nucleons located at $\mathbf{r}_1$ and $\mathbf{r}_2$ this equation is satisfied by the Yukawa potential [Yuk35]:

$$U(r) = \frac{g}{4\pi}\frac{e^{-\lambda r_{12}}}{r_{12}}\frac{(\tau_1 - i\tau_2)}{2}. \tag{2.4}$$

Here r_{12} is the distance between the nucleons and the Pauli matrices act to transform neutron to proton and vise versa. This potential has a range given by λ^{-1} and predicts a bosonic force carrier with a charge of $\pm e$ and a mass given by $m = (h/c)\lambda$.

The particle predicted by Yukawa was eventually discovered and named the pion (π). Initial potential models involving one-pion exchange were moderately successful at describing NN scattering data and the properties of the deuteron [Mac05]. However, when attempts were made to describe short-range NN interactions using multi-pion exchange models, serious difficulties were encountered [Bru53]. The large πNN coupling ($\frac{g^2}{4\pi} = 13.6$) constant makes unfeasible a perturbative treatment of the nuclear force analogous to QED ($\frac{e^2}{4\pi} = \frac{1}{137}$).

In the 1960's, heavy mesons were discovered that behaved as multi-pion resonances with definite masses and quantum numbers, the ρ and ω being 2π and 3π resonances, respectively. Additional fictitious mesons were conjectured to account for uncorrelated multi-pion exchanges [Mac89]. These advances led to the development of one-boson exchange (OBE) potential models which described empirical NN properties with a good deal of success in the 1970's and 1980's. These potentials begin with Lagrangians characterizing the meson-nucleon couplings by their various symmetries. These Lagrangians for the scalar (s), pseudoscalar (ps), vector (v), and tensor (t) fields are given as follows [Oga67]:

$$\begin{aligned}
\mathcal{L}_s &= g_s \overline{\Psi}\Psi\phi^{(s)}, \\
\mathcal{L}_{ps} &= g_{ps}\overline{\Psi}i\gamma_5\Psi\phi^{(ps)} + \frac{f_{ps}}{M}\overline{\Psi}i\gamma_5\gamma_\mu\Psi\partial_\mu\phi^{(ps)}, \\
\mathcal{L}_v &= g_v\overline{\Psi}i\gamma_\mu\Psi\phi_\mu^{(ps)} + \frac{f_v}{2M}\overline{\Psi}\sigma_{\mu\nu}\Psi\left(\partial_\mu\phi_\nu^{(v)} - \partial_\nu\phi_\mu^{(v)}\right), \\
\text{and } \mathcal{L}_t &= \frac{g_t}{2M}\left\{\overline{\Psi}\gamma_\mu\partial_\nu\Psi - \partial_\nu\overline{\Psi}\gamma_\mu\Psi\right\}\phi_{\mu\nu}^{(t)} + \frac{f_t}{M^2}\partial_\mu\overline{\Psi}\partial_\nu\Psi\phi_{\mu\nu}^{(t)}.
\end{aligned} \tag{2.5}$$

Here M is the nucleon mass and Ψ is the nucleon wavefunction. Wavefunctions for spin 0, 1, and 2 mesons are given by ϕ, ϕ_μ, and $\phi_{\mu\nu}$, respectively. The following definitions apply for the Dirac γ-matrices:

$$\sigma_{\mu\nu} = \frac{1}{2i}\left(\gamma_\mu\gamma_\nu - \gamma_\nu\gamma_\mu\right),$$

$$\gamma_0 = \begin{pmatrix} i & 0 \\ 0 & -i \end{pmatrix},\ \gamma_k = \begin{pmatrix} 0 & -i\sigma_k \\ i\sigma_k & 0 \end{pmatrix}(k = 1,2,3),\ \text{and } \gamma_5 = \begin{pmatrix} 0 & -1 \\ -1 & 0 \end{pmatrix}. \tag{2.6}$$

The first-order contributions to the NN interaction from OBE are described by the Feynman diagram in Figure 2.1. The corresponding amplitude for this process is given as follows:

$$\mathcal{A}_B\left(q', q\right) = \frac{\overline{u}_1(q')\Gamma_1^{(B)}u_1(q)P_B\overline{u}_2(-q')\Gamma_2^{(B)}u_2(-q)}{k^2 - m_B^2}. \tag{2.7}$$

Here $\Gamma_i^{(B)}$ are vertices derived from the Lagrangians of Equation 2.5, the u_i are Dirac spinors for the nucleons, and P_B divided by the denominator is the meson propagator. These amplitudes may be used to produce the following OBE potential [Mac01b]:

$$V(q', q) = \frac{M}{\sqrt{(M^2 + q^2)(M^2 + q'^2)}}\sum_B i\mathcal{A}_B(q', q)F(\mathbf{k}^2). \tag{2.8}$$

Here M is the nucleon mass and a form factor $F(\mathbf{k}^2)$ is used to account for the extended structure of the nucleon and conceal a singularity at the origin. Several examples of commonly

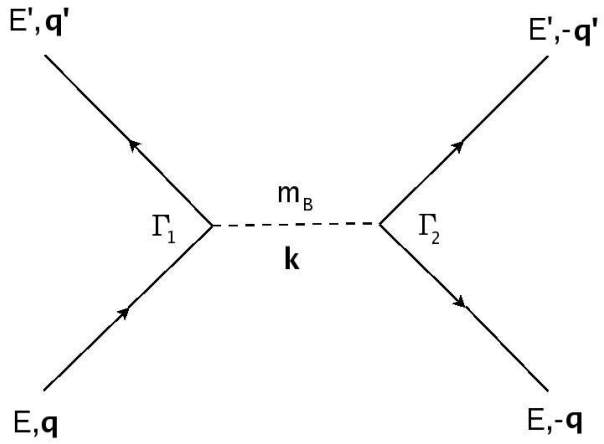

Figure 2.1: Feynman diagram for one-boson exchange in NN scattering in the center-of-mass frame [Mac89] which describes the amplitude given in Equation 2.7. Solid lines denote nucleons and the dashed line is a boson of mass, m_B. The symbols, Γ_i, represent the BNN vertices. The change in momentum is given by $\mathbf{k} = \mathbf{q}' - \mathbf{q}$.

used form factors are given as follows [Sto94]:

$$\begin{aligned} F(\mathbf{k}^2) &= 1, && (none) \\ F(\mathbf{k}^2) &= \frac{\Lambda^2 - m^2}{\Lambda^2 + \mathbf{k}^2}, && (monopole) \\ F(\mathbf{k}^2) &= \left[\frac{\Lambda^2 - m^2}{\Lambda^2 + \mathbf{k}^2}\right]^2, && (dipole) \\ \text{and } F(\mathbf{k}^2) &= e^{\mathbf{k}^2/\Lambda^2}. && (exponential) \end{aligned} \tag{2.9}$$

This project uses four high-precision NN potentials based more or less on the principles of meson-exchange to compare the cross-section data with theoretical predictions. They are the Nijmegen I and II (Nijm I and II) [Sto94], the Argonne V_{18} [Wir95], and the CD-Bonn [Mac01a] potentials. These potentials were developed in the 1990's and each fit the pruned 1992 Nijmegen database to a χ^2/datum ≈ 1 [Mac01b]. The 1992 Nijmegen database contains all pp and np scattering data below $T_{lab} = 350\ MeV$ published in a regular physics journal between 1955 and 1992 [Sto93] with certain exceptions which were rejected upon χ^2 analysis. Additional data have been accumulated since and the χ^2/datum produced by these potentials has suffered somewhat [Mac01b].

A few concepts must be addressed before a proper comparison of these potentials may proceed. The first is charge independence, defined as invariance to rotations in isospin space. For the purpose of this discussion, this boils down to identical treatment of nn, np, and pp

interactions once Coulomb forces are removed. Any violation of this principle is known as charge-independence breaking (CIB) or charge-dependence. A special case of charge independence is charge symmetry, which states that the nn and pp nuclear interactions should be identical. Any violation of this principle is called charge-symmetry breaking (CSB). Evidence for CIB is found in comparisons of Coulomb corrected pp and np scattering data. The effects of CSB are seen in Nolen-Schiffer anomaly which concerns differences in the binding energies of neighboring mirror nuclei [Nol69]. All of the meson-exchange NN potential models incorporate CIB and CSB to some extent. Both CIB and CSB are included in these potentials through charged-neutral mass splitting in the pion and nucleon, respectively, although not necessarily in all relevant terms. The concept of locality must also be addressed. Local potentials do not depend explicitly on the initial or final momenta, but only upon the momentum transfer, $\mathbf{k} = \mathbf{q}' - \mathbf{q}$. This is a reasonable approximation for low energies, however off-shell effects cause the approximation to break down at energies above ≈350 MeV.

The Nijmegen potentials [Sto94] are based on OBE potential functions with exponential form factors. The bosons included are three pseudoscalar mesons (π, η, η'), three vector mesons (ρ, ω, ϕ), and three scalar mesons (a_0, f_0, ε). The Particle Data Group [Nak10] contains information about all of these mesons except the ε, which would have the properties of the f_0 with a mass of 760 Mev/c^2. Also included are the $J = 0$ parts of the Pomeron, f_2, f_2', and a_2 tensor-meson trajectories. Here, CSB is included by explicitly including the mass difference between the proton and neutron. The mass differences between the π^0 and the $\pi^\pm$, as well as the ρ^0 and the $\rho^\pm$ are included as well to include CIB in both the long range and core regions of the interaction. The Nijm I potential contains non-local momentum dependent terms in its central component, though its tensor component is local. The Nijm II model differs from the Nijm I in that it is entirely local.

The AV18 potential [Wir95] is comprised of three parts: an electromagnetic (EM) part, a one-pion exchange (OPE) part, and a combined intermediate- and short-range phenomenological part. Here, CIB and CSB are incorporated into the EM part by including mass differences for the proton and neutron as well as taking into account the different EM properties of the nucleons. The OPE part also includes neutron-proton and charged-neutral pion mass-splitting. The OPE potential contains momentum space Gaussian cutoffs which make them vanish at $r = 0$ and simulate the effects of ρ-meson exchanges. The intermediate- and short-range phenomenological part is built from local Wood-Saxon type functions. This part of the potential only incorporates charge-dependence in its $^1S_0$ central component.

The CD-Bonn potential [Mac01a] is based on OBE potential functions using dipole form factors to regulate the short-range interaction. This model includes all mesons with masses

less than the nucleon (π, η, ρ, ω) as well as two fictional scalar-isoscalar σ bosons. The η is effectively dropped by incorporating a vanishing coupling to the nucleon. The σ bosons, introduced to simulate multi-meson exchanges, have masses and coupling constants which are adjusted in each partial wave to fit the 1992 Nijmegen database [Sto93]. This potential is entirely non-local and contains full CIB and CSB in all partial waves with $J \leq 4$.

2.2.2 Three Nucleon Force

Three-nucleon force effects arise from the quark substructure of the nucleon. The residual strong interaction between color neutral nucleons is simulated through the meson-exchange potentials discussed in the previous section. However, the 2N interaction may distort the quark substructure, altering the interaction between these nucleons and others that may be in their vicinity. The resulting 3NF effects in the framework of meson-exchange theory are typically modeled via two-pion exchange (TPE) interactions as shown in Figure 2.2. The first

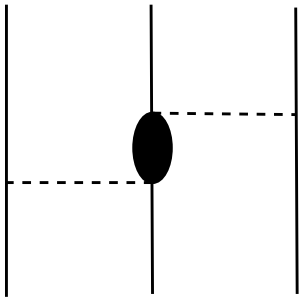

Figure 2.2: Feynman diagram from two-pion exchange. The solid lines represent nucleons, the dashed lines pions. The shaded oval represents anything except a forward propagating nucleon state which may be represented by iterations of the 2N interaction.

3NF based on TPE was developed by Fujita and Miyazawa [Fuj57] in an attempt to explain the underestimation of the triton binding energy by 2N interactions, though at this time the quark substructure of nucleons had yet to be proposed. The process they proposed was the following: one nucleon emits a pion which is scattered by a second nucleon before being absorbed by the third nucleon. Some aspects of this process may be explained by iterations of 2N interactions, by considering two uncorrelated OPE processes. However, 2N interactions do not take into account the intermediate excitation of the second nucleon which is the process of concern.

The modern 3NF's used in theoretical cross-section calculations for this project are the 1999 update to the Tuscon-Melbourne (TM99) potential [Coo01] and the Urbana IX (UIX) potential [Pud97]. These potentials are both non-local, charge-independent, and based upon TPE with an intermediate Δ-isobar. The TM99 potential is a modification of the TM81 [Coo81]

model which excludes a short-range contact term inconsistent with chiral symmetry and contains updated strength constants corresponding recent measurements of pion observables. The UIX potential was developed for exclusive use with the AV18 2N potential. It contains a 2PE term and a short-range phenomenological term each with a single coefficient which were fit to the density of nuclear matter and the binding energy of ^{3}H.

2.2.3 Chiral Effective Field Theory

The interaction between nucleons should be based on the strong theory of quantum chromodynamics (QCD) involving the interactions between quarks and gluons. However, at low energies (E $<$ 1 GeV) the characteristic degrees of freedon are not quarks and gluons, but nucleons and pions. To generate an effective theory for these degrees of freedom based on QCD, one may invoke a theorem proposed by Weinberg [Wei79] which he implemented to create the first chiral effective Lagrangians [Wei91].

> "If one writes down the most general possible Lagrangian, including all terms consistant with the assumed symmetry principles, and then calculates matrix elements with this Lagrangian to any given order in perturbation theory, the result will simply be the most general possible S-matrix consistent with analyticity, perturbative unitarity, cluster decomposition, and the assumed symmetry principles."

The big idea behind this theorem is that no assumptions can be made about the Lagrangian. All relevant terms must be included ensuring that the effective theory is the low-energy limit of QCD. To develop a potential model using an effective Lagrangian, a process for organizing the terms by their importance into a perturbative expansion must be developed. In chiral perturbation theory (χPT), the expansion parameter used in the perturbative scheme is given by the ratio $\mathcal{Q}/\Lambda$, where $\mathcal{Q}$ is the the soft scale given by the pion mass and/or external nucleon momenta and Λ is the hard scale of the order of the nucleon mass [Epe09]. The processes considered in the expansion are pion exchanges and contact interactions between nucleons. Heavy meson exchanges appear only indirectly in the contact terms. Feynman diagrams for these interactions are shown in Figure 2.3. The order of the expansion parameter ν for a particular Feynman diagram is determined by the following equation:

$$\nu = -2 + 2E_n + 2(L - C) + \sum_i V_i \Delta_i, \tag{2.10}$$

where E_n, L, C, and V_i are the numbers of nucleons, loops, separately connected pieces, and vertices of type i, respectively. The dimension of a vertex of type i is given by Δ_i, defined as:

$$\Delta_i = d_i + \frac{n_i}{2} - 2, \tag{2.11}$$

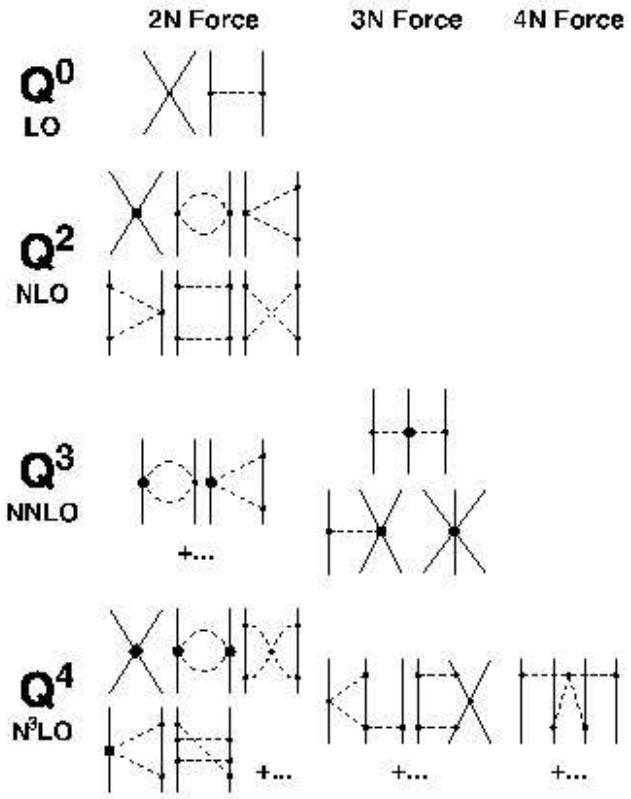

Figure 2.3: Feynman diagrams showing the hierarchy of nuclear forces in χPT. Solid lines represent nucleons and dashed lines pions. Solid dots, filled circles, squares, and diamonds denote vertices with Δ_i=0, 1, 2, and 3 [Mac05].

where d_i is the number of derivatives or pion mass insertions and n_i is the number of nucleon lines at the vertex [Epe05]. Please note that, for example, in a two-nucleon contact interaction (the first diagram in Figure 2.3) there are two nucleons ($E_n = 2$), while there are four nucleon lines at the vertex ($n_i = 4$). The nomenclature pertaining to this ordering scheme is that $\nu = 0$ is referred to as leading order (LO), $\nu = 2$ next-to-leading order (NLO), $\nu = 3$ next-to-next-to-leading order (NNLO), $\nu = 4$ next-to-next-to-next-to-leading order (N^{3}LO), and so on. Diagrams with $\nu = 1$ are not included as a result of parity conservation which forbids $(\overline{N}N)(\overline{N}N)$ vertices with one spatial derivative and πNN vertices with two derivatives. Also Equations 2.10 and 2.11 would imply that one irreducible 3N term involving a 2π-exchange with $\Delta_i = 0$ should appear at NLO, however this term is shifted to higher orders because of a $1/m$ factor appearing in its potential. Thus the 3NF does not arise until NNLO in χPT [Epe09].

Two nucleon potentials have been calculated up to N^{3}LO in χPT [Epe05]. These potentials are built from separate contributions arising from pion exchange and contact interactions. At N^{3}LO, terms arising from 1π, 2π, and 3π exchanges must be considered. A general outline of the structure of 2N chiral potentials up to N^{3}LO is given as follows:

$$
\begin{aligned}
V_{2N} &= V_{cont} + V_{\pi}, \\
\text{where} \quad V_{cont} &= V_{cont}^{(0)} + V_{cont}^{(2)} + V_{cont}^{(4)} + \cdots, \\
\text{and} \quad V_{\pi} &= V_{1\pi} + V_{2\pi} + V_{3\pi} + \cdots, \\
V_{1\pi} &= V_{1\pi}^{(0)} + V_{1\pi}^{(2)} + V_{1\pi}^{(3)} + V_{1\pi}^{(4)} + \cdots, \\
V_{2\pi} &= V_{2\pi}^{(2)} + V_{2\pi}^{(3)} + V_{2\pi}^{(4)} + \cdots, \\
V_{3\pi} &= V_{3\pi}^{(4)} + \cdots .
\end{aligned}
\tag{2.12}
$$

The superscript in parenthesis refers to the chiral order, ν, of the term. The explicit forms of these terms and their partial wave expansions have been derived by Epelbaum *et al.* [Epe05]. A number of "low energy constants" (LEC) arise in these potentials. All LEC related to pion exchange take experimentally determined values. At LO, these are the nucleon and pion masses (m_n, m_p, $M_{\pi^\pm}$, M_{π^0}), the pion decay constant F_π, and the axial-vector coupling constant g_a. At NNLO and N^{3}LO, four additional LEC are needed at each order which have been determined from πN scattering. The short-range contact terms also contain LEC that must be fixed from a fit to the Nijmegen database [Sto93], two at LO, seven at NLO, and fifteen at N^{3}LO. There are two high-momentum cutoffs, $\tilde{\Lambda}$ and Λ, used to prevent the potentials from delving too deeply into the nucleons to reveal the underlying quark structure.

The first of these, $\tilde{\Lambda}$, is used in the regularized spectral functions, $A^{\tilde{\Lambda}}(q)$ and $L^{\tilde{\Lambda}}(q)$, which are applied to prevent terms involving 2π-exchange loops from having components with a range, $r < \tilde{\Lambda}^{-1}$ [Epe05]. These spectral functions are given as follows:

$$\begin{aligned} A^{\tilde{\Lambda}}(q) &= \theta(\tilde{\Lambda} - 2M_\pi)\frac{1}{2q}\arctan\left[\frac{q(\tilde{\Lambda} - 2M_\pi)}{q^2 + 2\tilde{\Lambda}M_\pi}\right], \\ \text{and } L^{\tilde{\Lambda}}(q) &= \theta(\tilde{\Lambda} - 2M_\pi)\frac{\omega}{2q}\ln\left[\frac{(\tilde{\Lambda}\omega + qs)^2}{4M_\pi^2(\tilde{\Lambda}^2 + q^2)}\right], \\ \text{where } \omega &= \sqrt{q^2 + 4M_\pi^2}, \text{ and } s = \sqrt{\tilde{\Lambda}^2 + 4M_\pi^2}. \end{aligned} \tag{2.13}$$

The other high-momentum cutoff Λ is a parameter of an exponential regulator function $f^\Lambda(p)$ which is applied to the entire chiral potential to remove divergences in the Lippmann-Schwinger or Faddeev equations depending on whether a 2N or 3N system is being considered. The potential is modified as follows:

$$V(\mathbf{p}, \mathbf{p}) \rightarrow f^\Lambda(p) V(\mathbf{p}, \mathbf{p}') f^\Lambda(p'), \tag{2.14}$$

$$\text{where } f^\Lambda(p) = \exp\left[-\left(\frac{p}{\Lambda}\right)^{2n}\right]. \tag{2.15}$$

Here the parameter n is chosen such that the regulator function generates powers beyond the order ν of the calculation.

Five NNLO and five N^{3}LO two-nucleon chiral potentials were used in Faddeev calculations for this project. The five potentials at each order differed in their high-momentum cutoff values, Λ and $\tilde{\Lambda}$. Once the combination of high-momentum cutoffs was determined, the potentials were fit to the Nijmegen database [Sto93] using the LEC of the contact terms as variables [Epe05]. The high-momentum cutoff pairs used to create the chiral potentials used in this project are given in MeV as follows and all describe 2N scattering observables equally well:

$$\left\{\Lambda, \tilde{\Lambda}\right\} = \{450, 500\}, \ \{600, 500\}, \ \{450, 600\}, \ \{450, 700\}, \ \{600, 700\}. \tag{2.16}$$

The first non-vanishing 3NF enters χPT at NNLO with three relevant terms: a 2π-exchange term, a contact plus 1π-exchange term, and a 3N contact term. This introduces two new unknown LEC into the potential, one for each term involving contact interactions [Epe02]. This project used five NNLO chiral potentials which contained 3NF terms. These used the same high-momentum cutoffs as listed above, only the 3NF contributions were modified by a slightly different regulator function than was used for the 2N contribution. This function is

given by:

$$f^{\Lambda}(p,q) = \exp\left[-\left(\frac{4p^2+3q^2}{4\Lambda^2}\right)^n\right], \tag{2.17}$$

where p and q are the Jacobi momenta for the two-body subsystem and and spectator nucleon defined later in Equation 2.50. The two LEC associated with the 3NF were then fit to the triton binding energy and the nd doublet scattering length.

At N^{3}LO, 3N interactions involve five different topologies shown in Figure 2.4. The three long-range topologies involving (a) 2π exchange, (b) 2π-1π exchange, and (c) ring diagrams do not introduce any new parameters into the potential. The potentials for these processes have been derived [Ber08], but have yet to be encoded in a form applicable to numerical Faddeev calculations. The remaining topologies (d) and (e) involve two-nucleon contact interactions and introduce new LEC which will have to be fit to 3N observables. Their contribution to chiral potentials have yet to be derived, but should have little effect on the low-energy 3N system as a result of their limited range.

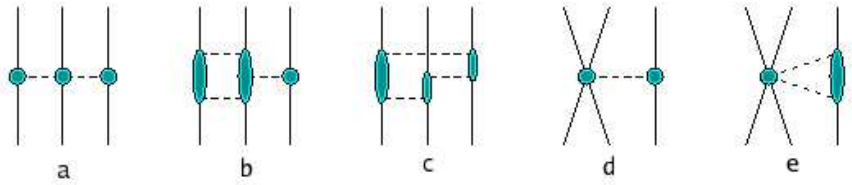

Figure 2.4: Feynman diagrams for the various topologies which appear in N^{3}LO of χPT. Solid and dashed lines are nucleons and pions, respectively. The shaded blobs represent the corresponding amplitudes. The long range terms which have been calculated are (a) 2π exchange, (b) 2π-1π exchange, and (c) ring diagrams. Short-range topologies (d) and (e) involve 4N contact operators and have not been calculated [Ber08].

2.3 Scattering Theory

Once a potential model is selected, one must apply quantum mechanical scattering theory to obtain the elements of the transition matrix. All physical observables may then be obtained from the transition matrix. We will begin the section on scattering theory with a review of two-body scattering and the Lippmann-Schwinger equation (LSE). Since this experiment involves three-body scattering, we will then extend the LSE to include an additional particle, deriving the Faddeev equations. Finally, the inclusion of the three-nucleon force into the Faddeev scheme requires some special treatment which will be discussed.

2.3.1 Two Body Scattering

We will begin our derivation of two-body scattering theory with the Schrödinger equations for a free particle with wavevector, $\mathbf{k}$, and energy $\mathrm{E}_k = \hbar^2 k^2/2\mu$ and for the scattering of this particle from a finite-ranged potential $V(r)$, where $V(r) = 0$ for $r > R$. These are given by:

$$(E_k - H_0)\,|\phi_k\rangle = 0, \tag{2.18}$$

and

$$(E_k - H)\,|\psi_k\rangle = 0, \tag{2.19}$$

where H_0 is the kinetic energy operator and $H = H_0 + V$. If we now define the free particle Green's function propagator,

$$G_0(E_k) \equiv \frac{1}{E_k - H_0 + i\epsilon}, \tag{2.20}$$

Equation 2.19 may be expressed as follows:

$$|\psi_k\rangle = |\phi_k\rangle + G_0(E_k)V\,|\psi_k\rangle\,. \tag{2.21}$$

We will now define the transition operator or T-matrix,

$$T_{k'k} \equiv \langle\phi_{k'}|\,T(E_k)\,|\phi_k\rangle = \langle\psi_{k'}|\,V\,|\psi_k\rangle\,. \tag{2.22}$$

Multiplying Equation 2.21 from the left by the potential, V, and using Equation 2.22 to transform all free particle wavefunctions, $|\phi_k\rangle$, into scattered wavefunctions, $|\psi_k\rangle$, we obtain the Lippmann-Schwinger equation [Lip50] for the T-matrix,

$$T(E_k) = V + VG_0(E_k)T(E_k). \tag{2.23}$$

In general, the solutions to the Lippmann-Schwinger equation may be described by an asymptotic expansion of the wavefunction into an incident plane wave and an outgoing spherical wave,

$$\psi(\mathbf{r}) = \frac{1}{(2\pi)^{\frac{3}{2}}}\left[e^{i\mathbf{k}\cdot\mathbf{r}} + f(\mathbf{k}',\mathbf{k})\frac{e^{ikr}}{r}\right]. \tag{2.24}$$

The coefficient in front of the scattered wave, f(**k'**,**k**), which has units of length, is known as the scattering amplitude. All information about two-body scattering is contained in this coefficient. It is directly proportional to the T-matrix and can be calculated as follows:

$$\begin{aligned} f(\mathbf{k}',\mathbf{k}) &= -2\pi^2\left(\frac{2\mu}{\hbar^2}\right)\int d^3r'\frac{e^{-i\mathbf{k}'\cdot\mathbf{r}'}}{(2\pi)^{\frac{3}{2}}}V(\mathbf{r}')\psi(\mathbf{r}'), \\ &= -2\pi^2\left(\frac{2\mu}{\hbar^2}\right)\langle\phi_{k'}|\,V\,|\psi_k\rangle\,, \end{aligned}$$

$$= \quad -2\pi^2 \left(\frac{2\mu}{\hbar^2}\right) \langle \phi_{k'} | \, T(E_k) \, | \phi_k \rangle \, . \tag{2.25}$$

To obtain the differential cross section, $\frac{d\sigma}{d\Omega}$, we must take the ratio of particle flux scattered into some solid angle, $d\Omega$, to the incident particle flux crossing some small area, $d\sigma$. The incident particle flux is proportional to the square of the first term in Equation 2.24 and the scattered flux to the second term [Sak94]. Thus,

$$\frac{d\sigma}{d\Omega} d\Omega = \frac{r^2 |\mathbf{j}_{scatt}| d\Omega}{|\mathbf{j}_{incid}|}. \tag{2.26}$$

Therefore, the differential cross section is simply the square of the scattering amplitude,

$$\begin{aligned} \frac{d\sigma}{d\Omega} &= |f(\mathbf{k}', \mathbf{k})|^2 \\ &= 4\pi^4 \left(\frac{2\mu}{\hbar^2}\right)^2 |\langle \mathbf{k}' | \, T(E_k) \, | \mathbf{k} \rangle|^2. \end{aligned} \tag{2.27}$$

To calculate the cross section for some two body scattering process, one must find the associated T-Matrix elements from the Lippmann-Schwinger equation.

2.3.2 Three Body Scattering

We will begin with three particles, two of them in an initial bound state. The particles may interact with each other through pairwise forces. After this interaction, the particles are free. The breakup operator which describes this process is given by the following series [Glö96]:

$$U_0^{(1)} \equiv V_3\phi_1 + V_2\phi_1 + V_1G_0V_3\phi_1 + V_3G_0V_3\phi_1 + V_3G_0V_2\phi_1 + \cdots . \tag{2.28}$$

Here, the initial state is denoted as ϕ_1, G_0 is the free three-body propagator for pair inter-

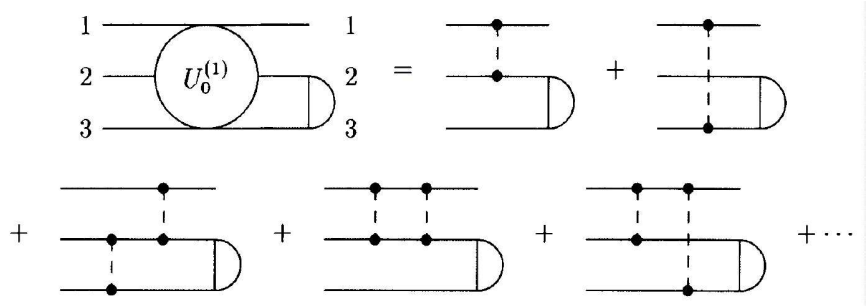

Figure 2.5: Diagram depicting the infinite multiple scattering breakup series of Equation 2.28 [Glö96]. Please note that time propagates from right to left with the initial bound state indicated by the semi-circle.

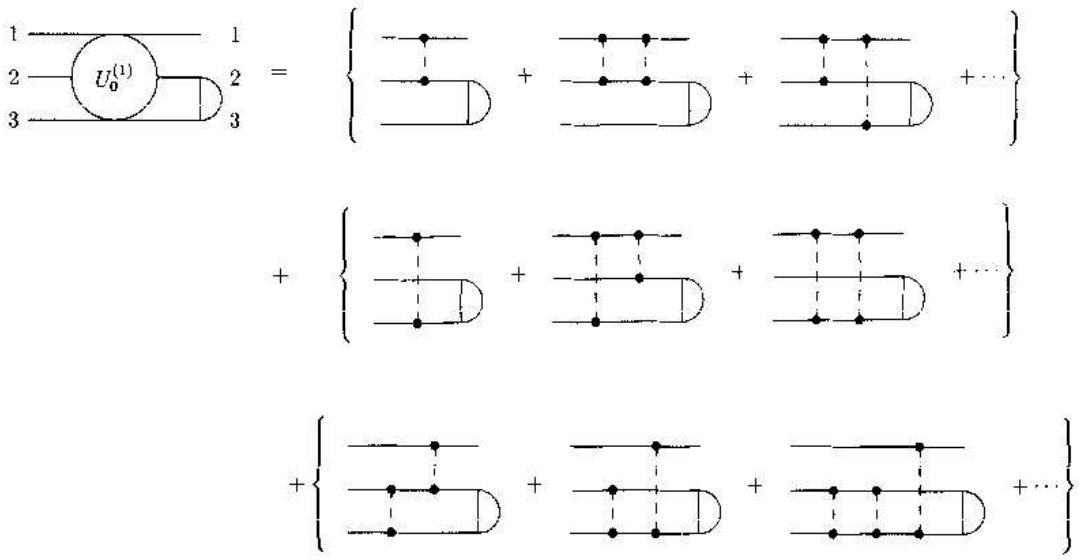

Figure 2.6: Diagram depicting the rearrangement of the infinite multiple scattering breakup series to apply the Faddeev scheme described in Equation 2.29 [Glö96].

actions, and the subscript on the pair interaction refers to the spectator particle, $V_1 \equiv V_{23}$ The superscript on the breakup operator, $U_0^{(1)}$, indicates that the 1^{st} particle is the projectile. The initial interaction must be between projectile and target, thus all terms in the expansion of the operator, $U_0^{(1)}$ must begin with either V_2 or V_3.

The key to solving this equation is in the organization of the terms. The Faddeev method [Fad61] for approaching this problem is to group all terms which end with one specific pair interaction on the left. Thus, the breakup operator may be separated as follows:

$$U_0^{(1)} = \left(U_0^{(1,3)} + U_0^{(1,2)} + U_0^{(1,1)}\right)\phi_1, \tag{2.29}$$

where the second superscript in these partial breakup operators denotes the spectator particle to this final two-body interaction. A diagram depicting this is included in Figure 2.6. The separation of this operator provides a system of three coupled equations, given by:

$$\begin{aligned} U_0^{(1,3)} &= V_3\phi_1 + V_3G_0\left(U_0^{(1,3)} + U_0^{(1,2)} + U_0^{(1,1)}\right)\phi_1, \\ U_0^{(1,2)} &= V_2\phi_1 + V_2G_0\left(U_0^{(1,3)} + U_0^{(1,2)} + U_0^{(1,1)}\right)\phi_1, \\ \text{and } U_0^{(1,1)} &= V_1G_0\left(U_0^{(1,3)} + U_0^{(1,2)} + U_0^{(1,1)}\right)\phi_1. \end{aligned} \tag{2.30}$$

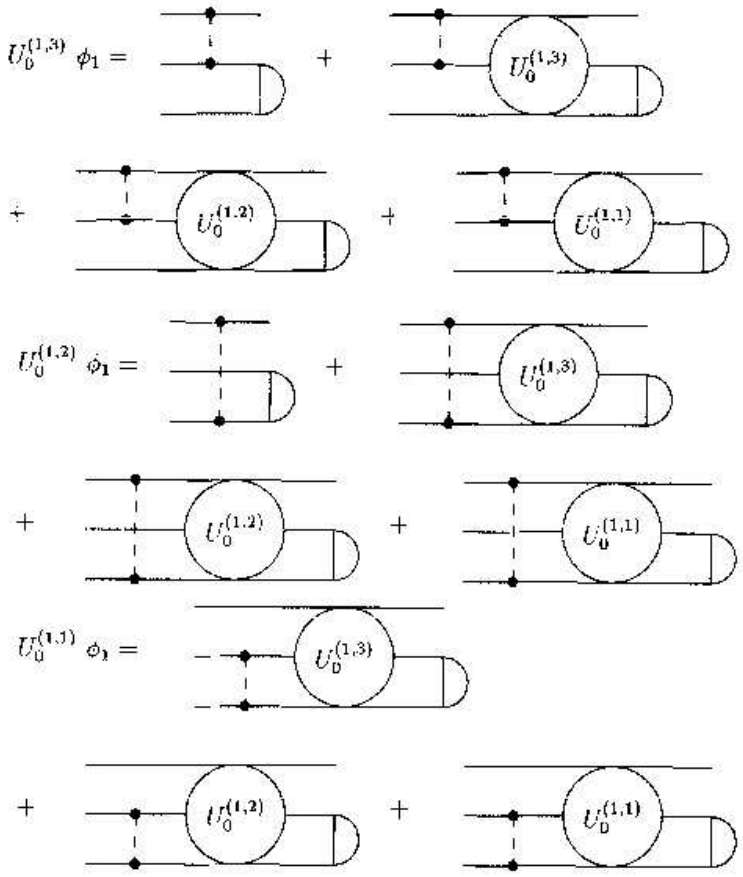

Figure 2.7: Diagram showing the separation of Equation 2.29 into Equations 2.30 [Glö96].

Examining the first of Equations 2.30, terms containing $U_0^{(1,3)}$ may be combined on the left hand side as follows:

$$\left(1 - V_3 G_0\right) U_0^{(1,3)} \phi_1 = V_3 \phi_1 + V_3 G_0 \left(U_0^{(1,2)} + U_0^{(1,1)}\right) \phi_1. \tag{2.31}$$

The operator acting on the partial amplitude, $U_0^{(1,3)}$, in Equation 2.31 may then be inverted to obtain:

$$U_0^{(1,3)} \phi_1 = t_3 \phi_1 + t_3 G_0 \left(U_0^{(1,2)} + U_0^{(1,1)}\right) \phi_1, \tag{2.32}$$

where the quantity, t_3, is defined as follows:

$$t_3 \equiv \left(1 - V_3 G_0\right)^{-1} V_3 \tag{2.33}$$

$$= V_3 + V_3 G_0 t_3. \tag{2.34}$$

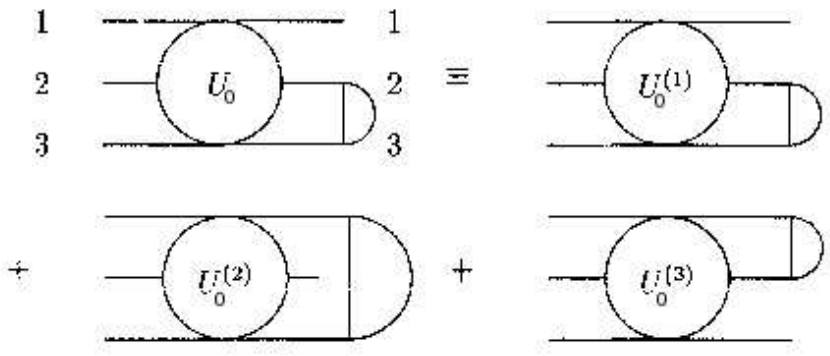

Figure 2.8: Diagram of the antisymmetrization of the breakup amplitude [Glö96].

This is simply the two-body T-matrix for particles 1 and 2 in a three-body space and obeys the LSE, as shown in Equation 2.34. Applying the same algebraic manipulations to the expressions for $U_0^{(1,2)}$ and $U_0^{(1,1)}$ in Equations 2.30, we obtain a set of three coupled Faddeev equations:

$$\begin{aligned} U_0^{(1,3)}\phi_1 &= t_3\phi_1 + t_3 G_0 \left(U_0^{(1,2)} + U_0^{(1,1)}\right)\phi_1, \\ U_0^{(1,2)}\phi_1 &= t_2\phi_1 + t_2 G_0 \left(U_0^{(1,3)} + U_0^{(1,1)}\right)\phi_1, \\ \text{and } U_0^{(1,1)}\phi_1 &= t_1 G_0 \left(U_0^{(1,3)} + U_0^{(1,2)}\right)\phi_1. \end{aligned} \tag{2.35}$$

The final requirement in applying the Faddeev equations to *nd* breakup is that the wavefunction must be antisymmetric, since the equations treat the three nucleons as identical fermions. We will do this for the initial wavefunction by replacing ϕ_1 as follows:

$$\phi_1 \Rightarrow \phi_a \equiv \phi_1 + \phi_2 + \phi_3. \tag{2.36}$$

Repeating the procedure above for ϕ_2 and ϕ_3, one may obtain the properly antisymmetrized breakup amplitude, given by [Glö96]:

$$U_0\phi_1 \equiv U_0^{(1)}\phi_1 + U_0^{(2)}\phi_2 + U_0^{(3)}\phi_3 = \sum_i \sum_k U_0^{(k,i)}\phi_k \equiv \sum_i U_{0,i}\phi_1. \tag{2.37}$$

Combining Equation 2.37 with iterations of Equation 2.35 for ϕ_2 and ϕ_3, we obtain the following set of equations:

$$U_{0,1}\phi_1 = t_1\left(\phi_2 + \phi_3\right) + t_1 G_0 \left(U_{0,2} + U_{0,3}\right),$$

$$
\begin{aligned}
U_{0,2}\phi_1 &= t_2\left(\phi_3+\phi_1\right)+t_2G_0\left(U_{0,3}+U_{0,1}\right), \\
\text{and}\ \ U_{0,3}\phi_1 &= t_3\left(\phi_1+\phi_2\right)+t_3G_0\left(U_{0,1}+U_{0,2}\right).
\end{aligned} \tag{2.38}
$$

Upon inspection of these equations, one may notice that the second and third equations are simply cyclic and anticyclic permutations of the first, respectively. Introducing the permutation operator,

$$
P \equiv P_{12}P_{23}+P_{13}P_{23}, \tag{2.39}
$$

and the 3N T-matrix,

$$
T \equiv U_{0,1}, \tag{2.40}
$$

the Faddeev equations may be written in the following elegant form (note the index 1 has been dropped from t and ϕ):

$$
T\phi = tP\phi + tPG_0T\phi. \tag{2.41}
$$

Once T is determined from Equation 2.41, the full breakup operator is given by the following:

$$
U_0 = (1+P)\,T. \tag{2.42}
$$

The operator for elastic scattering, U, may also be obtained from the T-matrix by removing all terms in the series given in Equation 2.28 which end with the interaction, V_1, between the nucleons in the bound state. This operator is given as follows:

$$
U\phi = PG_0^{-1}\phi + PT\phi. \tag{2.43}
$$

2.3.3 Inclusion of the Three Nucleon Force

To include a three-nucleon force into Faddeev calculations, a potential V_4 which acts on all three nucleons must be included in the Hamiltonian to obtain

$$
H = \sum_{i=1}^{3}\left(\frac{p_i^2}{2m_i}+V_i\right)+V_4. \tag{2.44}
$$

Introducing the following definitions:

$$
t_4 = V_4 + V_4G_0t_4,\ T = tG_0U_0,\ T_4 = t_4G_0U_0, \tag{2.45}
$$

and following a procedure analogous to the derivation of the Faddeev equations for 2N interactions above, the following set of coupled differential equations for the 3N T-matrices may be derived:

$$
T\phi = tP\phi + tG_0T_4\phi + tPG_0T\phi \tag{2.46}
$$

$$\text{and} \quad T_4\phi \;=\; (1+P)\,t_4\phi + (1+P)\,t_4 G_0 T\phi. \tag{2.47}$$

The breakup operator is then given simply as:

$$U_0 = (1+P)\,T + T_4. \tag{2.48}$$

The full derivation of these equations is beyond the scope of this thesis. A more detailed (although still incomplete) derivation of the 3NF Faddeev equations is included in the review article by Glöckle, *et al.* [Glö96] which includes references that explain the entire detailed procedure.

2.3.4 Calculating Cross Sections for Three Nucleon Processes

All neutron-deuteron observables must be calculated from the transition matrix amplitudes, $\langle\phi'|\,U\,|\phi\rangle$ for elastic scattering and $\langle\phi_0|\,U_0\,|\phi\rangle$ for breakup processes. These share the same initial state defined by: the relative momentum $\mathbf{q}_0$ of the neutron with respect to the deuteron, the deuteron wavefunction φ_d, and the spin quantum numbers, m_d and m_n. Thus the initial state is given by:

$$|\phi\rangle = |\varphi_d m_d\rangle\,|\mathbf{q}_0 m_n\rangle\,. \tag{2.49}$$

The final state for elastic scattering, $|\phi'\rangle$, shares the same $\mathbf{q}_0$ as $|\phi\rangle$ with all other parameters being primed. The final state for the breakup process, $|\phi_0\rangle$, may be defined by the relative momenta of the three particles and their spin magnetic quantum numbers. The relative Jacobi momenta are defined as:

$$\begin{aligned} \mathbf{p}_i \;&=\; \frac{1}{2}\left(\mathbf{k}_j - \mathbf{k}_k\right) \\ \text{and} \quad \mathbf{q}_i \;&=\; \frac{2}{3}\left(\mathbf{k}_i - \frac{1}{2}\left(\mathbf{k}_j + \mathbf{k}_k\right)\right). \end{aligned} \tag{2.50}$$

The final breakup state may then be described by any of the three pairs of these Jacobi momenta and is given by:

$$|\phi_0\rangle = |\mathbf{p}\mathbf{q} m_1 m_2 m_3\rangle\,. \tag{2.51}$$

The elastic cross section may be expressed in terms of the spin-dependent scattering amplitude, M, as follows [Glö96]:

$$M_{m'_d m'_n m_d m_n}\left(\mathbf{q}', \mathbf{q}_0\right) \equiv -\frac{8}{3} m\pi^2 \left\langle\phi'\right|\,U\,|\phi\rangle\,, \tag{2.52}$$

so that

$$\frac{d\sigma}{d\Omega} = |M_{m'_d m'_n m_d m_n}\left(\mathbf{q}', \mathbf{q}_0\right)|^2. \tag{2.53}$$

Here, $\mathbf{q}' = q_0\hat{R}$ and $\hat{R}$ points in the direction of observation.

The breakup cross section may be calculated from the transition rate for the breakup process, the probability that an incident particle will cause a breakup event with relative momenta, $\mathbf{q}$ and $\mathbf{p}$,

$$dN = 2\pi|\langle\phi_0|\, U_0\, |\phi\rangle|^2 \int d\mathbf{q}\; d\mathbf{p} \left(\frac{3q_0^2}{4m} + \epsilon_d - \frac{p^2}{m} - \frac{3q^2}{4m}\right). \tag{2.54}$$

Transforming this into the laboratory system, we obtain:

$$\begin{aligned} dN &= 2\pi|\langle\phi_0|\, U_0\, |\phi\rangle|^2 \int d\mathbf{k}_1\; d\mathbf{k}_2\; d\mathbf{k}_3\; \delta\left(\mathbf{k}_{lab} - \mathbf{k}_1 - \mathbf{k}_2 - \mathbf{k}_3\right) \delta\left(E_{lab} + \epsilon_d - \sum \frac{k_i^2}{2m}\right), \\ &= 2\pi|\langle\phi_0|\, U_0\, |\phi\rangle|^2\; k_E\; d\Omega_1\; d\Omega_2\; dE_1. \end{aligned} \tag{2.55}$$

The phase space factor, k_E, is defined through the energy and momentum conserving delta functions. It suffers from a singularity where $dk_1/dk_2 = 0$ and may be double-valued for a given E_1. The solution is to replace E_1 with an arclength, S, along the kinematic locus which leads to:

$$k_S \equiv k_E \frac{dE_1}{dS} = \frac{(mk_1k_2)^2}{\sqrt{k_1^2\left(2k_2 - \hat{k}_2\cdot(\mathbf{k}_{lab} - \mathbf{k}_1)\right)^2 + k_2^2\left(2k_1 - \hat{k}_1\cdot(\mathbf{k}_{lab} - \mathbf{k}_2)\right)^2}}. \tag{2.56}$$

The momenta k_1 and k_2 are coupled by the following equation which defines the kinematic locus,

$$k_2^2 - \mathbf{k}_2\cdot(\mathbf{k}_{lab} - \mathbf{k}_1) + k_1^2 - \mathbf{k}_1\cdot\mathbf{k}_{lab} - m\epsilon_d = 0. \tag{2.57}$$

Dividing Equation 2.55 by the incident beam flux, we obtain the following expression for the five-fold differential cross section,

$$\frac{d^5\sigma}{d\Omega_1 d\Omega_2 dS} = (2\pi)^4\;\; |\langle\phi_0|\, U_0\, |\phi\rangle|^2\; \frac{2m}{3q_0}\; k_s. \tag{2.58}$$

To obtain the cross section in terms of E_1, rather than S, one must simply multiply Equation 2.58 by the derivative dS/dE_1 being mindful of the singularities and double values mentioned above. Both Equations 2.58 and 2.53 for the breakup and elastic nd differential cross sections refer to specific magnetic quantum numbers in the initial and final states (polarized beam and target). This experiment deals with unpolarized observables; thus we must average over the initial states and sum the final ones. For the breakup cross section, this gives:

$$\frac{d^5\sigma}{d\Omega_1 d\Omega_2 dS} = \frac{(2\pi)^4}{(2s_d+1)(2s_n+1)} \left(\frac{2m}{3q_0}\right) k_S \sum_{m_1 m_2 m_3} \left(\sum_{m_d m_n} |\langle\phi_0|\, U_0\, |\phi\rangle|^2\right). \tag{2.59}$$

3 Experimental Details

3.1 Introduction

This experiment consists of a kinematically complete differential cross-section measurement of neutron induced deuteron breakup at an incident neutron energy of 16.0 MeV. The breakup configurations studied were the space-star (SST) and the coplanar-star (CST) described earlier in Section 1.1. Each configuration is mirrored about a vertical plane containing the beam axis to double the count rate. One of the outgoing neutrons and the proton were detected in coincidence and their momenta were determined via time-of-flight (ToF) measurements. The target-beam luminosity was determined through a concurrent measurement of nd elastic scattering. Data were accumulated over the course of a year and required around 1400 hours of accelerator time. The entire experiment was performed in the Shielded Source Area (SSA) of the Triangle Universities Nuclear Laboratory (TUNL).

3.2 Deuterium Beam Production

A 13.65 MeV deuteron beam incident upon a deuterium gas cell was required to produce our 16.0 MeV neutron beam via the $^2H(d,n)^3He$ reaction. The specifics of neutron production will be covered in Section 3.3. The current section will discuss the production and acceleration of the deuteron beam.

3.2.1 The Direct Extraction Negative Ion Source

The deuteron beam was created by the Direct Extraction Negative Ion Source (DENIS), a duoplasmatron [Law65] located in the low-energy bay of the tandem laboratory at TUNL. The DENIS is capable of producing a 30 μA beam of negative hydrogen or deuterium ions at an energy of 50 keV. For the present experiment only about 4.5 μA of D^- ions were required. A diagram of DENIS is shown in Figure 3.1.

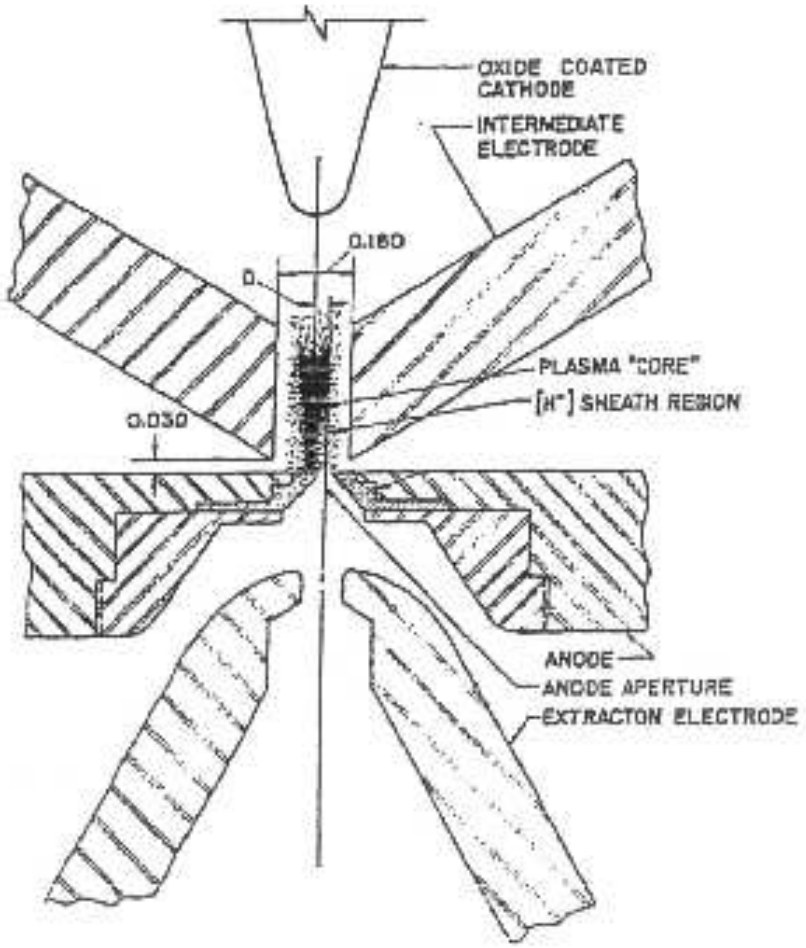

Figure 3.1: Critical region of the duoplasmatron [Law65] in the Direct Extraction Negative Ion Source (DENIS). The dimensions are given in inches in the diagram above.

To operate DENIS, a mixture of deuterium and hydrogen gas is leaked into a cylindrical steel chamber surrounded by a solenoidal magnet. A gas pressure of approximately 10^{-2} Torr is maintained in the chamber by balancing the leak rate with vacuum pumping. An electric potential of 150 V is applied between a cathode and anode on opposite ends of this chamber. The cathode consists of a nickel mesh filament coated with a mixture of barium and strontium oxides which lowers the work function of the nickel [Ble39]. A current through the filament causes resistive heating thereby inducing the emission of electrons. Under the right conditions an arc is struck in the region between the anode and cathode. The plasma is contained in this region by a solenoidal magnetic field. Depending upon the age of the filament, a filament current of 10-35 A is required to maintain the arc. The anode side of the steel chamber nar-

rows to an exit aperture located just before the anode as shown in Figure 3.1. High velocity electrons are confined near the central axis by the intense magnetic field at the narrow exit aperture of the chamber. These tend to knock electrons off of the H^0 and D^0 atoms forming positive ions. Low velocity electrons are only weakly influenced by the magnetic field and thus may migrate towards the edge of the aperture. These have a large capture cross section on the neutral atoms creating H^- and D^- ions. The net result of these two processes is to create a plasma with a dense positive core surrounded by a halo of negative ions. There is a small aperture in the anode offset from the central axis of the bottle, so as to be aligned with this negative halo. On the other side of the anode from the bottle an extraction electrode is held at a positive voltage between 0-10 kV with respect to the anode to separate the negative ions from any positive ions which may have passed though the aperture. This is followed by an electrostatic lens used to focus the ions as they enter the beamline. The entire DENIS system is held at a voltage of 50 kV with respect to ground providing the 50 keV beam energy of the departing negative ions. An inflection magnet downstream from DENIS is used to separate the H^- from the D^- ions and send the latter on to the accelerator. The ratio of hydrogen to deuterium gas injected into the bottle determines the D^- beam current. Additional beam optics between DENIS and the accelerator optimize the beam current and profile.

3.2.2 The Tandem Van de Graaff Accelerator

In this experiment, the Model FN Tandem Van de Graaff accelerator is used to take the 50 keV D^- beam produced by DENIS and convert it to a D^+ beam as it is accelerated up to 13.65 MeV. A diagram illustrating the basic operation of the accelerator is shown in Figure 3.2. The Tandem is a large steel cylindrical chamber with the beamline located just off its central axis. There is a high-voltage terminal at its center which has a maximum voltage of 10 MV. The terminal is insulated from the wall of the chamber by a $\sim$200 psi mixture of nitrogen, carbon dioxide, and sulfur hexafluoride gas. The terminal voltage is stepped down to ground by a series of resistors towards both ends of the accelerator, creating a smoothly increasing then decreasing electric potential as the beam traverses the machine. Within the terminal there is a thin carbon foil in the beamline which strips electrons from the D^- ions converting them to D^+ ions. Thus the negative beam is accelerated towards the terminal where it is stripped of its electrons and again accelerated to ground potential. For singly charged ion beams, energies corresponding to twice the terminal voltage are produced. For example, our 13.65 MeV deuteron beam was produced by a terminal voltage around 6.9 MV.

The accelerator terminal is charged by two Pelletron® chains situated on pairs of pulleys to each side of the terminal. These chains consist of a series of insulated metal pellets which are inductively charged at the ends of the machine. The charge is applied by a negative

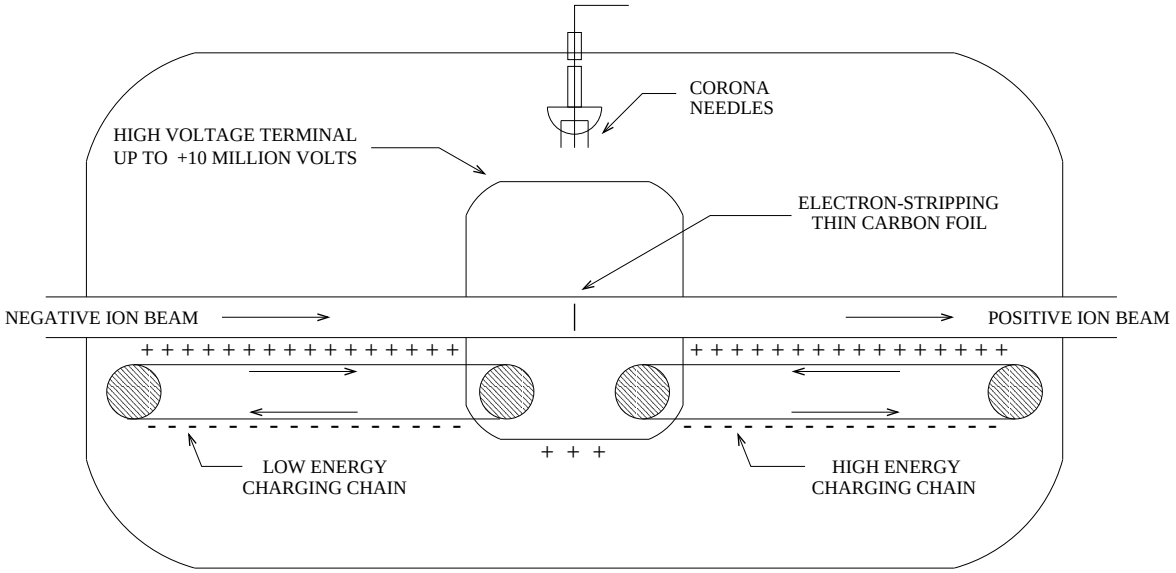

Figure 3.2: Illustration of the basic operation of the Model FN Tandem Van der Graaff Accelerator.

electrode which drives electrons from the pellet when it is in contact with a grounded pulley. This positively charged pellet then travels to the terminal where it is neutralized by electrons upon contact. The repetition of this process induces and maintains the terminal voltage.

When the tandem accelerator is operating, the precise terminal voltage is controlled by an analyzing the beam with a steering magnet, known at the "20-70," which is located downstream from the accelerator. This magnet may bend the beam down any of a series of beamlines identified by deflection angles ranging from 20° to 70°, hence its name. The strength of the magnetic field is set so particles of a particular mass, charge, and energy are sent down the center of the beamline in use, in this case the 20° line. After the magnet, a pair of slits is positioned on opposite sides of the beamline such that when the beam is centered it barely grazes each slit providing small current signals. If the terminal voltage is high or low, the beam will hit one of the slits more than the other. The current signals from the two slits are sent through a difference amplifier which generates a feedback signal used to adjust the terminal voltage accordingly. An array of fine metal needles attached to the end of a rod whose radial extention from the pressure tank is adjusted to produce a sustained coronal discharge from the terminal. The corona needles are connected to ground through a vacuum tube circuit with an effective resistance that is controlled by the slit feedback signal. This circuit continuously adjusts the current from the corona discharge to maintain a stable terminal voltage.

3.3 Neutron Production and Collimation

The 16.0 MeV neutron beam used in this experiment was produced via the $^2H(d,n)^3He$ reaction, which is often used to produce neutrons between 7 and 20 MeV because of its large 0° cross section compared with other neutron producing reactions [Dro78]. Both neutron energy and cross section decrease rapidly with deviations from 0°, making this an ideal reaction to produce a collimated neutron beam. The reaction has a +3.3 MeV Q-value, which provides a more than 5 MeV separation between the dominant background neutron source reactions; $^2H(d,n)dp$ and $^2H(d,n)ppn$.

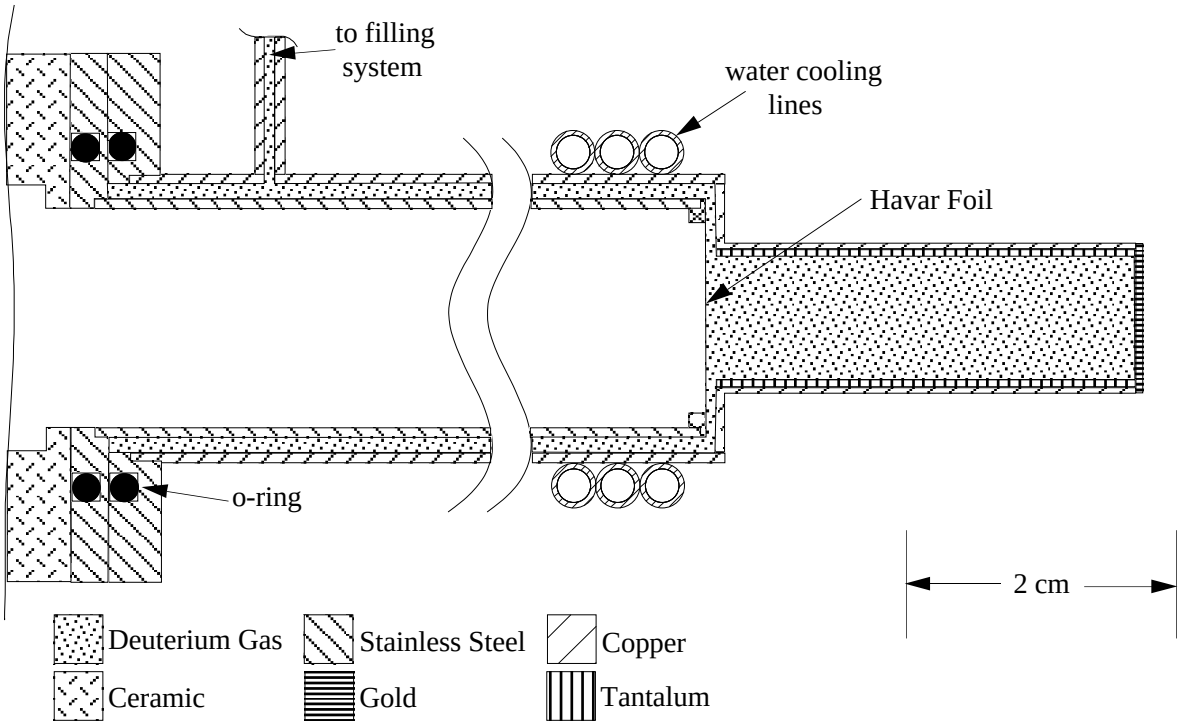

Figure 3.3: Deuterium gas cell used to produce neutron beam via the $^2H(d,n)^3He$ reaction. The length of the deuterium gas column was longer in the experiment than shown in the diagram because the insert holding the Havar foil was shorter than shown. This was done to increase the emitted neutron flux. Details are given in the text.

The neutron production reaction took place in a deuterium gas cell attached to the end of the 20° beamline, as shown in Figure 3.3. The gas cell was a copper tube with a 0.5 mm gold beam stop soldered to one end and a 6.35 μm thick Havar beam-entrance foil on the other end. The gas chamber within the cell was 71.4 mm long and filled to 7.8 atm with 99.99% pure research grade deuterium gas. Incident deuteron energy losses in the gas column lead to a ±340 keV spread in neutron beam energy. Distilled water was pumped through the copper

cooling coils surrounding the gas cell (see Figure 3.3) in a closed water circulation loop to remove the heat generated by stopping the beam in the cell. The temperature of the water in the closed loop was maintained by heat exchange with the main 50° C chilled water in the tandem lab. Air cooling was also applied to the gold beam stop and at the location of the Havar foil. The entire gas cell was electrically isolated from the remainder of the beam pipe and the current deposited on the beam stop was sent to a beam current integrator (BCI).

The target area was shielded from the neutron production cell and other upstream sources of neutron and gamma radiation by a wall composed of concrete, steel, lead, and paraffin. The hydrogen-rich concrete and paraffin were included for low-energy neutron shielding; while the high-Z steel, iron, and lead were used to deflect the γ-rays and higher energy neutrons [Gla74]. A 115 cm long double-truncated copper collimator with a circular cross section connects the neutron production cell to the target area. This collimator produced a roughly uniform neutron beam with a 40 cm diameter circular cross section at the location of the CD_2 target, 187 cm from the neutron production cell. See Appendix E for a description of measurements made to determine the energy and spatial distributions of the collimated neutron beam at produced at the target.

3.4 Experimental Setup

An illustration of the experimental setup is included in Figure 3.4 and a photograph showing the interior of the target chamber is shown in Figure 3.5. Surveyed detector angles and distances may be found in Table 3.1 and the techniques for their measurement are described in Appendix F. The 16.0 MeV neutron beam was incident on a 22.4 mg/cm^2 thick deuterated polyethylene (CD_2) target. The CD_2 target was approximately circular in shape with a diameter of 25.4 mm. The target was suspended in the center of a square aluminum target frame by thin nylon strings. The inner dimension of the target frame was 76.2 mm x 76.2 mm and the width of the frame was 6.35 mm. The frame was attached to the end of the target rod as shown in Figure 3.5. The target frame was mounted such that the incident beam axis was normal to the surface of the target. The target was housed in a scattering chamber which had the following characteristics: (1) a central cylindrical chamber, (2) a top dome, (3) two charged-particle arms, (4) a target rod, (5) a vacuum port, (6) a bottom plate with ports for the ΔE detectors, (7) entrance and exit windows for the beam. The central cylinder had a height of 17.1 cm and an inner diameter of 34.3 cm with 0.635 cm thick stainless steel walls. The top dome was composed of 0.318 cm thick aluminum. It was designed to allow emitted SST neutrons to exit the chamber through a thin barrier of uniform thickness while withstanding the $\sim$1 atm pressure differential. The charged particle arms were allowed the emitted protons and deuterons to travel sufficient distance to make ToF measurements

with reasonable energy resolution. The target rod could hold two targets which could be interchanged without breaking vacuum. Only one target was used for the main experiment; however, the second position proved useful for calibration runs. The vacuum in the chamber was produced and maintained by a turbo-molecular pump which provided chamber pressures on the order of 10^{-5} Torr over the course of the experiment. The two ΔE detectors needed to be positioned as close as possible to the target without being in the path of SST or CST emitted neutrons. The neutron beam entered the chamber through a 7.6 cm diameter, 100 μm thick beryllium window. The beam, as well as emitted CST neutrons, exited the chamber through a 25 μm thick rectangular tantalum window (6.4 cm $\times$ 2.0 cm).

Detector	θ (deg)	ϕ (deg)	Distance (cm)	Diameter (cm)	Thickness (cm)	Scint. Type
E1	51.3±0.5	180.0±0.1	69.0±0.2	10.0±0.05	0.50±0.02	BC-404
E2	52.3±0.5	0.0±0.1	69.0±0.2	10.0±0.05	0.50±0.02	BC-404
N1	51.4±0.5	119.5±0.5	73.0±0.2	12.68±0.05	5.08±0.05	BC-501A
N2	51.7±0.5	59.7±0.5	73.1±0.2	12.68±0.05	5.08±0.05	BC-501A
N3	17.7±0.5	180.0±0.5	101.3±0.2	12.68±0.05	5.08±0.05	BC-501A
N4	18.7±0.5	0.0±0.5	102.4±0.2	12.68±0.05	5.08±0.05	BC-501A

Table 3.1: Detector central angles, distances, and properties. The polar angle θ is given with respect to the direction of the incident neutron beam. The azimuthal angle ϕ is measured from the beam right in the horizontal scattering plane. Detector distances are given from target center to the surface of the scintillator for the charged particle (E) detectors and to the center of the scintillator volume for the neutron (N) detectors.

3.4.1 Charged Particle Telescope

The charged particle arms of the scattering chamber each housed an E-ΔE telescope. The ΔE detectors were 4.7 mg/cm^2 thick BC-404[1] plastic scintillator coupled to a Hamamatsu 1949-51[2] photomultiplier tube (PMT). They were covered with a thin ($\leq$ 8 μm) aluminum tent to reflect scintillator light into the PMT. The center of the ΔE detectors were located 8 cm from the CD_2 target. These detectors were designed to allow charged particles to pass through the detector, depositing part of their energy in the scintillator. The minimum energy required for a proton to traverse the ΔE detector and its aluminum tent was 1.7 MeV, while a deuteron needed 2.2 MeV for transmission. The main charged particle (E) detectors were located 61 cm beyond the ΔE detectors. They were also composed of BC-404 plastic scintillator. These detectors had a cylindrical geometry (10 cm radius, 5 mm thickness) and

[1]For full technical data sheet, please refer to www.detectors.saint-gobain.com/uploadedFiles/SGdetectors/Documents/Product_Data_Sheets/BC400-404-408-412-416-Data-Sheet.pdf

[2]For full technical data sheet, please refer to jp.hamamatsu.com/products/sensor-etd/pd002/pd394/H1949-51/index_en.html

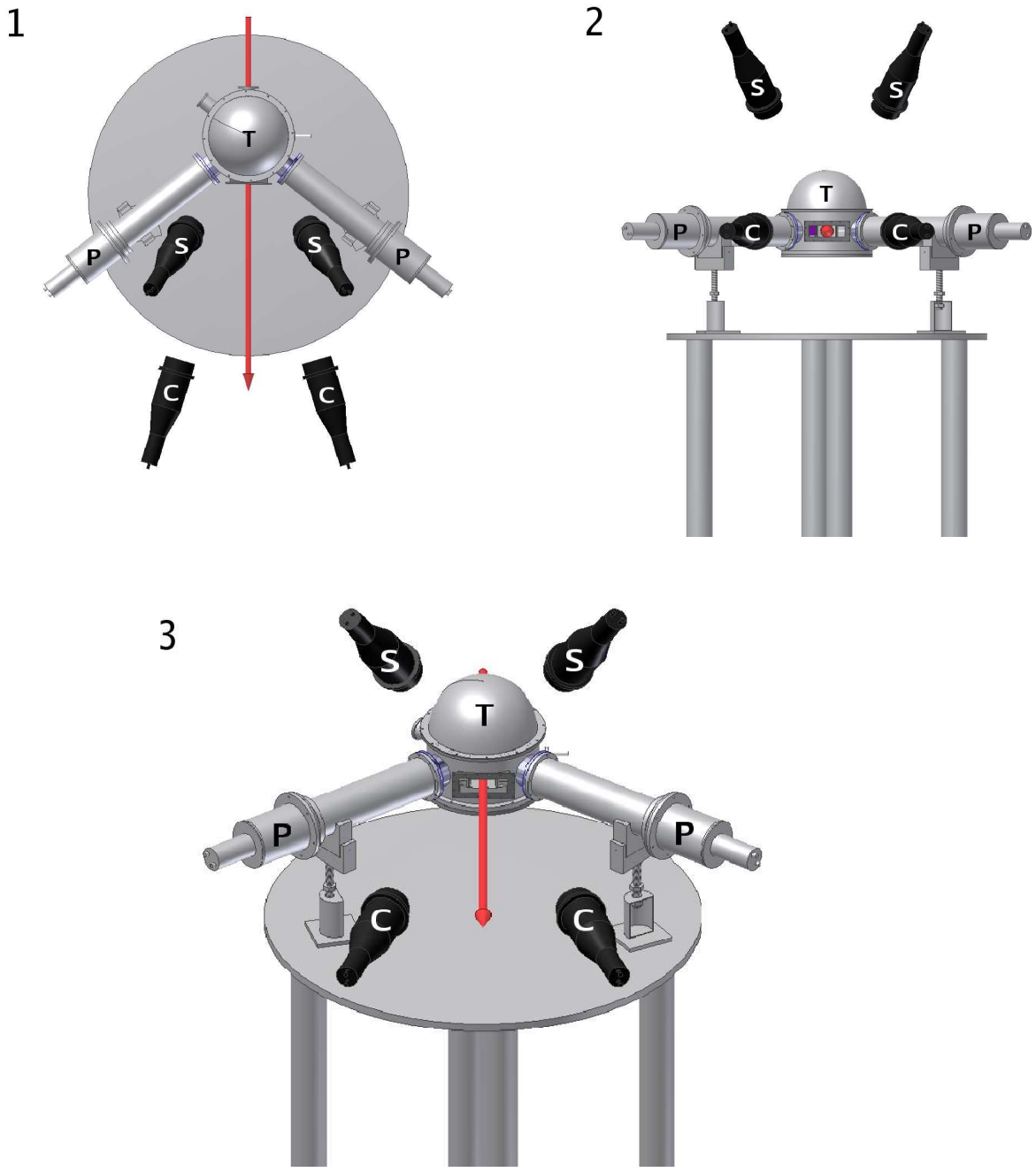

Figure 3.4: The three-dimensional renderings labeled 1, 2, and 3 are top, front, and angled views of the experimental setup, respectively, showing the target chamber (T), the charged particle arms (P), the SST (S) and CST (C) neutron detectors, and the neutron beam (red arrow). Please note that in the second image the neutron beam direction is out of the page.

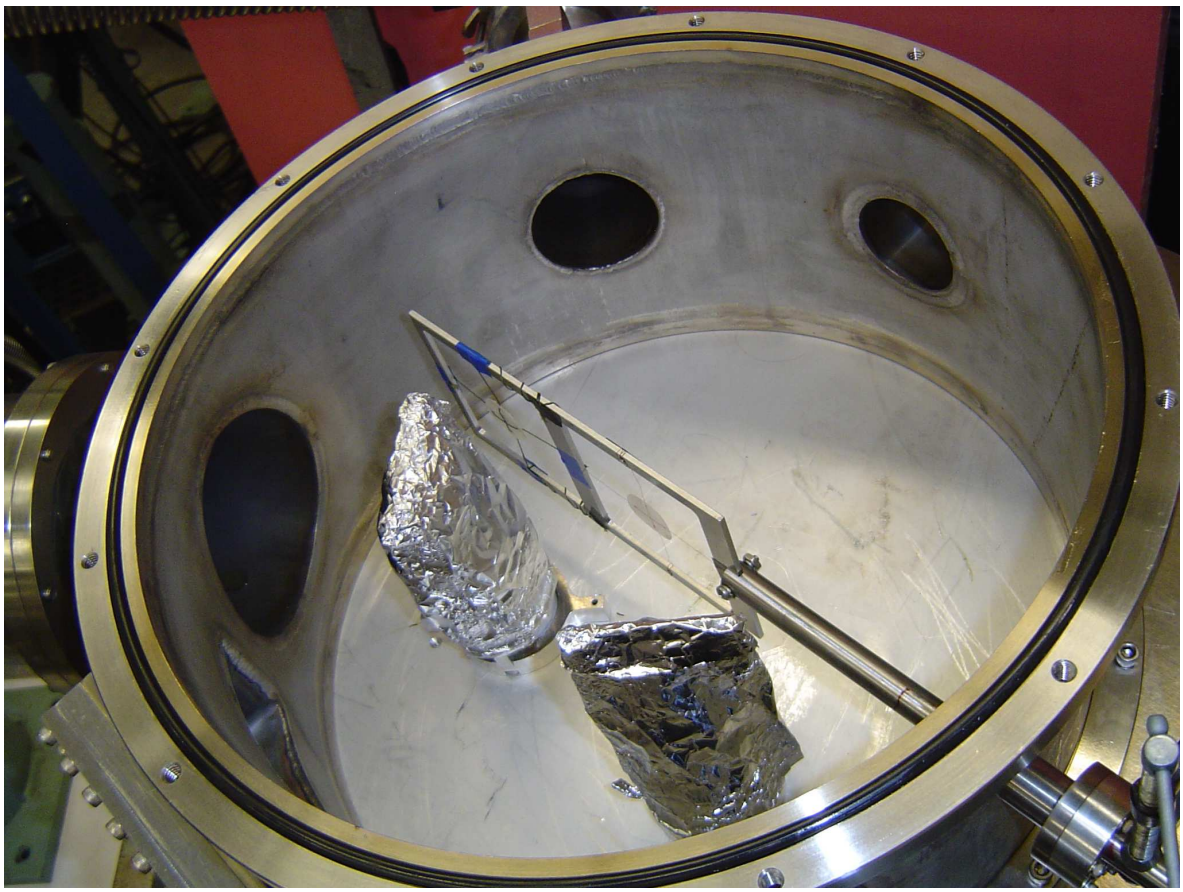

Figure 3.5: Photograph of the target chamber. The neutron beam enters the chamber through the port in the top right of the picture. The target rod holds the CD_2 foil used in the experiment and a CH_2 foil used for *np* elastic scattering. The two ΔE detectors are underneath the aluminum foil tents used to reflect scintillated light into the photomultiplier tubes located directly beneath the chamber.

were coupled to a Hamamatsu H6527[3] PMT. The front face of the scintillator was covered with thin aluminum foil to serve as a light reflector and seal. The foil did not affect the ToF energy measurements with the exception of stopping the slowest charged particles. The BC-404 was chosen for its physical rigidity as well as its high light output and fast response time. Technical specifications on the BC-404 plastic may be found in Table 3.2.

Scintillator	BC-501A	BC-404
Light Output (% Anthracene)	78	68
Decay Time (ns)	3.2	1.8
Density (mg/cm^2)	0.874	1.032
Ratio H:C Atoms	1.212	1.100
Wavelength of Maximum Emission (nm)	425	408

Table 3.2: Scintillator Properties: Neutron detectors used BC-501A. The charged particle telescope used BC-404.

3.4.2 Neutron Detectors

All of the neutron detectors used in this experiment were of the same design. They were manufactured by the Bicron Corporation and were filled with BC-501A[4] liquid organic scintillating fluid before being purchased by TUNL. The fluid chamber consisted of an aluminum cylinder (12.68 cm diameter, 5.08 cm depth interior dimensions) capped by a 1 mm thick aluminum plate on one end and a glass window on the other. A Teflon tube connected to the liquid chamber was coiled around the cell to allow for thermal expansion of the fluid. The cell and tube are designed such that no gas bubbles are present in the active scintillating volume. The interior aluminum surfaces of the fluid chamber were painted with BC-622[5] reflective polyurethane resin so that scintillated light must exit through the glass window. This window is directly coupled to a 12.7 cm diameter model R1250 Hamamatsu[6] PMT encased in a mu-metal shield. BC-501A was chosen for its excellent pulse shaped discrimination (PSD) properties and its fast response time. Technical specifications on BC-501A scintillator fluid may be found in Table 3.2.

[3]For full technical data sheet, please refer to jp.hamamatsu.com/products/sensor-etd/pd002/pd394/H6527/index_en.html

[4]For full technical data sheet, please refer to www.detectors.saint-gobain.com/uploadedFiles/SGdetectors/Documents/Product_Data_Sheets/BC501-501A-519-Data-Sheet.pdf

[5]For full technical data sheet, please refer to www.detectors.saint-gobain.com/uploadedFiles/SGdetectors/Documents/Product_Data_Sheets/SGC_Detector_Assembly_Materials_Data_Sheet.pdf

[6]For full technical data sheet, please refer to jp.hamamatsu.com/products/sensor-etd/pd002/pd394/R1250/index_en.html

3.5 Electronics

The signals generated by the detectors used in this experiment were processed by the electronics circuit described in this section. The circuit may be broken down into three main parts: the neutron detector circuit (Figure 3.6), the charged particle detector circuit (Figure 3.7), and a trigger circuit (Figure 3.8). The signals generated by these circuits were then digitized and saved to a disk.

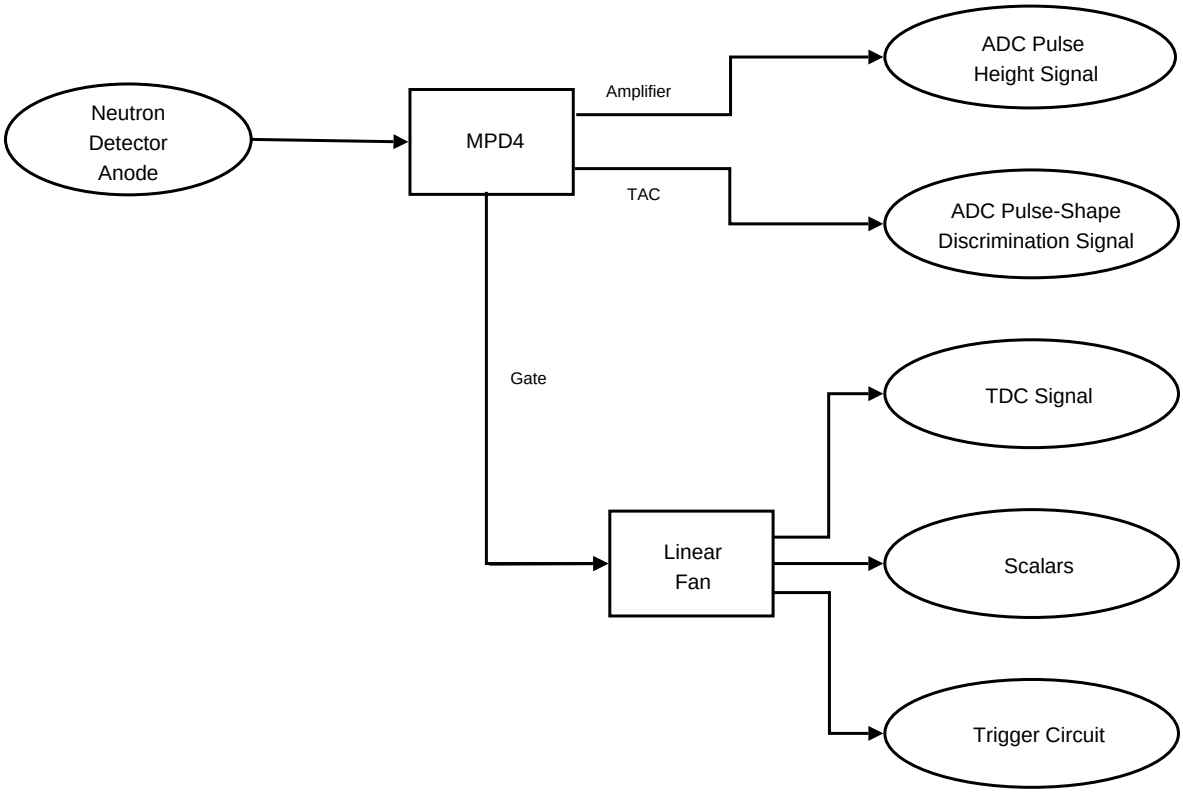

Figure 3.6: Neutron Detector Electronics Diagram.

The anode signal from the neutron detectors was sent directly into the mesytec MPD-4[7] particle discriminator module. This module was designed specifically for use with liquid scintillators and greatly simplified the electronics circuits needed to produce ToF and PSD measurements (see the theses of Crowell [Cro01] and Macri [Mac04] for comparison). This module produces three outputs: an amplified signal, a Time-to-Analog Converter (TAC) signal, and a gate signal. The amplified pulse height signal, proportional to the energy deposited in the scintillator, was sent directly to the Analog-to-Digital Converter (ADC). The TAC output was proportional to the decay time of the anode signal. Signals caused by γ-rays

[7]For full technical data sheet, please refer to www.mesytec.com/datasheets/MPD-4.pdf

decay faster than those from neutrons allowing discrimination between the particles using pulse-shape analysis techniques. This signal is also sent directly to the ADC and will be referred to as the PSD signal. The gate signal is a negative logic signal produced by the constant-fraction discriminator circuit in the MPD-4 module when the input signal is greater than some adjustable threshold. This gate signal is split with a linear fanout; one signal is sent to the Time-to-Digital Converter (TDC), another to the scalar module, and the final to the trigger circuit.

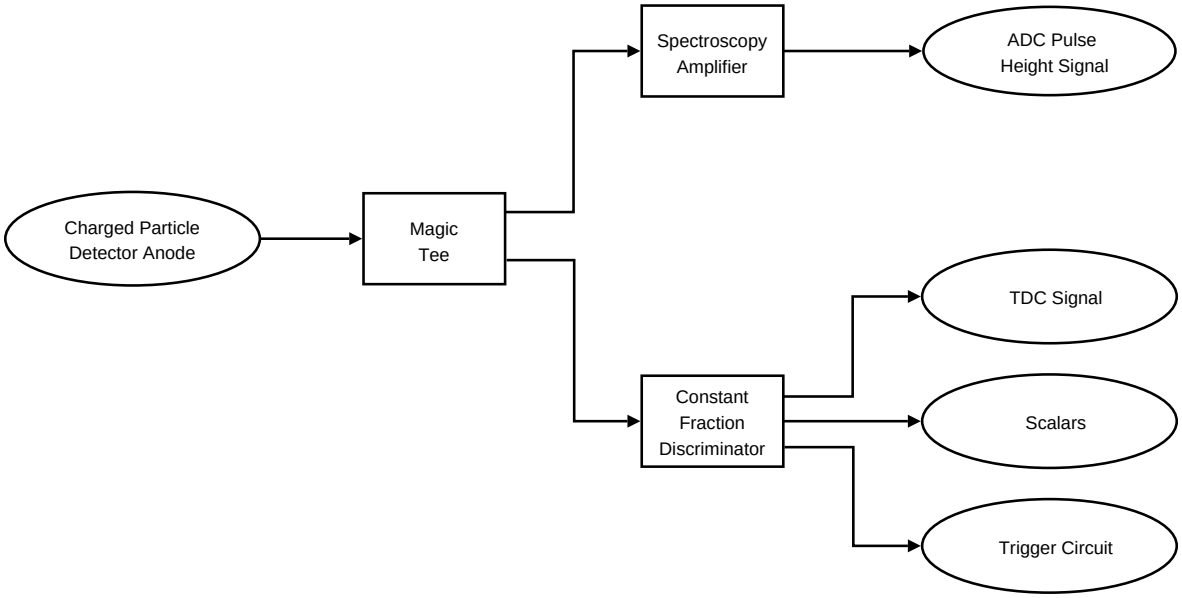

Figure 3.7: Charged Particle Detector Electronics Diagram.

The electronics for the E and ΔE detectors were identical, except the ΔE signals required an additional amplifier at the beginning of the circuit. The anode signal from the charged particle detectors was sent through a "magic tee", a passive voltage divider which matches the impedance of the two branches to prevent signal reflections. One branch was then sent through a spectroscopy amplifier and then into an ADC channel to provide pulse-height information. The other branch was sent to a constant fraction discriminator which produced a negative logic pulse if the signal was above the threshold. This logic pulse was fanned out to the TDC, the scalar module, and the trigger circuit.

The trigger circuit produced logic signals that were used to start the data acquisition system (DAQ) digitization and data readout sequence for each event. Signals from the neutron detectors were used to trigger the DAQ during γ-source energy calibration runs. During normal data runs, triggers were generated from the coincidence of same-side E-ΔE detector

signals. These triggers would be vetoed if the ADC, TDC, or DAQ were busy processing another event. The TUNL source/beam box was used to switch the DAQ trigger logic between calibration runs and *nd* breakup runs. This box put an open circuit on the output when set to beam and generated a constant voltage at the level of a logical "true" on the output when set to source.

The ADC and TDC used in this experiment were 4096 channel CAEN models V775[8] and V785[9], respectively. The TDC was set to a 600 ns range. The logic signals were counted with a SIS 3800[10] Scalar module. Along with the scalars mentioned above, we also recorded the triggers both before and after being vetoed, a 60 Hz clock both vetoed and unvetoed, the beam current integration (BCI), and several other unused or redundant quantities. Event data and scalars were buffered into the memory of a MVME 5100[11] Single Board Computer before being transferred to the main DAQ computer where they were saved to a disk using CEBAF Online Data Acquisition (CODA) software. An event consisted of eight pulse height signals, the eight timing signals, the four neutron PSD signals, and several other quantities which were not used in data analysis.

[8]For full technical data sheet, please refer to www.caen.it/nuclear/product.php?mod=V775
[9]For full technical data sheet, please refer to www.caen.it/nuclear/product.php?mod=V785
[10]For full technical data sheet, please refer to www.struck.de/sis3800s.pdf
[11]For full technical data sheet, please refer to www.mvme.com/manuals/MVME5100-SPEC.pdf

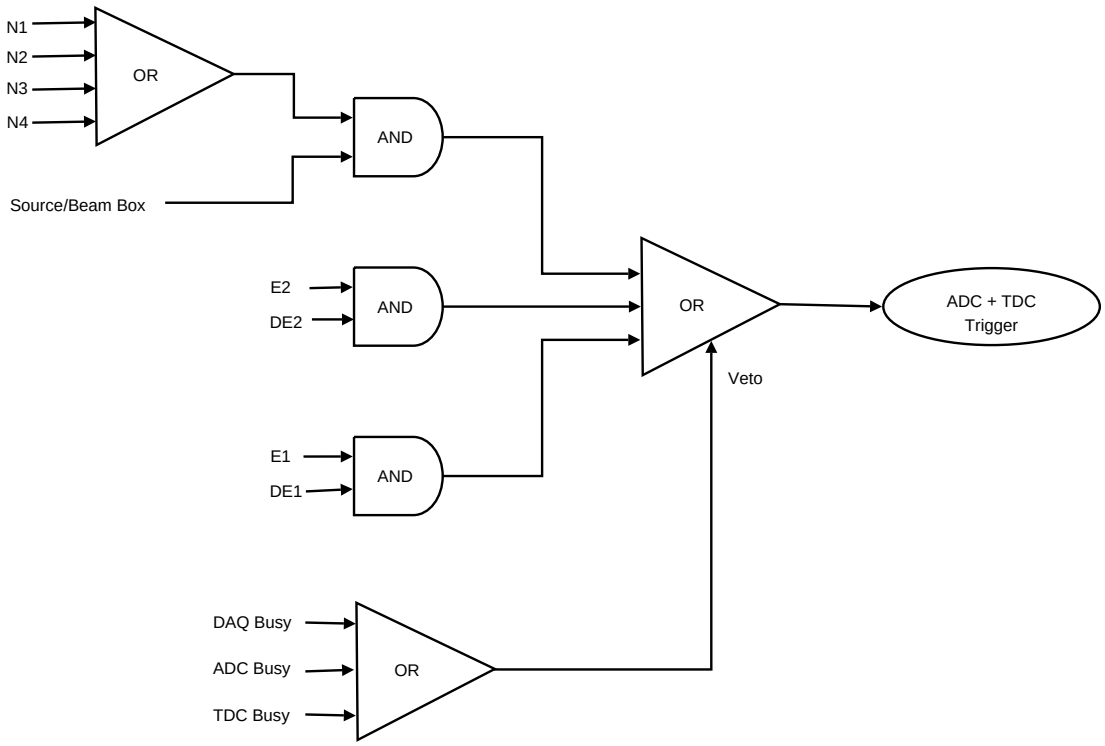

Figure 3.8: Diagram of the data acquisition trigger circuit.

4 Monte-Carlo Simulations

4.1 Introduction

The theoretical cross-section predictions for *nd* breakup and elastic scattering were made by Henryk Witała of the Bochum-Cracow theory group [Glö96]. These calculations are for point geometry. This means they assume a mono-energetic neutron beam with a target and detectors of infinitesimal size, which does not accurately represent the actual experiment. To make a meaningful comparison of experimental data with the theoretical predictions, Monte-Carlo (MC) simulations of the experiment were produced by Shigeyuki Tajima [Taj10] which averaged the point geometry calculations over the finite geometry of our experiment. Along with this averaging process several other effects were included in the simulation: the energy loss and attenuation of charged particles in the target and detectors, background events from low energy neutrons in the beam, and the time resolution of the detectors and electronics. This chapter will begin with a description of the composition of the point geometry cross-section libraries used in the simulation. The details of the *nd* elastic scattering and breakup Monte-Carlo simulations will then be provided.

4.2 Cross-Section Libraries

The *nd* elastic scattering cross-section library was fairly simple. It contained differential cross sections for the $^2H(n,n)^2H$ reaction in the CM frame calculated using the CD-Bonn [Mac01a] potential model for incident neutron energies from 0.5 to 20 MeV in 0.5 MeV steps. At each energy, the library contained cross-section values for neutron scattering angles in the center-of-mass system in 2.5° steps from 0° to 180°.

The *nd* breakup library was more extensive as a result of the additional degrees of freedom

in three-body kinematics. This library contains files consisting of point-geometry, five-fold differential cross sections, $d^5\sigma/d\Omega_n d\Omega_p dS$, in the laboratory frame, also based on the CD-Bonn [Mac01a] potential specified by four variables: the incident neutron energy, E_n^0, and the outgoing nucleon angles, θ_p, θ_n, ϕ_{np}. Please refer to Section 1.1 for definitions of these angles. These four parameters define the S-curve, or the kinematic locus which starts at the point where the proton energy is zero (S=0). Each file contains differential cross sections generated in 0.1 MeV steps along the S-curve.

The incident neutron beam energies used to produce the libraries were 15.6, 16.0 and 16.4 MeV for the "prompt" part of the neutron beam. The "source breakup" (SBU) neutrons were accounted for through the inclusion of incident neutron energies from 5.0 to 15.5 MeV in 0.5 MeV steps. A description of the measurement of the incident neutron beam energy spectrum is included in Appendix E. Definitions of prompt and source breakup neutrons may also be found there. Figure E.2 shows the energy distribution of the incident neutron beam. The cross-section libraries were composed to span 1-2° beyond the physical angular acceptance of the detectors to ensure complete coverage. The angular ranges and step sizes for the CST and SST configurations incorporated in the libraries are summarized in Table 4.1. In all more than 60,000 files for different combinations of E_n^0, θ_p, θ_n, and ϕ_{np}, each containing on average about 175 points along the S-curve, had to be included in the breakup cross-section library.

Configuration	θ_n (°)	$\Delta\theta_n$ (°)	θ_p (°)	$\Delta\theta_p$ (°)	ϕ_{np} (°)	$\Delta\phi_{np}$ (°)
CST	13.0-24.0	1.1	46.0-58.0	1.0	159-180	3.0
SST	44.5-59.5	1.5	46.0-58.0	1.0	104-136	3.0

Table 4.1: Angular ranges and step sizes used to generate theoretical cross-section libraries for the *nd* breakup Monte-Carlo simulation.

4.3 Elastic-Scattering Simulation

The integrated target-beam luminosity obtained over the course of this experiment was determined by an *nd* elastic scattering measurement taken concurrently with the primary breakup measurement. The recoil deuterons were detected in the charged-particle arm. However, in exiting the target and traversing the ΔE detector, there was significant energy loss and approximately 40% of the scattered deuterons were actually stopped before reaching the E detector. In order to estimate the deuteron attenuation, determine the shape of the elastic ToF spectrum, and model backgrounds from SBU events, a Monte-Carlo simulation of the elastic scattering process was required.

The first step in the elastic simulation was to select an incident neutron beam energy. The incident beam energy distribution shown in red in Figure E.2 was used to weight each event. An interaction location within the volume of the target and a polar and azimuthal scattering angle within the acceptance of the charged particle (E) detector were then chosen, completely defining the reaction kinematics. The cross section for this scattering event was then calculated from the neutron scattering angle in the CM frame through an interpolation of the elastic cross-section library, and this was subsequently stored after conversion into the laboratory frame. This sampling process was then repeated until the statistical uncertainty was insignificant when compared with the 1% systematic uncertainty of the cross-section weighting.

The energy of the elastic deuterons immediately after the reaction was calculated based upon the incident energy and scattering angle. The mean energy loss attained by a deuteron of this energy as it encounters the experimental setup was then estimated using the Fortan code, "Babel." This code was developed at TUNL in the early 80's and calculates the energy loss of ions in matter using the relativistically correct Bethe formula by dividing the path through the material into regions of small energy loss [Sel64, Jan66]. The energy after passing through the ΔE detector was then used to determine the ToF of the deuteron between the ΔE and E detectors. If a particle was stopped in the target or in the ΔE detector, it was assigned an unphysical negative ToF. A Gaussian time-smearing function with a central value of zero and a full-width half-maximum (FWHM) of 2.0 ns was used to shift the actual ToF randomly, thereby simulating the time resolution of the charged particle detectors and the processing electronics. The FWHM value for the time-smearing function was varied in 0.5 ns steps up to 3.0 ns before settling on the 2.0 ns value which proved the best fit to the measured ToF spectrum. This fit was then used for the normalization. A sample ToF spectrum generated by the elastic Monte-Carlo is shown in Figure 5.9.

4.4 Breakup Simulation

The Monte-Carlo simulation for the *nd* breakup process begins in the same fashion as the elastic simulation, with the choice of the incident neutron energy, E_n^0. The neutron energy was sampled from 5.0 to 16.34 MeV weighted by the incident beam energy distribution shown in in red Figure E.2. While the measured distribution contains neutrons below 5 MeV, they are not included in the simulation as protons from these breakup events would not have sufficient energy to be detected. A reaction location was then chosen in the target volume, followed by detection locations on the surface of the proton detector and within the volume of the neutron detector. This determines the outgoing nucleon angles, θ_p, θ_n, ϕ_{np}. The combination of incident neutron energy and outgoing nucleon angles defines the kinematic locus or

S-curve. The detected neutron energy, E_n, is then uniformly sampled up to 8.2 MeV for the SST configuration and 14.66 MeV for the CST. The simulation must then solve the three-body kinematic equation which imposes energy and momentum conservation to determine the momentum vectors of all three outgoing nucleons. There are three possibilities: either one, two, or no solutions may be found. If a single solution is found, the three momenta, cross section, and neutron detection efficiency are stored and the simulation proceeds. If two solutions are found, one is chosen at random and the parameters are stored. If no solution is available, nothing is stored. The sampling process was repeated until statistical uncertainty was insignificant compared with systematic errors. A sample S-curve describing the three possible solutions to the kinematic equation for the SST configuration is shown in Figure 4.1.

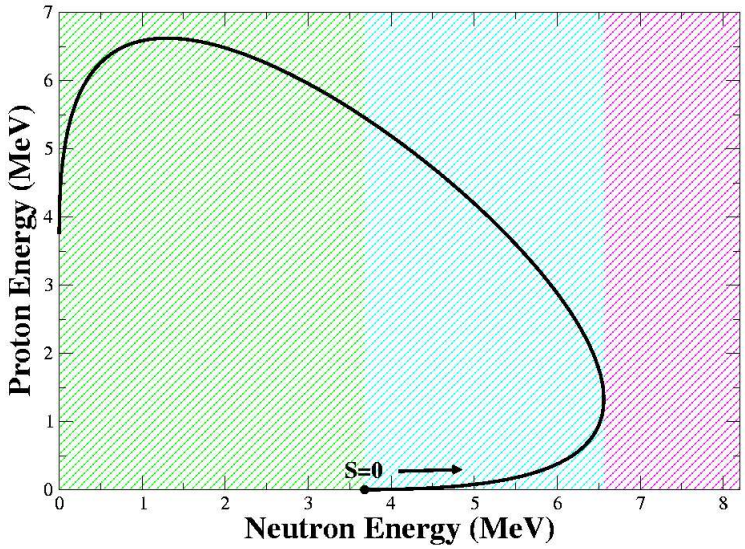

Figure 4.1: Sample SST kinematic locus or S-curve. It is defined such that S=0 is located at the intercept with the neutron energy axis and S increases counterclockwise. This particular locus was defined by $E_n^0 = 16.0$ MeV, $\theta_p = 51.3°$, $\theta_n = 51.5°$, and $\phi_{np} = 59.7°$. A uniform sampling of the detected neutron energy, E_n, will find either zero(red), one(green), or two(blue) possible solutions to the kinematic equation after energy and momentum conservation are imposed.

The effective breakup cross section for detecting coincident events with our experimental setup drops off significantly with increasing E_n as compared to point geometry cross sections at the central detector angles, as shown in Figure 4.2. There are two processes which contribute to this effect which will be referred to as geometric acceptance and proton energy

threshold acceptance. Figure 4.3 plots the acceptance factors as a function of E_n for these processes as well as the net effect. The geometric acceptance is defined as the probability of finding a solution to the three-body kinematic equation for a randomly chosen E_n, taking into account all possible S-curves allowed by the range of incident neutron energies and detection angles. This effect is much more pronounced in the SST configuration than in the CST because the SST is the kinematic extreme of nd breakup. Protons that exit the target with an energy less than about 2 MeV were stopped by the ΔE detectors. A higher E_n leaves less energy available to the outgoing proton, decreasing its probability of detection. Both of these effects also come into play at very low E_n; however this has no bearing on our experimental results as a low energy threshold is applied to the neutron detectors.

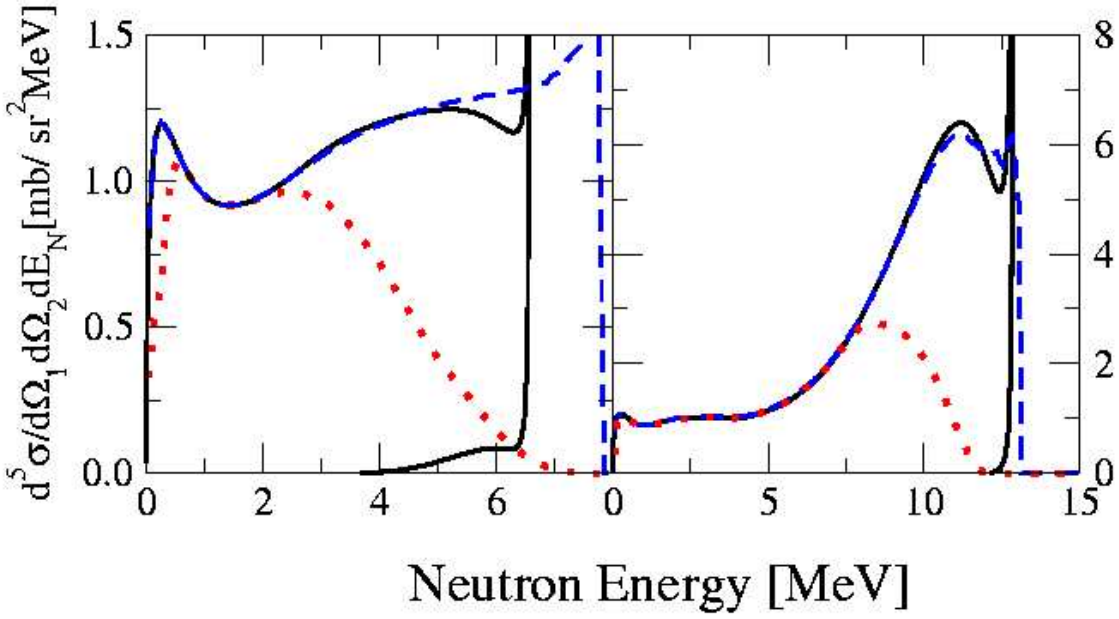

Figure 4.2: Comparison of Monte-Carlo simulated cross section to point geometry. The graph on the left(right) corresponds to the SST(CST) configuration. The solid black line is the point geometry cross section for the central detector angle at 16 MeV. The dashed blue line gives the average cross section for all kinematically allowed configurations sampled over the angular range of the detectors and the incident neutron energy of the prompt neutron beam. The dotted red line represents the effective cross section for the experimental setup with acceptance factors applied. The double-valued regions of E_n in the black curve correspond to the two possible solutions to the kinematic equation. The dashed blue curve produced by the Monte-Carlo simulation sums these two contributions.

The final step in the breakup simulation was to adjust the particle energies to replicate the experimental measurement. First the energy loss of the protons as they exited the target and traversed the ΔE detector was calculated. This was done using the "Babel"

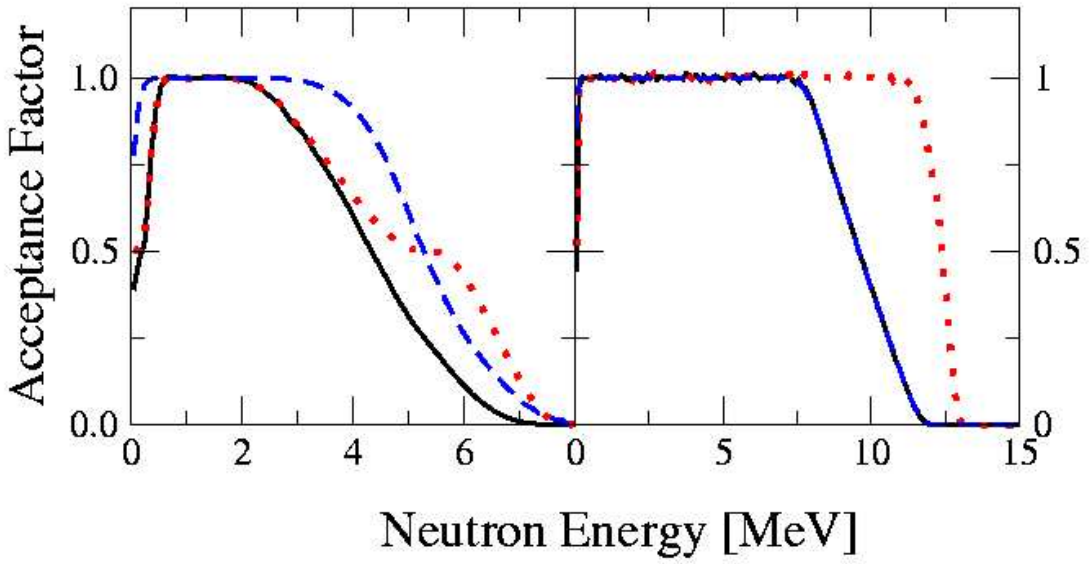

Figure 4.3: Acceptance factors for coincident *nd* breakup events. The graph on the left(right) corresponds to the SST(CST) configuration. The dotted red curve is the geometric acceptance factor and the dashed blue curve is the proton energy threshold acceptance factor. The solid black curve is the total acceptance factor, the product of the other curves.

code [Sel64, Jan66] in the same manner as for the elastic simulation. The actual ToF between the ΔE and E detectors was then calculated using the real flight path. Likewise the real ToF between the time the proton triggered the ΔE and the time the neutron interacted with its detector was calculated. These times were each adjusted using a randomly generated time shift having a Gaussian profile with a FWHM of 2.0 and 2.5 ns for the protons and neutrons, respectively. A "smeared" proton energy was then calculated using this adjusted ToF and the center-to-center distance between faces of the ΔE and E detectors. This should correspond to the proton energies measured in the actual experiment. The same procedure was repeated for the neutron using the distance from the target to the center of the neutron scintillator volume. Babel was then used in reverse to estimate the proton energy upon exiting the target. These smeared neutron and proton energies were used to produce the simulated loci in Figures 4.4 and 4.5 for the SST and CST configurations, respectively.

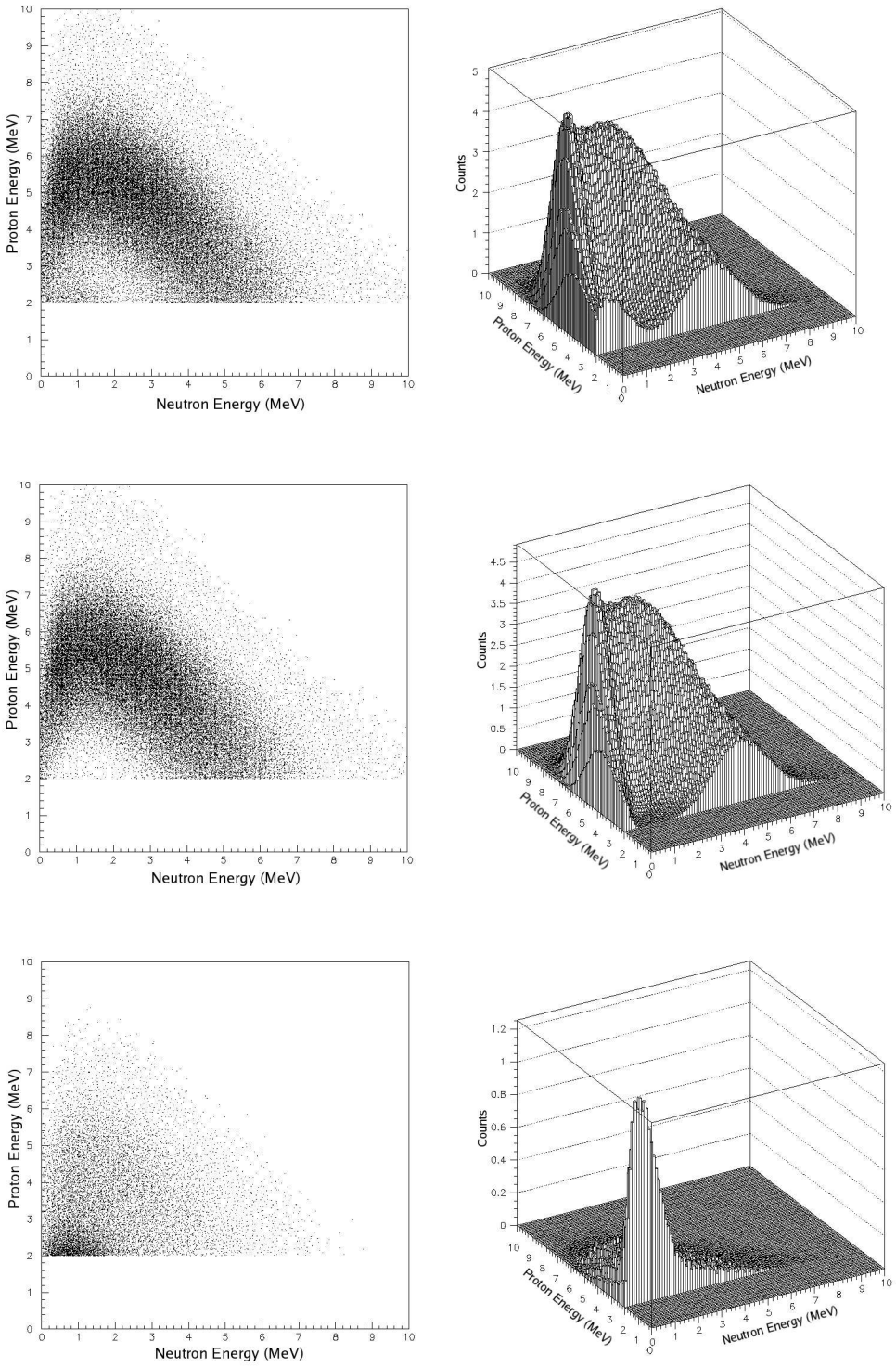

Figure 4.4: Monte-Carlo simulated SST counts for the complete experiment (top), prompt neutrons only (middle), and SBU neutrons only (bottom). The vertical scale of the 3D-plots is in thousands of counts.

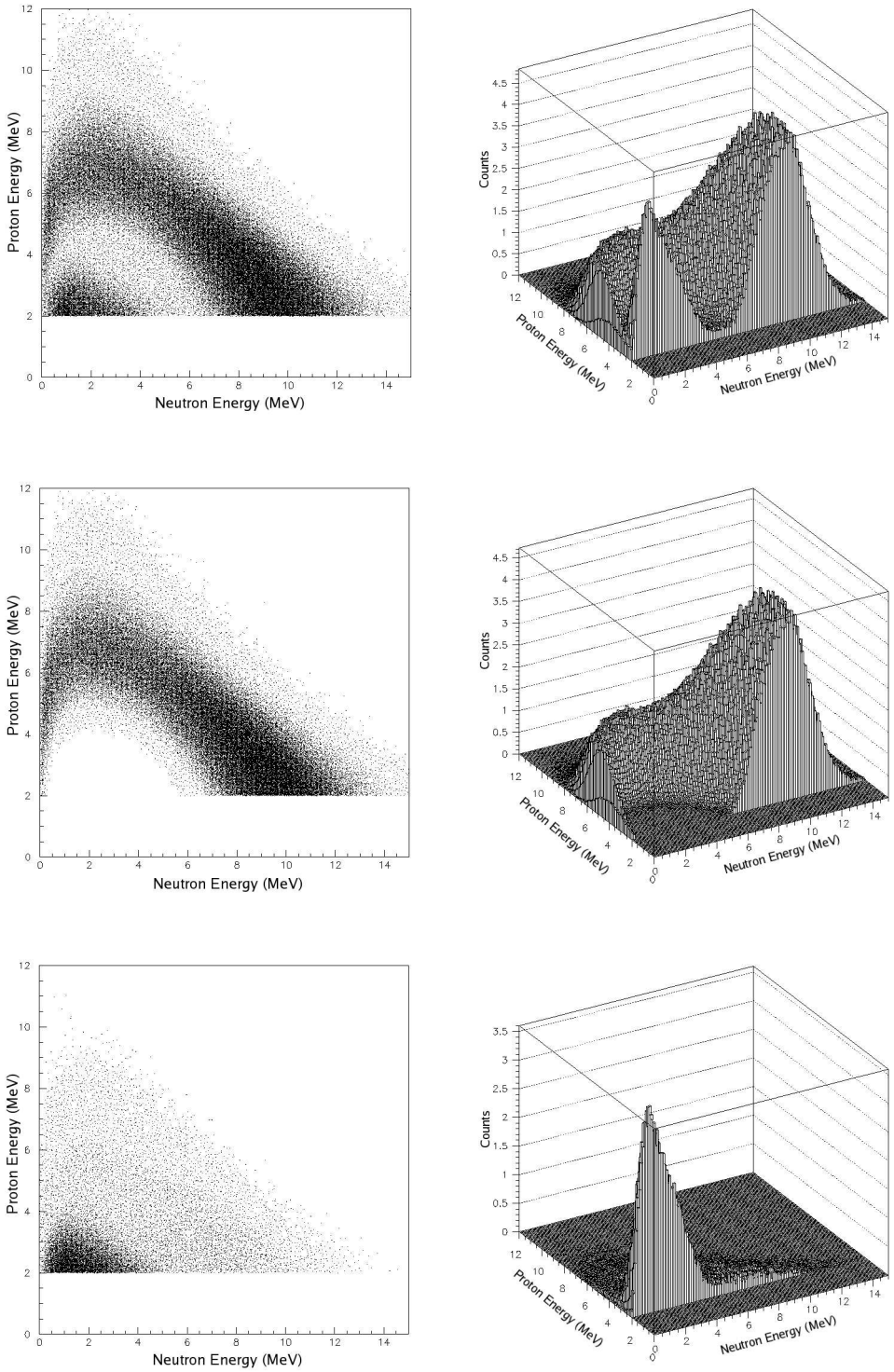

Figure 4.5: Monte-Carlo simulated CST counts for the complete experiment (top), prompt neutrons only (middle), and SBU neutrons only (bottom). The vertical scale of the 3D-plots is in thousands of counts.

5 Data Analysis

5.1 Introduction

The data analysis for this experiment was broken into two separate parts. The first was to determine the number of valid experimental breakup coincidence events as a function of detected neutron energy. The second was to use the effective breakup cross section determined from the Monte-Carlo simulation to predict this same quantity, thus comparing theory to experiment. The relative discrepancy between the measured and predicted counts should be identical to the relative discrepancy between the actual cross section and the one predicted by Faddeev calculations using the CD-Bonn potential. One advantage to this method of data analysis is that statistical and systematic uncertainties may be clearly separated into the experimental findings and theoretical predictions, respectively.

The data for this experiment were accumulated over the course of eight separate accelerator runs. Each of these runs lasted between 1-2 weeks and data were taken around the clock whenever possible. Neutron detector biases and thresholds were monitored daily during these runs using ^{137}Cs and ^{22}Na γ-sources and proved to be extremely stable. Data analysis was performed on each run individually and the results were compiled afterwards. Table 5.1 contains the dates and percent of the total data that each run represents. This percentage was determined by calculating the integrated beam flux for each run from the *nd* elastic scattering measurements.

5.2 Determining the Measured Counts

This section will describe the method for producing the spectrum of measured *nd* breakup coincidence events. The first step in this process was determining which events contain both

Run	Date	Percent of Total Data
1	June 2008	8.7
2	August 2008	17.1
3	September 2008	14.1
4	October 2008	15.1
5	December 2008	7.8
6	January 2009	14.2
7	March 2009	13.1
8	April 2009	9.8

Table 5.1: Data batches. The dates and percentage of total data obtained in each accelerator run are given above. Each run was analyzed independently and the results were compiled afterwards. The percentages were determined from the integrated neutron beam flux for each run.

a proton and a neutron. The techniques for separating proton and neutron events from events containing deuterons, electrons, γ-rays, and noise are collectively known as particle identification (PID). The next step was to determine the energies of the protons and neutrons. The coincidence events were then plotted on the E_p versus E_n plane where a gate is applied to the region of interest. Events falling within this gate were projected into 1 MeV bins along the E_n axis. To create the final spectrum, an accidental event subtraction was required.

5.2.1 Particle Identification

In order to find *nd* breakup events among the larger number of background events, protons and neutrons detected in coincidence had to be identified. The *nd* elastic normalization required the identification of deuterons. The charged particle arms detected events caused by protons, deuterons, and electrons. The neutron detectors could detect both neutrons and γ-rays. Spectra from both detectors also contained null events and electronic noise. The processes used to sort events by which particles they contained is outlined below.

In the neutron detectors, neutrons scatter elastically off of protons in the scintillating fluid while γ-rays interact predominantly through Compton scattering with electrons. These charged particles excite molecules in the scintillator which produce light when they relax back into their ground states. Protons have a higher rate of energy loss than electrons providing a high density of excited molecules in a region of the scintillator. This high density of excited molecules results in increased intermolecular attractions which hinder their relaxation to the ground state [Leo94]. The net effect of this process, known as pulse-shaped-discrimination (PSD) is that anode signals produced by neutrons take longer to decay than signals from γ-rays. Figure 5.1 is a plot of the energy deposited in the scintillator (pulse height) versus

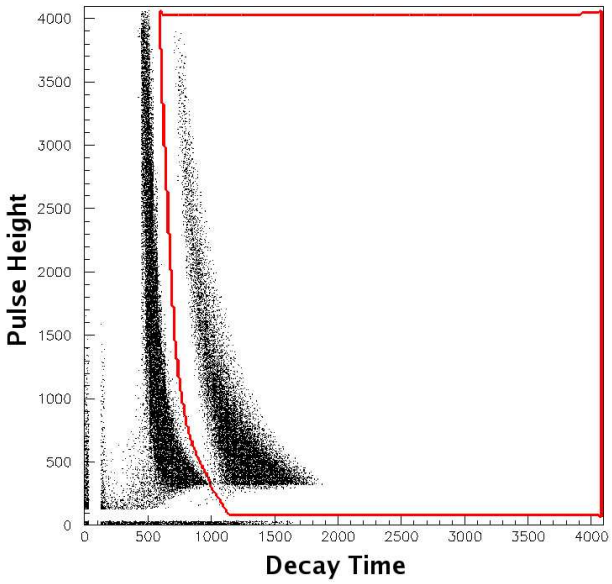

Figure 5.1: Neutron PSD spectrum. The graph shows the total energy deposited in the scintillator (pulse height) versus the decay time of the anode signal. The red gate was set around the neutrons. Counts outside the gate were caused by γ-rays. The units on both axes are arbitrary.

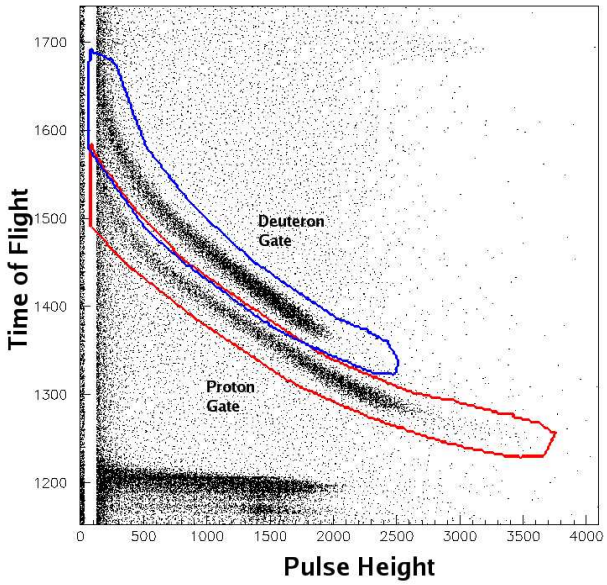

Figure 5.2: Charged particle identification spectrum. The plot of pulse height vs. ToF separates particles with the same energy but different masses into bands. The blue gate is for deuterons, the red is for protons. The units on the axes are arbitrary.

the decay time of the anode signal. Neutrons and γ-rays are clearly separated into bands. A two-dimensional gate (shown in red) is used to identify neutrons in the data analysis.

The process for distinguishing between the protons, deuterons, and electrons was fairly simple. Pulse height signals proportional to charged particle energy were recorded as well as the time-of-flight (ToF) between the E and ΔE detectors. Particles with the same kinetic energy but different masses travel at different velocities. This phenomenon separates the different species of charged particles into distinct bands when pulse height versus ToF is plotted as in Figure 5.2. During data analysis, two-dimensional gates were placed around the deuteron band (blue) and the proton band (red).

5.2.2 Energy Calibration

To determine particle energies, ToF techniques were used. Charged particle and neutron detector ToF spectra are shown in Figures 5.3 and 5.4, respectively. The signal from the ΔE detector was used to start the TDC clock. To extract an actual time from these spectra, two basic pieces of information must be determined: the time interval represented by one TDC channel and a channel in the spectrum with a known time. Once these flight times were known, particle energies could be determined using the formula: $E = \frac{1}{2}m(\frac{d}{t})^2$. Here the distance traveled, d, was determined by the experimental geometry and the particle mass, m, to be used was determined using the particle identification gates discussed in Section 5.2.1.

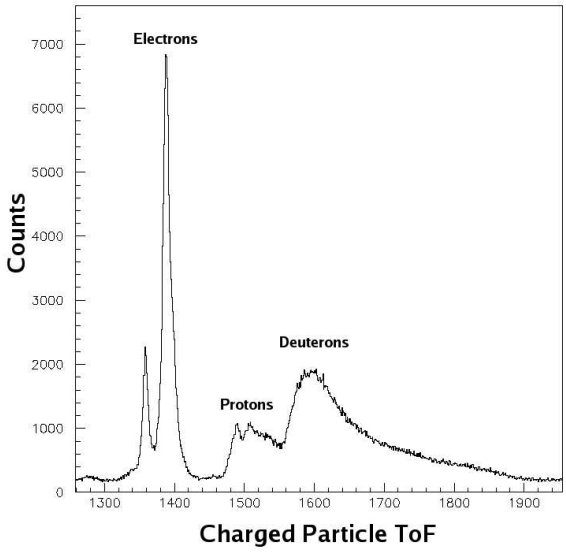

Figure 5.3: Charged particle ToF spectrum. The units of the time spectrum are TDC channels (1 TDC channel = 0.135 ns). Time increases to the right.

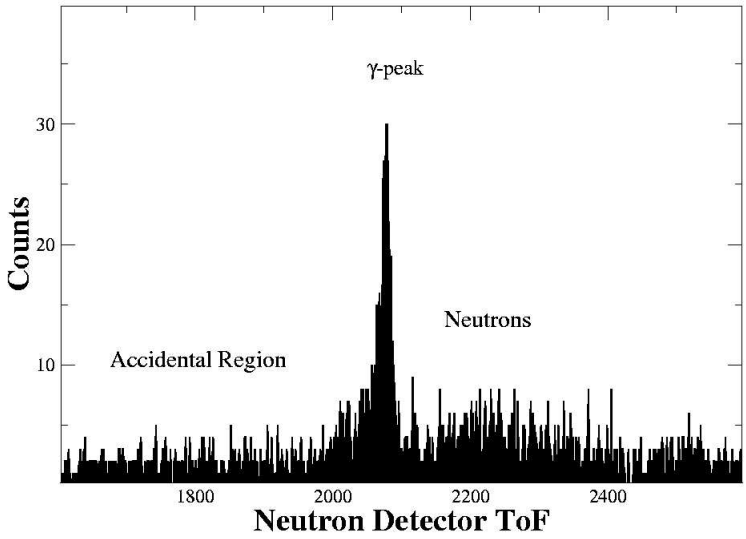

Figure 5.4: Neutron detector ToF spectrum. The units of the time spectrum are TDC channels (1 TDC channel = 0.135 ns). Time increases to the right.

To determine time interval per TDC channel, the Ortec 462 Time Calibrator[1] was used. This device provided a start signal for the TDC and then stop signals every 40±1 ns for a 1.28 μs time interval. Each of the TDC inputs was tested in this manner. The spectra from these tests showed a series of five narrow peaks each separated by 296±4 TDC channels. Thus each TDC channel had a width of 0.135±0.002 ns.

Elastic scattering was used to find a channel in the spectrum with a known time. Both *nd* and *np* elastic scattering were performed detecting the neutron and scattered charged particle in coincidence. To make this measurement, the neutron detectors had to be moved from their breakup locations to a polar scattering angle of 37.6° for *np* scattering and 52.1° for *nd* scattering. These detectors were located in the horizontal scattering plane, opposite their coincident charged particle arm. These measurements were taken at incident neutron beam energies of 16.0 and 19.0 MeV. The elastic scattering Monte-Carlo simulation discussed in Section 4.3 was used to model charged particle energy loss in the target and ΔE detector. The maximum in the elastic spectum was determined for both the simulation and measurement for the four possible combinations of *np* and *nd* elastic scattering at 16 and 19 MeV. A linear fit of these four points was then performed to obtain the TDC channel corresponding to

[1]For full technical data sheet, please refer to //www.ortec-online.com/download.asbx?AttributeFileId=95fdab9e-2fa2-4559-91e2-29d5dfe84110

t=0. The there was excellent agreement between the slope of these linear regressions and the 0.135 ns/ch value determined using the Time Calibrator. The procedure used for the charged particle arms and the neutron detectors was virtually identical. The only difference being that, for the neutron detectors, the ToF of the coincident charged particle between the target and ΔE detector had to be added to the time interval measured by the TDC because the ΔE detector provided the start signal for the clock.

5.2.3 Locus Projections and Background Subtraction

Once neutron-proton coincidences have been identified using the methods described in Section 5.2.1, and their energies determined as described in Section 5.2.2, they are plotted on the E_p versus E_n plane. In an idealized experiment, using a neutron beam with a 16 MeV delta-function energy spectum and point-geometry beam, target, and detectors, all coincident counts would lie on the kinematic loci shown in Figure 5.5. However, as a result of the finite geometry of the experimental setup, the measured coincidences are found in a band around this ideal locus. The location and width of this band was determined using the Monte-Carlo simulation described in Section 4.4. A two-dimensional gate was set around this region of the proton-versus-neutron-energy spectrum.

Along with the genuine 16 MeV *nd* breakup coincidence events of interest, background

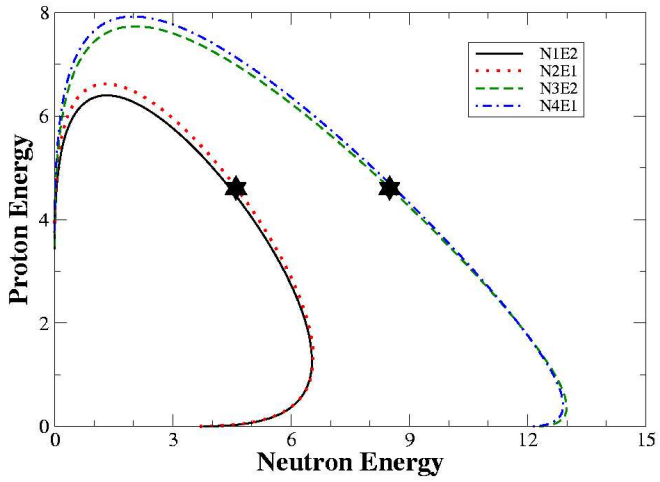

Figure 5.5: Point geometry kinematic loci based on central detector angles. The locations of the SCRE conditions are indicated by the stars. The N1-E2 and N2-E1 loci are the SST configuration; the other two are the CST configuration.

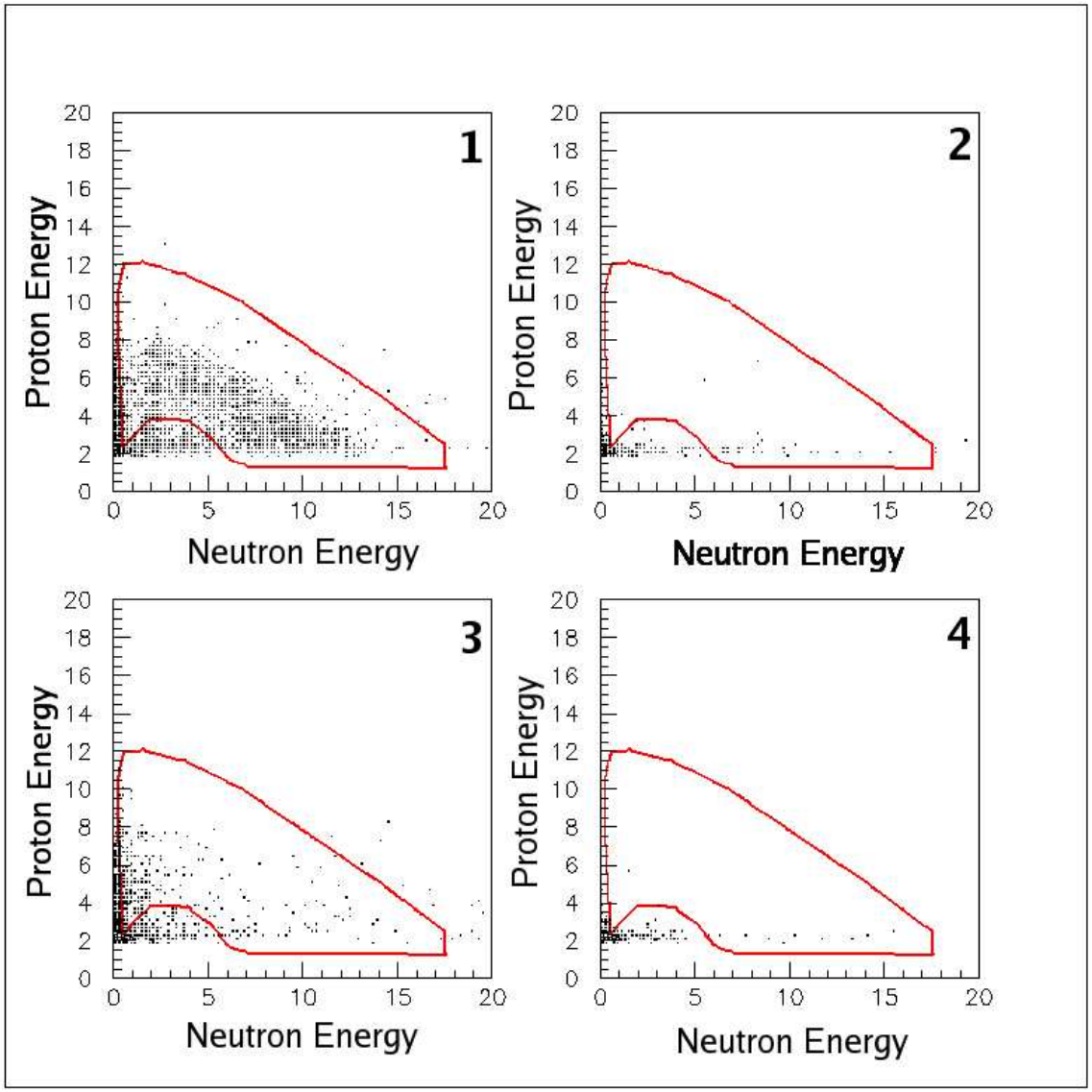

Figure 5.6: Measured locus and accidental spectra for N3-E2 CST detector pair. The number in the top right corner of each spectum indicates the coincident event type as defined in Table 5.2. The red gate defines the region where 16 MeV *nd* breakup events are kinematically allowed. The units on all axes are MeV.

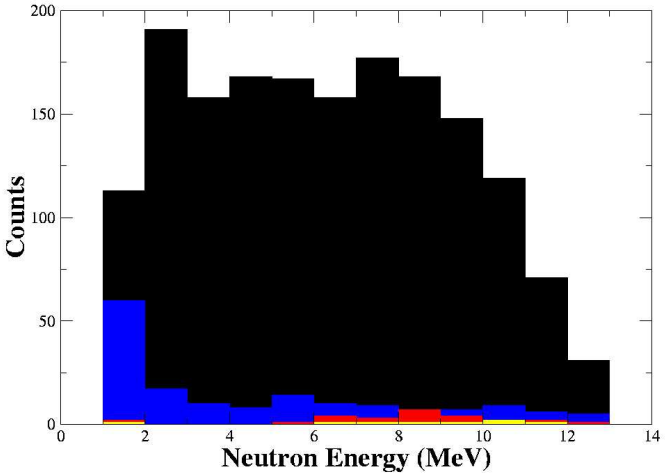

Figure 5.7: Projections of the counts in the 2D-gates shown in Figure 5.6 onto the neutron energy axis: The four colors on the graph correspond to the following coincident event types as defined in Table 5.2; black ⇒ 1, red ⇒ 2, blue ⇒ 3, and yellow ⇒ 4. This graph corresponds to the N3-E2 CST detector pair.

coincidence events are measured as well. Accidental coincidences may occur between time-uncorrelated events that are misidentified as breakup events. These events form a uniform background in the both the proton and neutron time spectra. One or both of the signals in a coincident event may be caused by processes uncorrelated with *nd* breakup. To remove these events from the analysis, unphysical regions of the timing spectra corresponding to particles traveling faster than the speed of light were used to determine the magnitude of the accidental background. The physical region of the spectra containing *nd* breakup events will be referred to as the "True + Accidental" (T+A) region and the unphysical region will be referred to as the "Accidental" (A) region. Gates of identical shape were set on the T+A and A regions. To assign energies to the A region, the ToF of events in that region were shifted such that the A gate identically overlapped with the T+A gate.

There are four possible combinations of proton and neutron event types as shown in Table 5.2. Two-dimensional spectra of the N3-E2 CST detector pair for each of these event types are graphed in Figure 5.6. Please note that the proton energies were adjusted to account for energy loss in the ΔE detector using the "Babel" charged particle energy loss code. The measured locus containing the true *nd* breakup events along with background coincidences corresponds to event type 1. The same 2D-gate was applied to each event type and the coincident events within the gate were projected in to 1 MeV bins along the neutron energy

Coincidence Event Type	Proton Event Type	Neutron Event Type
1	T+A	T+A
2	A	T+A
3	T+A	A
4	A	A

Table 5.2: Identification of true and accidental event types: The coincident event type will be used to refer to the combination of proton and neutron event types in this section.

axis. These projections are displayed in Figure 5.7. The measured locus has coincident events of type 2, 3, and 4 as backgrounds. The accidental spectra for coincident events of type 2 and 3 each have events of type 4 as a background. In order to remove the accidental background from the measured locus the following formula must be applied:

$$\begin{aligned} Y(T) &= Y(1) - [Y(2) - Y(4)] - [Y(3) - Y(4)] - Y(4) \\ &= Y(1) - Y(2) - Y(3) + Y(4). \end{aligned} \tag{5.1}$$

Here Y(T) is the estimated yield of true *nd* breakup events in a particular neutron energy bin and Y(i) is the projected yield of the i^{th} coincident event type into that same bin. The statistical uncertainty for the true yields is given by the following formula:

$$\Delta Y(T) = \sqrt{Y(1) + Y(2) + Y(3) + Y(4)}. \tag{5.2}$$

There is also a source of non-accidental background which may not be accounted for by the methods described above. The neutron beam used in this experiment contains low energy (SBU) neutrons as defined in Appendix E. The Monte-Carlo simulation discussed in Section 4.4 was used to determine the fraction of true *nd* breakup counts in each neutron energy bin which were caused by these SBU neutrons. The results of this simulation for the N3-E2 CST detector pair are shown in Figure 5.8.

5.3 Determining the Predicted Counts

To predict the yield of *nd* breakup events Y_{ndbu} expected in an energy bin along the E_n axis from the effective cross section $d^5\sigma/d\Omega_n d\Omega_p dE_n$ produced by the Monte-Carlo simulation, the following formula must be applied:

$$Y_{ndbu} = \left(\frac{d^5\sigma}{d\Omega_n d\Omega_p dE_n} \right) \cdot t \cdot n \cdot \Omega_p \cdot \Omega_n \cdot \varepsilon_n \cdot \alpha_n \cdot \Delta E_n \cdot LT, \tag{5.3}$$

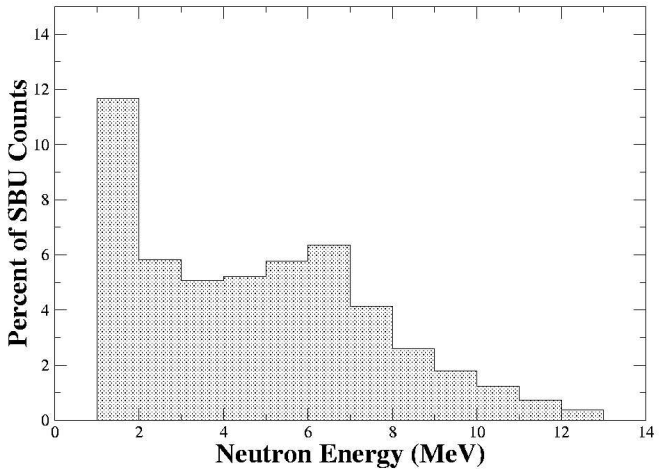

Figure 5.8: Estimated percent of measured breakup counts from SBU events. This background was estimated by the Monte-Carlo simulation described in Section 4.4. This graph corresponds to the N3-E2 CST detector pair.

where t, n, Ω, ε_n, α_n, ΔE_n, and LT stand for the target thickness, neutron beam flux, detector solid angle, neutron detector efficiency, neutron attenuation, energy bin width, and fractional live time of the data acquisition system, respectively. The proton detector is assumed to be perfectly efficient and proton attenuation is handled by the Monte-Carlo simulation; thus it is hidden in the effective cross section. The product of the target thickness, neutron beam flux, proton detector solid angle, and live time were determined via *nd* elastic scattering performed simultaneously with the *nd* breakup experiment. These quantities are related to the elastic cross section and yield as follows:

$$Y_{nde} = \left(\frac{d\sigma}{d\Omega}\right)_{nde} \cdot t \cdot n \cdot \Omega_p \cdot LT. \tag{5.4}$$

Many elastically scattered deuterons were stopped in either the target or ΔE-detectors and thus were not recorded. However, the total number of elastic scattering events is the quantity needed in Equation 5.4. This issue, along with the fact that the low energy region of the elastic deuteron spectrum was contaminated with substantial background noise, led to the adoption the following procedure for *nd* elastic scattering normalization.

The high energy region of the elastic deuteron spectrum was used in conjunction with the Monte-Carlo simulation discussed in Section 4.3 to determine the total elastic yield. The full

nd elastic yield was estimated using the following equation:

$$Y_{nde} = Y_{nde}^{HE} \cdot \left(\frac{Y_{MC} \cdot \left\langle \frac{d\sigma}{d\Omega} \right\rangle_{nde}}{Y_{MC}^{HE} \cdot \left\langle \frac{d\sigma}{d\Omega} \right\rangle_{nde}^{HE}} \right), \tag{5.5}$$

where the superscript, HE, indicates the yield or average cross section pertains to the high energy region of the deuteron spectrum. Combining Equations 5.3, 5.4, and 5.5 we obtain the following expression containing all quantities used to predict the nd breakup yields:

$$Y_{ndbu} = \left(\frac{d^5\sigma}{d\Omega_n d\Omega_p dE_n} \right) \cdot \Omega_n \cdot \varepsilon_n \cdot \alpha_n \cdot \Delta E_n \cdot \left(\frac{Y_{nde}^{HE} \cdot Y_{MC}}{Y_{MC}^{HE} \cdot \left\langle \frac{d\sigma}{d\Omega} \right\rangle_{nde}^{HE}} \right). \tag{5.6}$$

This section will begin with a discussion of the nd elastic scattering normalization, explaining the method for determining the term in parenthesis at the end of Equation 5.6. The remaining terms in this equation are all parameters pertaining to the detection of the neutron, as indicated by the subscript n, and will be discussed subsequently. The section will conclude with a summary of the sources of systematic uncertainty in this experiment.

5.3.1 Elastic Normalization

Using the same beam, target, charged particle detectors, and electronics as the main breakup experiment, nd elastic scattering measurements were taken as well. The purpose of these measurements was to determine the product of the beam-target luminosity, charged particle detector solid angle, and DAQ fractional live time shown in Equation 5.4. In these measurements, the recoil deuteron was detected and its ToF between the ΔE and E detectors determined. The elastic deuterons had to exit the target and traverse the ΔE detector with its aluminum foil tent. During this process, there was substantial energy loss and straggling; many of the deuterons were stopped or scattered, preventing their detection. The elastic scattering measurements were modeled using the Monte-Carlo (MC) simulation described in Section 4.3 to reproduce the shape of the measured ToF spectrum accurately. The simulation was run until statistical uncertainty was negligible; a $\pm 1\%$ error was assigned to the simulated spectrum resulting from cross-section weighting [Wit89]. The results of this simulation are shown in Figure 5.9. The simulation was used to estimate the total number of nd elastic events that occured over the course of the experiment, as shown in Equation 5.5.

The measured ToF spectrum for elastic deuterons was produced using the PID techniques described in Section 5.2.1. This spectrum is shown in Figure 5.10 which is a projection of the contents of the blue deuteron PID gate shown in Figure 5.2 onto the ToF axis. This gate was also shifted to an unphysical region of the ToF spectrum containing only accidental counts in order to apply a background subtraction to the elastic spectrum.

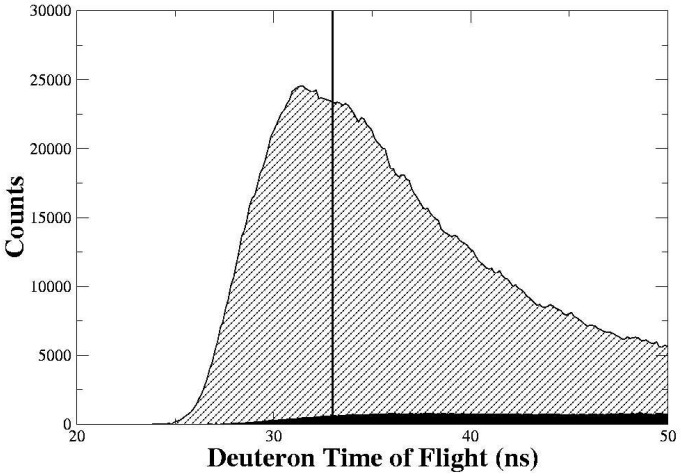

Figure 5.9: Monte-Carlo simulation of the elastic deuteron ToF spectrum. Only the region of the spectrum to the left of the vertical line was used in the normalization. The region shaded black indicates the influence of the SBU neutrons.

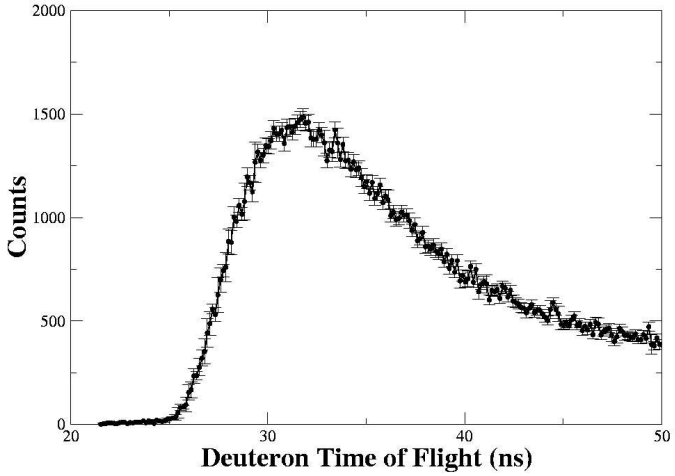

Figure 5.10: Measured elastic deuteron ToF spectrum. This is a projection of the contents of the blue deuteron PID gate shown in Figure 5.2 onto the ToF axis. The error bars represent statistical uncertainty.

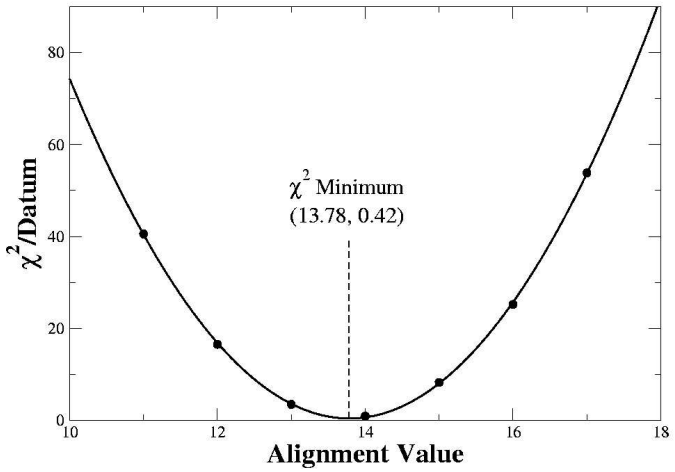

Figure 5.11: Elastic scattering χ^2 minimization. The alignment value represents which entry in the measured elastic scattering spectrum corresponded to the first entry in the pruned Monte-Carlo spectrum for that particular linear fit.

The ToF spectum created by the Monte-Carlo simulation was fit to the measured data taken by each charged particle arm on a batch-by-batch basis. The MC spectrum was binned such that the width of one bin corresponded to the width of one TDC channel (0.135 ns). This spectrum was then pruned to include only the highest energy elastic deuterons; only the part of the spectrum to the left of the vertical line in Figure 5.9 was used for this fit. This was done to minimize the effect of the SBU part of the neutron beam as well as any discrepancies in the background subtraction on the analysis. A linear fit was performed between the channel yields in the two spectra, given as follows:

$$Y_i^{meas} = mY_j^{MC} + b. \tag{5.7}$$

The pruning of the MC spectra determined the number of points to fit. The fit parameter, b, was included to account for any errors in the background subtraction. To allow for errors in timing calibration, the pruned MC spectrum was scanned across the measured spectrum with a linear fit being performed at each increment. The difference between the j^{th} bin of the MC and the i^{th} bin of the measured spectrum $(i - j)$ will be referred to as the "alignment value" for that linear fit. For each alignment value, a χ^2/datum was calculated as well as a background subtracted measured yield ($Y^{BS} = mY^{MC}$). These were each plotted and fit to parabolic functions as shown in Figures 5.11 and 5.12. The alignment value of the minimum

reduced χ^2 (13.78 in Figure 5.11) was used to determine the optimal measured yield. The error in this yield was estimated by adding one to the minimum value of χ^2/datum and finding the corresponding range of yields. The combination of this "high energy" measured yield, the integration of the cross-section weighted pruned MC spectrum, and the total number of elastic events simulated by the MC were then used to estimate the total number of *nd* elastic events resulting from the 16.0 MeV "prompt" neutron beam that occurred during the course of a data run. The results for the two charged particle arms were averaged and the disagreement between the two sides was used as a measure of the $\pm 4\%$ systematic uncertainty.

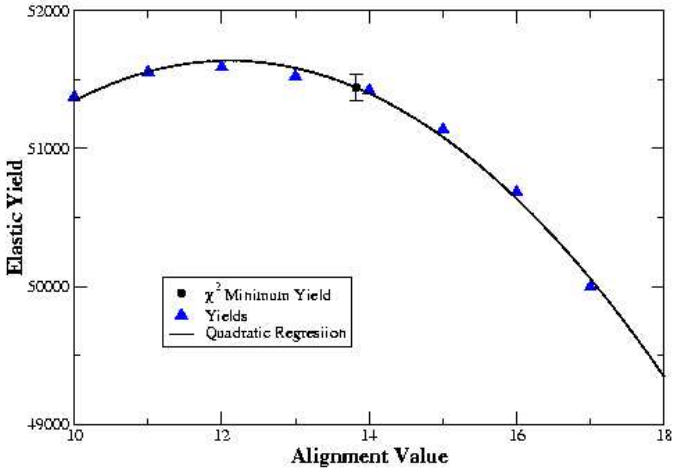

Figure 5.12: Determination of the *nd* elastic scattering yield from the χ^2 minimization. The optimal yield was determined from a quadratic fit of Measured Yields vs. Alignment Value. Error bars were obtained by adding one to the minimum value of χ^2/datum and determing the range of yields associated with the corresponding alignment values.

5.3.2 Neutron Detection Parameters

The explanations for two of the neutron detection parameters, Ω_n and ΔE_n, are pretty straightforward. The neutron detector solid angles, Ω_n, were determined by dividing the cross-sectional area of the scintillator volume by the square of the distance between the center of the scintillator volume and the target. The width of the neutron energy bins were set at 1 MeV as a balance between accurately tracing the shape of the cross section and statistical uncertainty.

The neutron detector efficiency, ε_n, is an energy dependent quantity. The neutron scintillators produce a light pulse when a neutron scatters on a proton in their volume that is

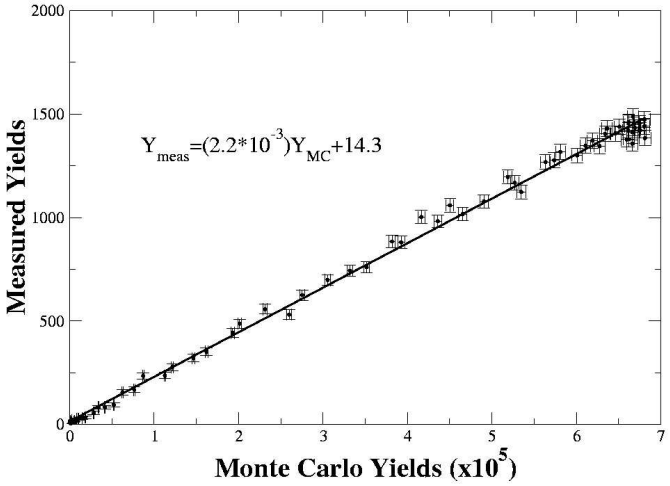

Figure 5.13: Results of the linear fit between elastic scattering data and the Monte-Carlo simulation for the best integer alignment value.

proportional to the energy delivered to the recoiling proton. This recoil energy varies continuously from the full energy of the neutron all the way down to zero since the neutron may pass through without interacting at all. A software threshhold was applied to the neutron pulse height spectrum which disregards any signals detected below a specific energy. This pulse height threshold determines the probability that a neutron of a particular energy which entered the detector would be included in the measured spectrum. Several times over the course of each accelerator run, the neutron beam would be stopped so that ^{137}Cs and ^{22}Na γ-sources could be placed near the detectors. These sources produce γ-rays at three specific energies. The Compton scattering edge for each γ-ray energy was recorded; and these were used to calibrate the neutron pulse height spectrum. The choice of pulse height threshold was based on this calibration and was specified by what fraction of the ^{137}Cs Compton edge it corresponded to. Thus this threshold is also referred to as the Cs-bias; a $\frac{1}{2}$Cs-bias was used for all detectors in this experiment. The absolute efficiencies of the neutron detectors were measured previously at TUNL using the $^2H(d,n)^3He$ reaction as well as neutrons from a ^{252}Cf spontaneous fission source. The details of these measurements may be found in the dissertations of D.E. González Trotter [Gon98] and F. Salinas [Sal98]. Tables, plots, and further information on the neutron detector efficiencies may be found in Appendix C.

The neutron attenuation factor, α_n, is the probability that an outgoing breakup neutron initially headed for a particular detector will not be scattered away from the detector by intermediate material (technically this is a transmission factor). The material between the

reaction and the neutron detectors differed between the SST and CST detectors. The CST neutrons simply had to exit the target and pass through a 25 μm tantalum foil; the attenuation was negligible ($\alpha_n = 1$). The SST neutrons had to exit the target and pass through the 0.318 cm thick aluminum dome. Using the total interaction cross section for 4.6 MeV neutrons with aluminum, we estimate that 4% of the neutrons should interact in the aluminum. Additionally, a large portion of the neutrons scattered by the aluminum were still detected on account of the large forward angle differential cross section. Some neutrons that initially would have missed the detector were scattered into the detector lessening this effect further. A first-order estimate based on an isotropic neutron distribution across the surface of the dome and isotropic, energy-independent neutron-aluminum scattering was performed which indicated that for the SST configuration $\alpha_n = 0.98 \pm 0.01$.

5.3.3 Systematic Errors

The known sources of systematic error in this experiment are as follows: (1) *nd* elastic normalization, (2) SBU subtraction, (3) neutron detector solid angle, (4) neutron detector efficiency, (5) neutron attenuation, and (6) neutron energy binning. The estimates for the relative error of each of these contributions are added in quadrature to estimate the systematic error for the entire experiment as shown in the following formula.

$$\left(\frac{\Delta Y_{bu}}{Y_{bu}}\right)_{sys} = \left[\left(\frac{\Delta Y_{el}}{Y_{el}}\right)^2 + \left(\frac{\Delta Y_{SBU}}{Y_{SBU}}\right)^2 + \left(\frac{\Delta \Omega_n}{\Omega_n}\right)^2 + \left(\frac{\Delta \varepsilon_n}{\varepsilon_n}\right)^2 + \left(\frac{\Delta \alpha_n}{\alpha_n}\right)^2 + \left(\frac{\Delta E_n}{E_n}\right)^2\right]^{\frac{1}{2}} \tag{5.8}$$

Estimates of the magnitude of each term in Equation 5.8 and the sources of these systematic uncertainties are described below and summarized in Table 5.3.

1. The uncertainty in the *nd* elastic normalization arises from several sources. Background subtraction, calculation of deuteron energy loss, angular uncertainties, fitting errors, and cross-section weighting must contribute. The magnitude of this uncertainty was estimated by examining the difference between the neutron flux determined by the two charged particle detectors as described in Section 5.3.1. This uncertainty was estimated to be $\pm 4.0\%$.

2. The subtraction of SBU induced *nd* breakup events is described in Section 5.2.3. The uncertainty in this quantity was governed by the uncertainty in the *nd* breakup cross sections and neutron beam energy spectrum used to model the SBU events in the Monte-Carlo simulation. These quantities were varied within reasonable bounds and the range of results were used to estimate the $\pm 1.0\%$ uncertainty assigned to this quantity.

3. The uncertainty in the neutron detector solid angle is derived from the the measurement error in the neutron flight paths ($\pm 2mm$) and scintillator radii ($\pm 0.5mm$). Since the

SST and CST flight paths were different, their relative uncertainties are slightly different, ±1.7% and ±1.6% respectively. However, after performing the error propagation described by Equation 5.8, the difference between the overall systematic uncertainties between the two configurations is negligible.

4. Neutron detector efficiencies were obtained through previous measurements at TUNL of the $^2H(d,n)^3He$ source reaction as well as the spontaneous fission of a ^{252}Cf source [Sal98, Gon98]. These measurements were compared to a simulated spectrum. The uncertainty in these efficiencies was derived from two sources: a ± 3% uncertainty stemming from the range of normalizations needed to bring the measured spectra in agreement with the simulation for the various detectors and a ± 1% uncertainty associated with small deviations in the shape of the measured spectra. These uncertainties were added in quadrature to produce an overall systematic error of ± 3.2%

5. The ±1.0% systematic uncertainty assigned to the neutron attentuation coefficient in the SST configuration was based upon a first-order estimate of isotropic, energy-independent neutron-aluminum scattering. The maximum and minimum possible values for this coefficient differed only by ±2%. The effects of neutron attenuation on the CST configuration were negligible, thus no uncertainty was alotted.

6. The width of the neutron energy bins into which the measured counts are projected is determined by the energy calibration. Uncertainty in the measurement of the nanoseconds per TDC channel used in this experiment provide us with a conservative estimate of ± 1% systematic error in the width of the 1 MeV energy binning.

Source of Uncertainty	Estimated Uncertainty
Elastic Normalization	±4.0%
SBU Subtraction	±1.0%
Solid Angle	±1.7%
Detector Efficiency	±3.2%
Neutron Attenuation (SST)	±1.0%
Neutron Attenuation (CST)	±0.0%
Energy Binning	±1.0%
Total Uncertainty (SST)	±5.7%
Total Uncertainty (CST)	±5.6%

Table 5.3: Summary of systematic uncertainties inherent in the breakup cross-section measurement.

6 Results and Conclusions

This chapter will summarize the experimental results for the nd breakup cross-section measurements of the SST and CST configurations and compare them to theoretical predictions as well as to previous measurements. A series of studies probing the sensitivity of the theoretical calculations to modifications of the nuclear potential were performed. The first of these tested the different NN potential models and 3NF's described in Section 2.2. The second tested the sensitivity of the calculations to the partial waves included in the CD-Bonn potential. The final study examines the effects of modifying the nn $^1S_0$ component of the CD-Bonn potential. The chapter will conclude with speculations as to how theoretical predictions may be brought into agreement with experimental findings based upon the results of these sensitivity studies.

6.1 Space-Star Results

The results for the SST cross-section measurements are shown in Figure 6.1. The counts measured in 1 MeV bins along the neutron energy axis after subtracting background events are shown for the two mirrored detector pairs, N1-E2 and N2-E1, as well as their statistically weighted average. The error bars on these measurements reflect only statistical uncertainty. The solid black line in the figure is the theoretical prediction produced by the Monte-Carlo simulation based on the CD-Bonn [Mac01a] potential; the blue band around it shows the $\pm 5.8\%$ systematic uncertianty. The discrepancy between the theoretical cross-section prediction and the actual value should be directly proportional to the relative difference between the measured and predicted counts. The SCRE condition occurs at a detected neutron energy of 4.6 MeV and is indicated in the figure by the vertical dashed line. Considering the weighted average of the two detector pairs, the theoretical prediction is $\sim 28\%$ below the measurement around the SCRE condition.

All previous measurements of the SST reported the differential cross section with respect

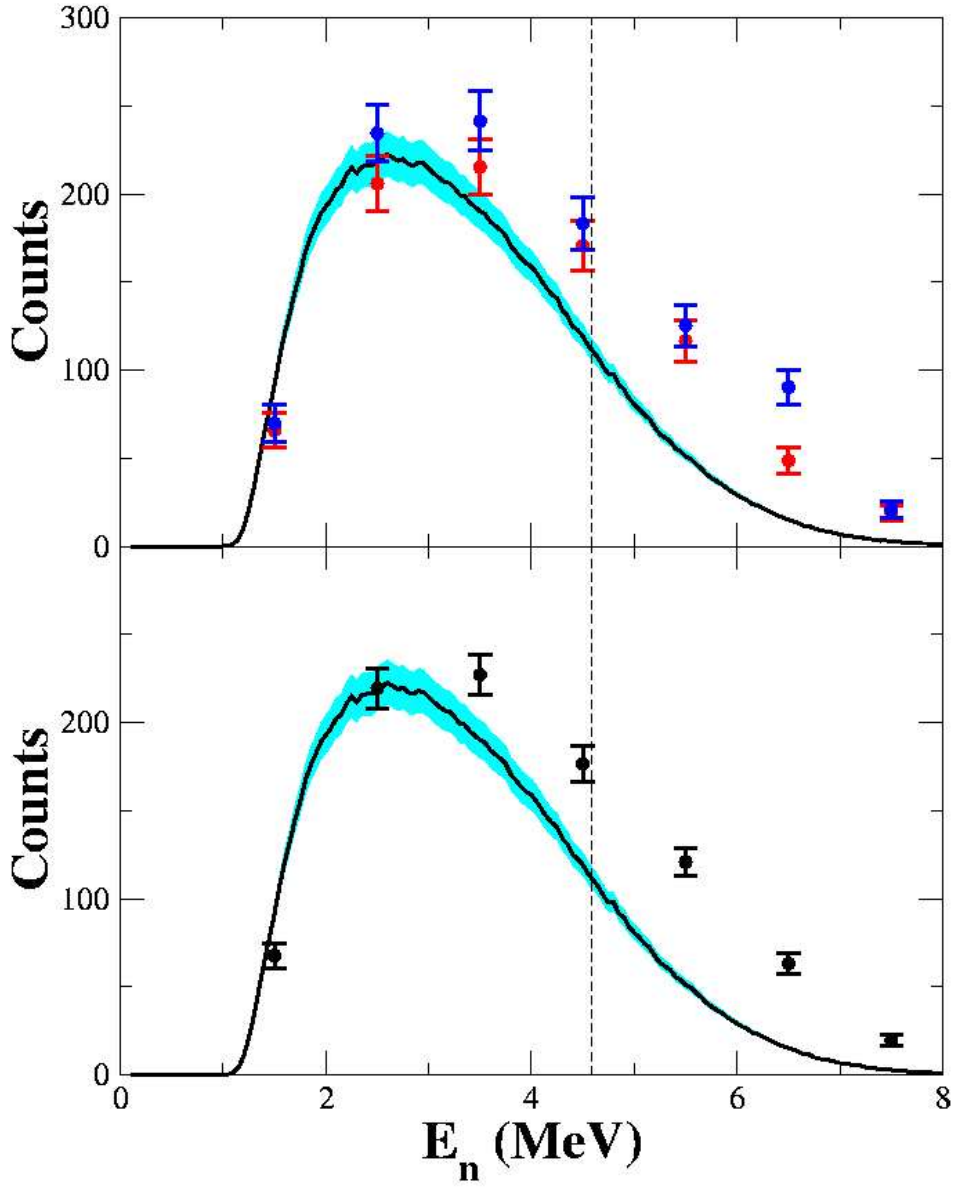

Figure 6.1: Results for the SST measurement. The top graph shows the counts measured by the N1-E2 (blue points) and N2-E1 (red points) detector pairs after background subtraction. The bottom graph shows the weighted average of the two sides (black points). Error bars on data points represent statistical uncertainties only. The solid black line represents the theoretical prediction obtained from the Monte-Carlo simulation and the band around it represents the 5.7% systematic uncertainty. The vertical dashed line indicates the neutron energy of the SCRE condition.

to S, $d^5\sigma/d\Omega_1 d\Omega_2 dS$. The current results must be presented in the same manner to compare them with those measurements. To do this, the relative discrepancy between data and theory found at the SST condition was multiplied by the point geometry cross section based on the CD-Bonn potential to obtain a value of 1.203±0.098 mb/sr^2·MeV. Figure 6.2 shows this value compared with the history of *nd* breakup five-fold differential cross-section measurements.

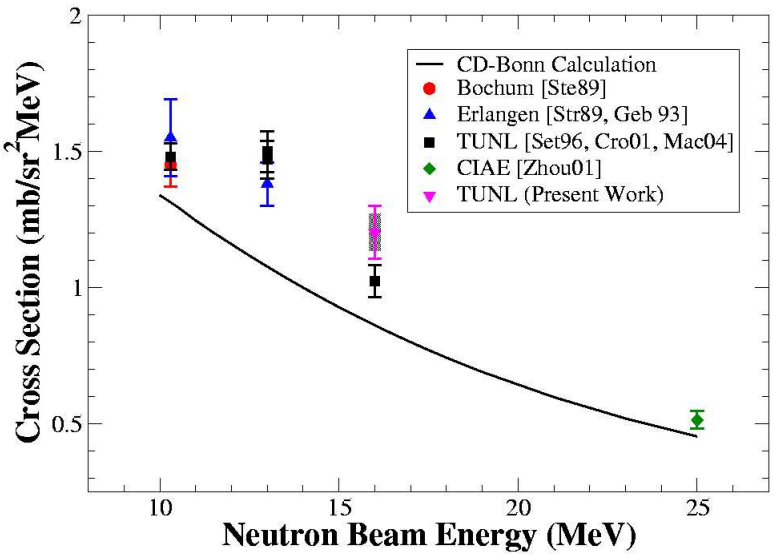

Figure 6.2: History of SST cross-section measurements with the present datum included. The data point for the present work shown as the magenta triangle was created by calculating the relative discrepancy between the number of counts measured and the number of counts predicted by the CD-Bonn potential. This discrepancy was then used to estimate the point geometry cross section by simple multiplication. The statistical error on the data point for the present work is shown by the black shaded band. The magenta error bar for this point is the statistical and systematic errors added in quadrature. While adding statistical and systematic errors in quadrature can not be rigorously justified, it gives the reader a feel for the magnitude of the total uncertainty [Tay97].

6.2 Coplanar-Star Results

The results for the CST cross-section measurements are shown in Figure 6.3. In the same manner as the SST results, the counts measured in 1 MeV bins along the neutron energy axis after subtracting background events are shown for the two mirrored detector pairs, N3-E2 and N4-E1, as well as their weighted average. The error bars on these measurements reflect

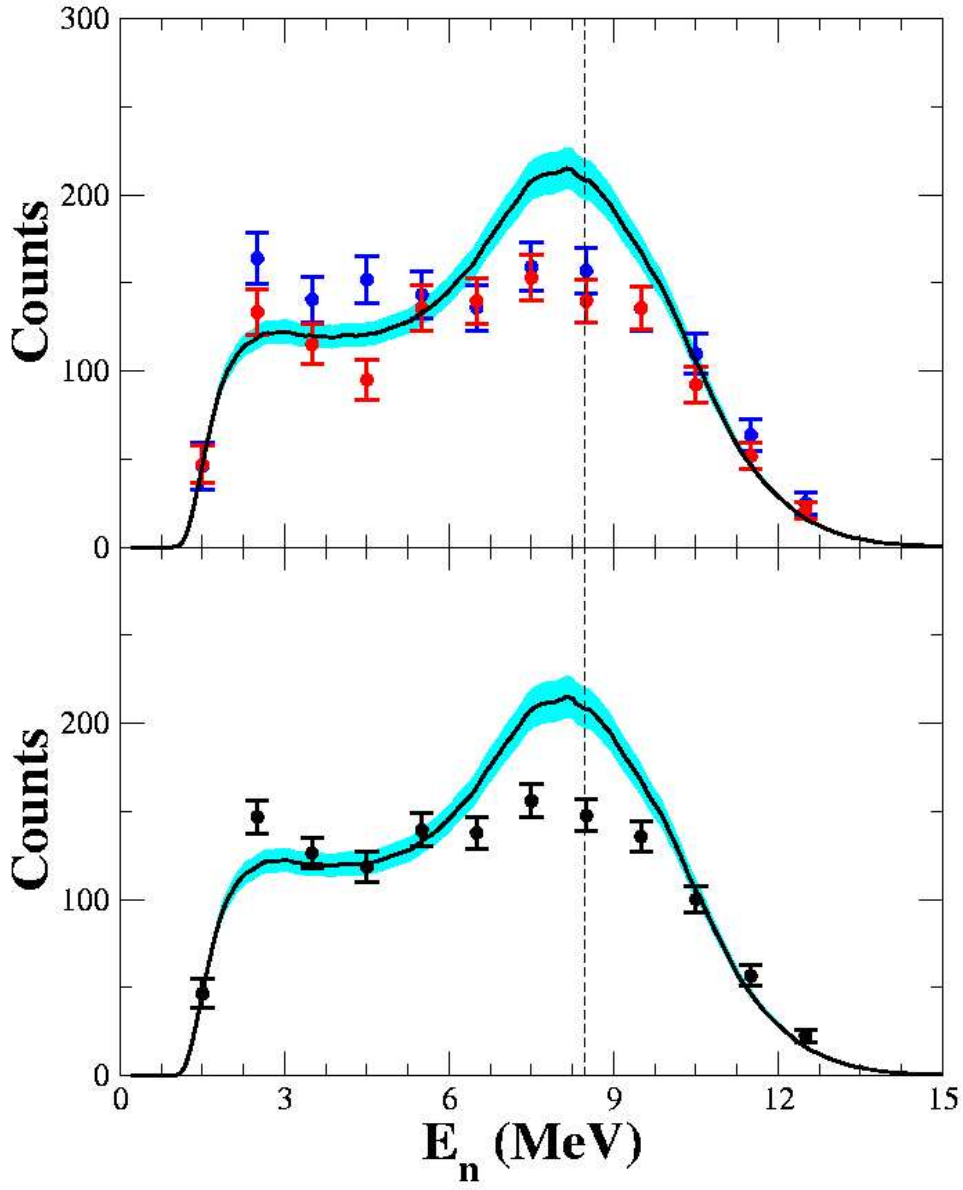

Figure 6.3: Results for the CST measurement. The top graph shows the counts measured by the N3-E2 (blue points) and N4-E1 (red points) detector pairs after background subtraction. The bottom graph shows the weighted average of the two sides (black points). Error bars on data points represent statistical uncertainties only. The solid black line represents the theoretical prediction obtained from the Monte-Carlo simulation and the band around it represents the 5.6% systematic uncertainty. The theoretical predictions for the two detector pairs varied slightly because of the slight difference in geometry. The average value is shown on the graphs; and the two values lie within the error band. The vertical dashed line indicates the neutron energy of the SCRE condition.

only statistical uncertainty. The solid black line in the figure is the theoretical prediction produced by the Monte-Carlo simulation based on the CD-Bonn [Mac01a] potential, and the blue band around it shows the ±5.6% systematic uncertainty. The SCRE condition occurs at a detected neutron energy of 8.45 MeV and is indicated in the figure by the vertical dashed line. Considering the weighted average of the two detector pairs, the theoretical prediction is $\sim 40\%$ above the measurement around the SCRE condition. This discrepancy is confined to the kinematic region near the SCRE condition in this configuration. The theory follows the data quite nicely at detected neutron energies below 6 MeV and above 10 MeV.

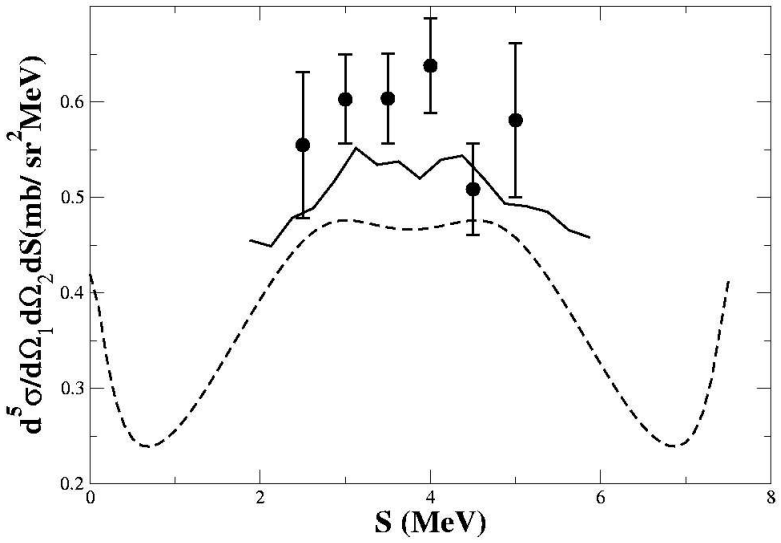

Figure 6.4: Results from the previous 16.0 MeV CST cross-section measurement of A. Crowell [Cro01]. Two neutrons were detected in coincidence at laboratory angles of $\theta_{n1} = \theta_{n2} = 71.2°$ and $\phi_{12} = 180°$. The dashed line gives the gives CD-Bonn prediction for point geometry. The solid line is the finite-geometry prediction based on Monte-Carlo simulations. The error bars represent only statistical uncertainty.

The first CST data taken were at an incident neutron energy of 13.0 MeV in an asymmetric configuration by Strate *et al.* [Str89] and were reported higher than the theoretical prediction by 10-25%. This measurement was repeated by Setze *et al.* [Set05]; and was found to be in agreement with theory. Setze indicated that the background subtraction applied in the analysis of Strate was underestimated [Set05] which would lessen the reported discrepancy, if not eliminate it entirely. Additionally symmetric CST measurements taken at beam energies of 10.3 and 13.0 MeV [Mac04] agreed with theoretical predictions within the experimental

uncertainty. In the previous 16.0 MeV CST measurement [Cro01], the results of which are shown in Figure 6.4, the data were on average 1.4 standard deviations higher than theory. Those data were taken in the symmetic CST configuration where the direction of the outgoing proton is opposite the direction of the incident neutron in the CM frame. The present data were taken in an asymmetric configuration such that the direction of the outgoing proton was perpendicular to the neutron beam in the CM frame. It is odd that a 90° rotation of the outgoing particles would produce cross-section discrepancies of opposite signs and significantly different magnitudes when compared to theoretical predictions.

6.3 Sensitivity Studies

All the theoretical predictions shown in the previous section were based upon the CD Bonn nucleon-nucleon (NN) potential model [Mac01a]. Since there is significant disagreement between these predictions and the present results, an investigation into possible resolutions of this disagreement must ensue. There are other possible NN potential models which may prove a better match to experimental findings. Also the effects of three-nucleon forces (3NF) need to be considered. It also would be instructive to test the sensitivity of the SST and CST breakup cross sections to the contributions of the various partial waves used in Faddeev calculations. The likely culprits for the source of the discrepancy may then be identified and tested.

6.3.1 Sensitivity to Potential Models

In order to test the dependence of theoretical predictions to the underlying dynamics contained in traditional meson-exchange based potential models, 3N Faddeev calculations were performed using different modern NN potentials alone and combined with 3NF models [Glö96, Hüb97]. Along with the CD Bonn potential [Mac01a], the AV18 [Wir95] and Nijmegen I and II [Sto94] high precision NN potentials were also used to make predictions. These four NN potential models were each combined with the TM99 3NF [Coo81, Coo01] using cutoff Λ values which led to a reproduction of the ^{3}H binding energy for a particular NN force and TM99 combination. The AV18 NN potential was also combined with the UIX 3NF [Pud97] which was developed for exclusive use with this potential. All NN potentials used provided virtually the same cross-section predictions. The effects of the TM99 and UIX 3NF models were also essentially negligible.

Faddeev calculations were also performed using potential models derived from the framework of chiral effective field theory (χEFT). Ten different NN chiral potentials were used, five at N^{2}LO and five at N^{3}LO [Epe06]. These potentials differ in the value of the high-momentum cutoffs used in their derivation. Using a particular pair of cutoffs, Λ and $\tilde{\Lambda}$, their low-energy

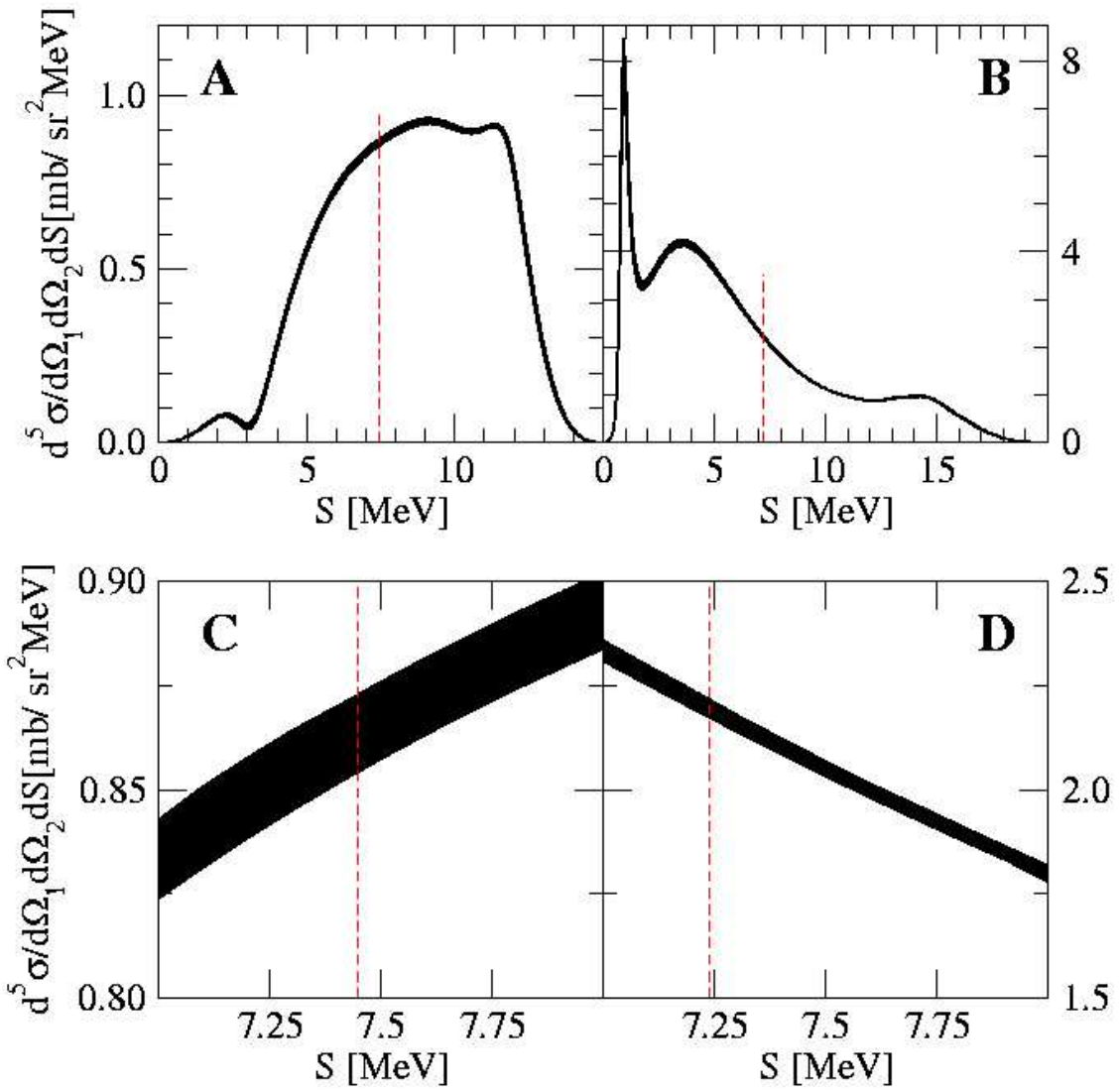

Figure 6.5: Sensitivity of the five-fold point geometry cross section, $d^5\sigma/d\Omega_p d\Omega_n dS$, to different potential models as a function of the S-curve length. Faddeev calculations using 24 different potential models, including traditional meson-exchange and χEFT potentials both with and without 3NF's, were performed for the SST (A) and CST (B) configurations. All results lie within the black bands and differ by less than 2% at the location of the star condition. The red dashed lines indicate the location of the star condition. Graphs C and D are zoomed in views of the SCRE condition for graphs A and B, respectively.

constants were then adjusted to reproduce two-nucleon phase shifts. All choices of these cutoff values described the two-nucleon system equally well. The first non-vanishing 3NF appears in N^{2}LO order of the chiral expansion with three contributing topologies: the 2π-exchange between three nucleons, a one-pion exchange between one nucleon and two-nucleons interacting pointwise, and a pure 3N contact interaction. While standard 3NF models only take into account 2π-exchange, these topologies simulate contributions from heavier meson-exchanges such as π–ρ and ρ–ρ in their contact terms. Each of the five N^{2}LO potentials were combined with a chiral 3NF using the same high-momentum cutoffs. Two additional adjustable parameters appear in the short-range 3NF terms which were adjusted for each potential to reproduce the triton binding energy and the *nd* scattering length [Epe02]. At N^{3}LO, 3NF contributions have been derived [Ber08], but have yet to be transcribed into a form applicable to numerical Faddeev calculations. The star cross sections were found to be practically insensitive to variations in the χEFT potential model used. For both configurations studied, all theoretical cross-section predictions based on both traditional meson-exchange models and χEFT, with and without 3NF's differed at most by 2% at the star condition as shown in Figure 6.5.

6.3.2 Sensitivity to Partial Waves

Since the star cross sections are practically insensitive to the choice of potential model used to produce theoretical predictions, the CD Bonn model was given further examination. At low energies, the largest contributions to these cross sections should be provided by the S-wave components of the NN potential. Faddeev calculations were performed using the $^1S_0$, $^3S_1$-$^3D_1$, the combination of these two, and all higher angular momentum components of the CD Bonn interaction up to a two-body total angular momentum, $j = 3$. The results of these calculations are shown in Figure 6.6 for the SST and CST configurations. These studies show that the star cross sections are built predominantly from the singlet and triplet S-wave components of the NN force with the triplet being the dominant of the two. The effects of higher order partial waves on the star cross sections are essentially negligible. Both the $^1S_0$ and $^3S_1$-$^3D_1$ *np* forces have been well determined by *np* scattering data and the properties of the deuteron [Sto93]. Up to this point, the $^1S_0$ *nn* force has only been determined indirectly because of the lack of free *nn* data [Kon10, Gar09]. Therefore, the $^1S_0$ *nn* force is the most likely culprit for the disagreement between data and theory in the star configurations.

6.3.3 Sensitivity to the nn $^1S_0$ Component

There is further evidence of possible issues with the nn $^1S_0$ component of the nucleon-nucleon interaction which have arisen from cross-section measurements of the quasifree scattering (QFS) configuration of *nd* breakup. The QFS configuration refers to a situation in which one of the nucleons is at rest in the laboratory system. In *nd* breakup, the *nn* or *np*

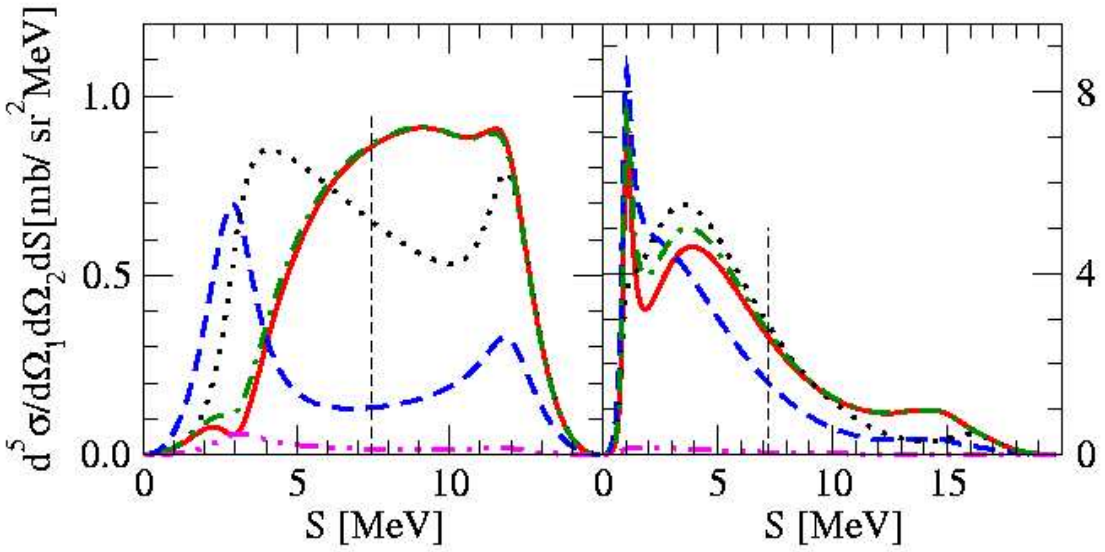

Figure 6.6: Sensitivity of the five-fold point geometry cross section, $d^5\sigma/d\Omega_1 d\Omega_2 dS$, to the CD Bonn potential to different partial waves for the SST (left) and CST (right) configurations as a function of the S-curve length. The solid (red) line shows the full calculation with all partial waves up to $j_{max} = 3$ included. The dashed (blue), dotted (black), and dashed-dotted (green) lines show the results when only contributions from $^1S_0$, $^3S_1$-$^3D_1$, and $^1S_0$+$^3S_1$-$^3D_1$ are kept when calculating the cross sections, respectively. The dashed-double-dotted (magenta) line presents contribution of all partial waves with the exception of $^1S_0$ and $^3S_1$-$^3D_1$. The position of the SCRE condition is indicated by the vertical dashed line.

QFS configurations are possible, leaving the proton or one of the neutrons at rest, respectively. Measurements of QFS cross sections have been performed at incident neutron energies of 26 MeV [Sie02] and 25 MeV [Rua07]. At 26 MeV both nn and np QFS configurations were measured; while at 25 MeV only nn was measured. The results for nn QFS resemble those of the SST: the nn QFS cross sections are clearly underestimated by $\approx 20\%$. Suprisingly, when the np pair is quasi-freely scattered instead, the theory closely follows the np QFS cross-section data [Sie02].

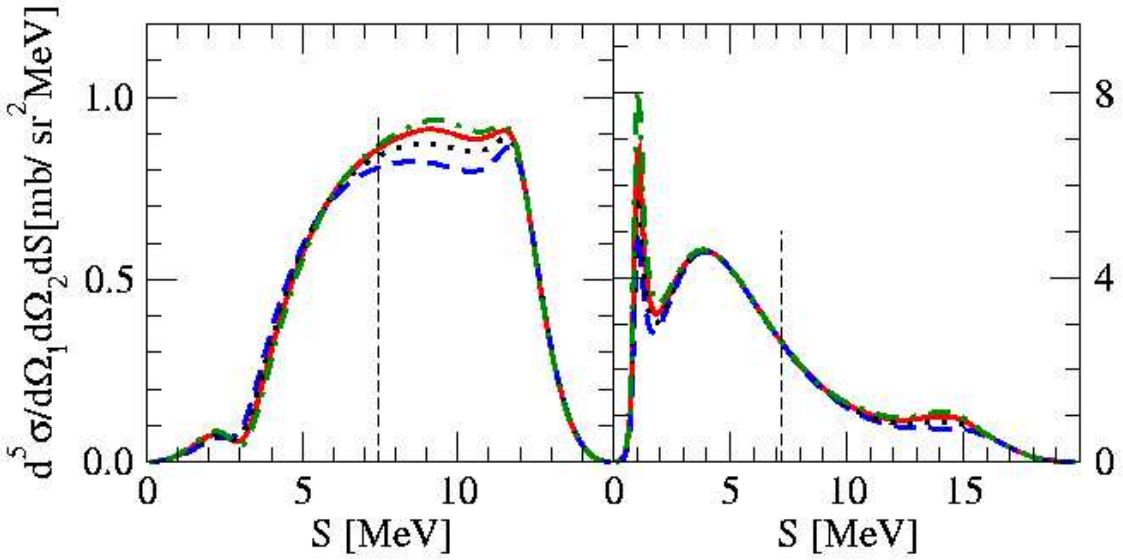

Figure 6.7: Sensitivity of the star five-fold point geometry cross sections, $d^5\sigma/d\Omega_1 d\Omega_2 dS$, in the SST (left) and CST (right) configurations to the changes of the nn $^1S_0$ force component as a function of S-curve length. Those changes were induced by multiplying the $^1S_0$ nn matrix element of the CD Bonn potential by a factor λ. The solid (red) line is the full result based on the original CD Bonn potential [Mac01a] and all partial waves with 2N total angular momenta up to $j_{max} = 3$ included. The dashed (blue), dotted (black), and dashed-dotted (green) lines correspond to $\lambda = 0.9$, 0.95, and 1.05, respectively. The vertical dashed line indicates the position of the SCRE condition.

Sensitivity studies analogous to those described in the previous two sections have been performed for these QFS configurations [Wit10b] which show that these cross sections are highly independent of the NN potential and practically do not change when any of the present day 3NF's are included. The partial wave analysis study proved that QFS is dominated by S-wave contributions as well. Studies to probe the sensitivity of QFS, SST, and CST cross sections to the $^1S_0$ nn force component have been performed. In these studies, a very simple mechanism was used to change the $^1S_0$ nn interaction; the $^1S_0$ nn matrix element of the CD Bonn poten-

tial was multiplied by a factor λ. This technique demonstrated that the nn QFS undergoes significant variations while the np QFS cross sections remain essentially unchanged as shown in Figure 6.8. The increase in the $^1S_0$ nn force strength ($\lambda = 1.08$) needed to bring the nn QFS theoretical cross sections into agreement with data would lead to a nearly bound state of two neutrons [Wit10b]. The corresponding study for the SST configuration has shown that changes which would provide an explanation for the nn QFS have almost no effect on the SST discrepancy. In Fig. 6.7, we present evidence that changing the $^1S_0$ nn interaction does not influence the CST configuration and has only a minor effect on the SST cross section near the star condition. The study was performed with λ values of 0.9, 0.95, and 1.05. Increasing the value of λ much beyond 1.05 would require modification to the Faddeev calculations to take into account the neutron-neutron bound state. This is feasible; however, further experimental evidence for this state will be required for such modifications to be warranted.

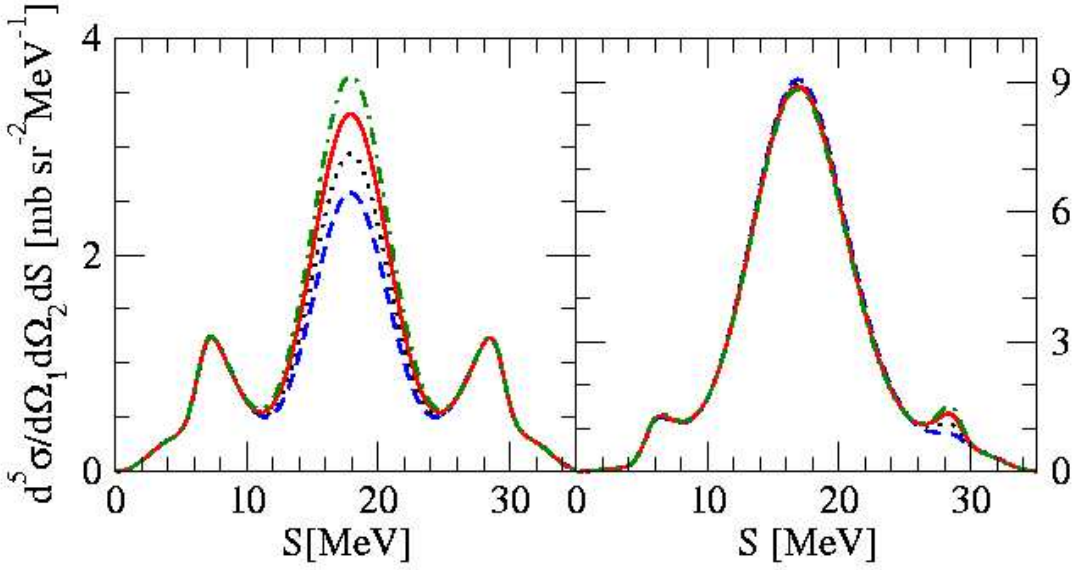

Figure 6.8: Sensitivity of the nn (left) and np (right) QFS five-fold point geometry cross sections, $d^5\sigma/d\Omega_1 d\Omega_2 dS$, at an incident neutron energy of 26 MeV to changes in the nn $^1S_0$ force component as a function of S-curve length. There are significant variations in nn QFS, while np QFS remains virtually unchanged. For a description of the lines see Figure 6.7, the only difference being at this higher energy all partial waves with 2N total angular momenta up to $j_{max} = 5$ were included.

6.4 Discussion and Speculations

The results of this experiment confirm the SST anomaly in *nd* breakup established by previous measurements which measured differential cross section by detecting the two outgoing neutrons in coincidence. The present measurement used a different experimental technique which detected the proton and one of the neutrons in coincidence and found a similar discrepancy with theoretical calculations. Additionally, the CST measurement found discrepancies between data and theory in a kinematic region of the 3N continuum unexplored by previous experiments. Preliminary analysis of 19.0 MeV *nd* breakup data taken at TUNL indicates similar discrepancies with the SST and CST cross sections [Taj10] providing further credence to these claims.

The sensitivity study presented in Section 6.3.1 clearly shows that cross-section calculations using the most advanced nuclear potential models currently available all provide essentially the same prediction for the *nd* breakup configurations measured in this experiment. However, this does not exclude the possibility that some exotic, long-range components of a 3NF could provide the modification to the nuclear potential needed to bring theoretical calculation in line with data. Chiral perturbation theory in orders higher than N^{2}LO introduces a multitude of additional short- and long-range 3NF contributions which come with a variety of momentum-spin dependencies [Ber08]. While fourth-order corrections to a perturbative expansion which describes most processes well at third-order must by definition be small, these configurations could be particularly sensitive to the matrix elements altered by them.

Considering the large *nn* QFS discrepancies, one may indulge in even wilder speculation about the existence of a weak two neutron bound state which could affect star cross sections. Such a state would not only drastically change the $^1S_0$ *nn* interaction, but could also provide a continuous background from the following reaction:

$$\mathrm{n} + {}^2\mathrm{H} \rightarrow \mathrm{p} + {}^2\mathrm{n} \rightarrow \mathrm{p} + \mathrm{n} + \mathrm{n} \tag{6.1}$$

which would be particularly important in regions of the breakup phase-space with small cross sections, like the SST configuration [Wit10a]. The strength of the *nn* interaction is typically parameterized by the $^1S_0$ *nn* scattering length, a_{nn}, the magnitude of which is negative in unbound attractive interactions and positive for bound systems. Please refer to Appendix D for information on scattering length. Measurements of this parameter have been made through cross-section measurements of several different reactions: $^2H(n,np)n$ [Huh00a, Huh00b] giving $a_{nn} = -16.1 \pm 0.4$ fm, $^2H(n,nnp)$ [Gon98] giving $a_{nn} = 18.7 \pm 0.7$ fm, and $^2H(\pi^-,n\gamma)n$ [How98] which gave $a_{nn} = -18.5 \pm 0.5$ fm. These values were obtained by incorporating different values of a_{nn} into theoretical calculations which were then fit to the

cross-section data. However, these calculations were only sensitive to the square of the scattering length, not the sign, and did not include any accommodations for a nn bound state. The discrepancy between the $^2H(n,np)n$ a_{nn} measurement and the other two could be accounted for by such a state. An experiment that could test the nn bound state hypothesis is the photodisintegration of ^{3}H, measuring the energy spectrum of the recoil proton [Wit10b]. The energy spectrum of the proton should show two distinct regions (provided sufficient energy resolution): a low energy region pertaining to the three-body exit channel and a higher energy region of the two-body exit channel. These two regions should be separated by the binding energy of the nn state. An example of this principle is shown in Figure 6.9 which shows the summed charged particle energy spectrum of the two-body (p+d) and three-body (p+p+n) exit channels for the photodisintegration of ^{3}He.

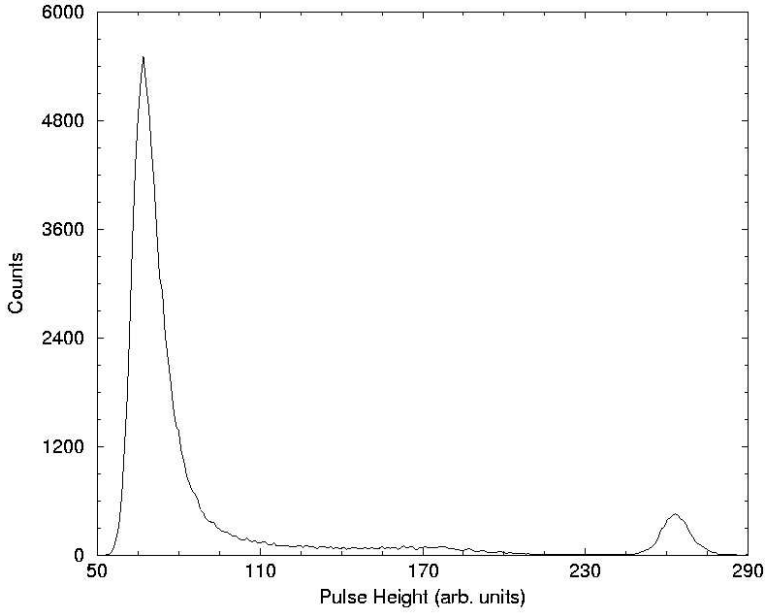

Figure 6.9: Energy spectrum obtained from the photodisintegration of ^{3}He at E_γ = 15.01 MeV. A high-pressure ^{3}He gas scintillator acted as both target and detector. The large peak on the left is from Compton scattered electrons. The three-body exit channel, $^3He(\gamma,pp)n$ is seen in the continuum of counts which extend out to a pulse height of around 215. The peak on the right is the two-body exit channel, $^3He(\gamma,pd)$. The separation between the three-body continuum and the two-body peak is defined by the deuteron binding energy [Est04].

In summary, we have presented cross sections in two kinematically complete geometries of the $E_n^{lab} = 16$ MeV nd breakup. These data have been taken by detecting the outgoing np pair in coincidence while all previous nd breakup measurements have detected the nn pair. Thus the clear discrepancy between data and theory found in the present measurement supports

those revealed in previously reported experiments. As a result of the strong stability of the theoretical cross sections to the underlying dynamics, such large discrepancies would require new long-ranged components of 3NF's or could even indicate a deficiency in our present knowledge of the $^1S_0$ nn force.

Appendices

A Tables of Experimental Results

The following tables present the counts measured during the experiment with uncertainties as well as the theoretical predictions for those counts from the Monte-Carlo simulation. These tables correspond to the plots shown in Figures 6.1 and 6.3. The counts are presented in 1 MeV bins along the neutron energy axis where the neutron energy value specified defines the center of the bin. A background subtraction has been applied to the counts. The total uncertainty was obtained by adding the statistical and systematic uncertainties in quadrature. Combining statistical and systematic uncertainties by this method can not be rigorously justified, however it may give the reader a feel for the magnitude of the total uncertainty of these measurements [Tay97]. The systematic uncertainty was 5.8%(5.6%) for the SST(CST).

Neutron Energy (MeV)	Measured Counts	Statistical Uncertainty (%)	Total Uncertainty (%)	Predicted Counts
1.5	66	15.0	16.1	91
2.5	206	7.5	9.5	221
3.5	215	7.2	9.2	194
4.5	171	8.1	9.9	121
5.5	116	9.8	11.4	52
6.5	49	15.0	16.1	16
7.5	19	23.1	23.8	3

Table A.1: Experimental results and theoretical predictions for the N1-E2 detector pair.

Neutron Energy (MeV)	Measured Counts	Statistical Uncertainty (%)	Total Uncertainty (%)	Predicted Counts
1.5	70	15.0	16.1	93
2.5	234	6.9	9.0	223
3.5	241	7.0	9.1	194
4.5	183	8.0	9.9	122
5.5	125	9.3	11.0	52
6.5	90	11.0	12.5	15
7.5	21	23.0	23.7	3

Table A.2: Experimental results and theoretical predictions for the N2-E1 detector pair.

Neutron Energy (MeV)	Measured Counts	Statistical Uncertainty (%)	Total Uncertainty (%)	Predicted Counts
1.5	46	28.9	29.4	47
2.5	164	8.8	10.4	120
3.5	141	9.2	10.8	121
4.5	152	8.7	10.4	120
5.5	143	9.4	11.0	130
6.5	136	9.7	11.2	157
7.5	159	8.7	10.3	198
8.5	157	8.5	10.2	201
9.5	136	9.3	10.9	166
10.5	110	10.4	11.8	109
11.5	64	14.1	15.2	51
12.5	25	24.4	25.1	19

Table A.3: Experimental results and theoretical predictions for the N3-E2 detector pair.

Neutron Energy (MeV)	Measured Counts	Statistical Uncertainty (%)	Total Uncertainty (%)	Predicted Counts
1.5	47	22.7	23.4	47
2.5	133	9.6	11.1	118
3.5	115	10.0	11.4	118
4.5	95	11.8	13.0	121
5.5	136	9.6	11.1	136
6.5	140	9.2	10.8	170
7.5	153	8.6	10.2	217
8.5	140	8.8	10.4	214
9.5	136	9.0	10.6	169
10.5	92	11.2	12.5	102
11.5	52	14.8	15.8	42
12.5	21	22.9	23.6	13

Table A.4: Experimental results and theoretical predictions for the N4-E1 detector pair.

Neutron Energy (MeV)	Measured Counts	Statistical Uncertainty (%)	Total Uncertainty (%)	Predicted Counts
1.5	68	10.6	12.1	96
2.5	219	5.1	7.7	231
3.5	227	5.0	7.7	201
4.5	176	5.7	8.1	126
5.5	121	6.8	8.9	54
6.5	63	9.3	11.0	16
7.5	20	16.3	17.3	3

Table A.5: Experimental results and theoretical predictions for the SST configuration. These are the weighted averages of the N1-E2 and N2-E1 detector pairs.

Neutron Energy (MeV)	Measured Counts	Statistical Uncertainty (%)	Total Uncertainty (%)	Predicted Counts
1.5	46	17.9	18.7	47
2.5	147	6.5	8.6	119
3.5	126	6.8	8.8	120
4.5	118	7.2	9.1	121
5.5	139	6.7	8.7	133
6.5	138	6.7	8.7	164
7.5	156	6.1	8.3	208
8.5	148	6.1	8.3	208
9.5	136	6.5	8.6	167
10.5	100	7.7	9.5	105
11.5	57	10.2	11.7	47
12.5	22	16.8	17.7	16

Table A.6: Experimental results and theoretical predictions for the CST configuration. These are the weighted averages of the N3-E2 and N4-E1 detector pairs.

B Kinematic Tables

These tables present kinematic quantities of interest pertaining to nd breakup at 16.0 MeV for the central angles of the four detector pairs used in this experiment. The central detector angles are specified in the caption below each table. The quantities given in the tables are defined as follows:

- E_p = laboratory energy of the proton,
- E_n = laboratory energy of the detected neutron,
- E_u = laboratory energy of the undetected neutron,
- E_{pn} = relative energy between the proton and the detected neutron,
- E_{pu} = relative energy between the proton and the undetected neutron,
- E_{nu} = relative energy between the two neutrons,
- θ_u = laboratory polar scattering angle of the undetected neutron,
- ϕ_u = laboratory azimuthal scattering angle of the undetected neutron, and
- S = the length along the S-curve.

The SCRE condition occurs when all three particles have the same relative momentum. If the detectors were set up at the ideal angles, the SST would occur at S=7.45 MeV and the CST would occur at S=7.24 MeV. For the SST, the ideal angles would have been $\theta_n = \theta_p = 51.52°$ and $\phi_{np} = 120°$. For the CST, these angles would have been $\theta_n = 16.75$, $\theta_p = 51.52°$, and $\phi_{np} = 180°$.

N1-E2 Space-Star Kinematics								
Laboratory Energy (MeV)			Relative Energy (MeV)			Undet. Neutron Lab Angle (°)		S (MeV)
E_p	E_n	E_u	E_{pn}	E_{pu}	E_{nu}	θ_u	ϕ_u	S
1.00	6.49	6.28	3.55	2.39	6.72	44.1	276.2	3.2
1.20	6.52	6.05	3.64	2.36	6.65	45.1	273.8	3.4
1.40	6.52	5.86	3.73	2.37	6.57	45.9	271.5	3.6
1.60	6.49	5.69	3.79	2.40	6.47	46.6	270.7	3.8
1.80	6.43	5.54	3.85	2.45	6.35	47.2	272.8	4.0
2.00	6.36	5.41	3.91	2.52	6.23	47.8	274.9	4.2
2.20	6.28	5.29	3.95	2.61	6.10	48.3	277.0	4.5
2.40	6.18	5.19	3.99	2.70	5.96	48.8	279.0	4.7
2.60	6.07	5.10	4.03	2.81	5.82	49.2	281.0	4.9
2.80	5.95	5.02	4.06	2.93	5.67	49.5	283.1	5.1
3.00	5.82	4.96	4.09	3.06	5.51	49.8	285.1	5.4
3.20	5.68	4.90	4.11	3.20	5.35	50.1	287.1	5.6
3.40	5.53	4.85	4.13	3.35	5.18	50.3	289.1	5.9
3.60	5.37	4.80	4.15	3.50	5.01	50.5	291.1	6.1
3.80	5.20	4.77	4.16	3.66	4.84	50.6	293.2	6.4
4.00	5.03	4.75	4.17	3.83	4.66	50.7	295.3	6.7
4.20	4.84	4.73	4.17	4.00	4.49	50.8	297.4	6.9
4.40	4.65	4.73	4.18	4.18	4.30	50.8	299.5	7.2
4.60	4.44	4.73	4.17	4.37	4.12	50.8	301.7	7.5
4.80	4.23	4.75	4.17	4.56	3.93	50.8	304.0	7.8
5.00	4.00	4.77	4.16	4.76	3.74	50.6	306.3	8.1
5.20	3.76	4.81	4.14	4.97	3.55	50.5	308.7	8.4
5.40	3.51	4.87	4.12	5.18	3.36	50.2	311.3	8.7
5.60	3.23	4.94	4.09	5.41	3.16	49.9	314.0	9.1
5.80	2.93	5.05	4.05	5.65	2.96	49.4	317.0	9.4
6.00	2.59	5.19	3.99	5.91	2.76	48.8	320.3	9.8
6.20	2.17	5.41	3.90	6.20	2.56	47.9	324.5	10.3
6.00	0.49	7.29	3.11	6.78	2.76	40.0	344.1	12.0

Table B.1: Kinematics for the N1-E2 space-star detector pair in the region where data were taken. This table was produced using the experimentally measured central detector angles $\theta_n = 51.4°$, $\phi_n = 119.5°$, $\theta_p = 52.3°$, $\phi_n = 0°$. Kinematic parameters pertaining the the undetected neutron are labeled with the subscript, u.

N2-E1 Space-Star Kinematics								
Laboratory Energy (MeV)			Relative Energy (MeV)			Undet. Neutron Lab Angle (°)		S (MeV)
E_p	E_n	E_u	E_{pn}	E_{pu}	E_{nu}	θ_u	ϕ_u	S
1.00	6.51	6.26	3.56	2.33	6.77	44.2	277.6	3.3
1.20	6.55	6.03	3.66	2.29	6.71	45.2	275.3	3.5
1.40	6.55	5.82	3.74	2.29	6.63	46.0	273.0	3.7
1.60	6.53	5.64	3.81	2.31	6.54	46.8	270.9	3.9
1.80	6.49	5.49	3.88	2.36	6.43	47.5	271.2	4.1
2.00	6.43	5.35	3.93	2.42	6.31	48.1	273.3	4.3
2.20	6.35	5.23	3.98	2.50	6.18	48.6	275.3	4.5
2.40	6.26	5.12	4.03	2.59	6.05	49.1	277.3	4.8
2.60	6.16	5.02	4.06	2.69	5.90	49.5	279.3	5.0
2.80	6.04	4.93	4.10	2.80	5.76	49.9	281.3	5.2
3.00	5.92	4.86	4.13	2.93	5.60	50.2	283.2	5.5
3.20	5.79	4.79	4.16	3.06	5.45	50.5	285.2	5.7
3.40	5.64	4.73	4.18	3.20	5.28	50.8	287.2	5.9
3.60	5.49	4.68	4.20	3.34	5.12	51.0	289.2	6.2
3.80	5.33	4.64	4.22	3.50	4.95	51.2	291.2	6.4
4.00	5.17	4.61	4.23	3.66	4.77	51.3	293.2	6.7
4.20	4.99	4.58	4.24	3.82	4.60	51.4	295.2	7.0
4.40	4.81	4.57	4.24	4.00	4.42	51.5	297.3	7.2
4.60	4.61	4.56	4.25	4.18	4.24	51.5	299.5	7.5
4.80	4.41	4.56	4.25	4.36	4.05	51.5	301.6	7.8
5.00	4.20	4.58	4.24	4.55	3.86	51.5	303.9	8.1
5.20	3.98	4.60	4.23	4.75	3.68	51.4	306.2	8.4
5.40	3.74	4.64	4.22	4.96	3.48	51.2	308.6	8.7
5.60	3.49	4.69	4.20	5.17	3.29	51.0	311.2	9.0
5.80	3.22	4.76	4.17	5.39	3.10	50.6	313.9	9.4
6.00	2.92	4.85	4.13	5.63	2.90	50.2	316.8	9.7
6.20	2.59	4.99	4.08	5.88	2.70	49.6	320.2	10.1
6.40	2.18	5.19	4.00	6.16	2.50	48.7	324.2	10.6
6.60	1.50	5.67	3.81	6.56	2.30	46.6	331.4	11.3

Table B.2: Kinematics for the N2-E1 space-star detector pair in the region where data were taken. This table was produced using the experimentally measured central detector angles $\theta_n = 51.7°$, $\phi_n = 59.7°$, $\theta_p = 51.3°$, $\phi_n = 180°$. Kinematic parameters pertaining the the undetected neutron are labeled with the subscript, u.

N3-E2 Coplanar Star Kinematics								
Laboratory Energy (MeV)			Relative Energy (MeV)			Undet. Neutron Lab Angle (°)		S (MeV)
E_p	E_n	E_u	E_{pn}	E_{pu}	E_{nu}	θ_u	ϕ_u	S
2.00	11.75	0.02	5.22	1.21	6.23	30.4	180.0	3.0
2.20	11.53	0.04	5.14	1.41	6.10	44.7	180.0	3.3
2.40	11.31	0.06	5.07	1.62	5.96	53.3	180.0	3.6
2.60	11.08	0.09	5.00	1.84	5.82	59.2	180.0	3.9
2.80	10.85	0.13	4.94	2.06	5.67	63.6	180.0	4.2
3.00	10.60	0.17	4.87	2.28	5.51	67.0	180.0	4.5
3.20	10.36	0.22	4.81	2.50	5.35	69.9	180.0	4.9
3.40	10.11	0.27	4.75	2.73	5.18	72.4	180.0	5.2
3.60	9.85	0.32	4.69	2.96	5.01	74.6	180.0	5.5
3.80	9.59	0.38	4.63	3.19	4.84	76.6	180.0	5.8
4.00	9.33	0.45	4.58	3.42	4.66	78.5	180.0	6.2
4.20	9.06	0.51	4.52	3.65	4.49	80.3	180.0	6.5
4.40	8.79	0.59	4.47	3.89	4.30	82.0	180.0	6.8
4.60	8.51	0.66	4.41	4.13	4.12	83.6	180.0	7.2
4.80	8.23	0.75	4.36	4.36	3.93	85.2	180.0	7.5
5.00	7.94	0.84	4.31	4.60	3.74	86.8	180.0	7.9
5.20	7.65	0.93	4.27	4.84	3.55	88.3	180.0	8.2
5.40	7.34	1.03	4.22	5.08	3.36	89.8	180.0	8.6
5.60	7.04	1.14	4.17	5.33	3.16	88.6	180.0	9.0
5.80	6.72	1.25	4.13	5.57	2.96	87.1	180.0	9.3
6.00	6.40	1.38	4.08	5.81	2.76	85.5	180.0	9.7
6.20	6.07	1.51	4.04	6.06	2.56	83.9	180.0	10.1
6.40	5.72	1.66	3.99	6.31	2.36	82.2	180.0	10.5
6.60	5.36	1.82	3.95	6.56	2.16	80.4	180.0	10.9
6.80	4.98	2.00	3.90	6.81	1.95	78.6	180.0	11.4
7.00	4.57	2.20	3.85	7.06	1.74	76.5	180.0	11.8
7.20	4.13	2.45	3.80	7.32	1.54	74.3	180.0	12.3
7.40	3.62	2.75	3.74	7.59	1.33	71.6	180.0	12.8
7.60	2.98	3.19	3.66	7.88	1.12	68.0	180.0	13.5
7.40	0.96	5.42	3.27	8.06	1.33	52.9	180.0	15.5

Table B.3: Kinematics for the N3-E2 coplanar star detector pair in the region where data were taken. This table was produced using the experimentally measured central detector angles $\theta_n = 17.7°$, $\phi_n = 180°$, $\theta_p = 52.3°$, $\phi_n = 0°$. Kinematic parameters pertaining the the undetected neutron are labeled with the subscript, u.

N4-E1 Coplanar Star Kinematics								
Laboratory Energy (MeV)			Relative Energy (MeV)			Undet. Neutron Lab Angle (°)		S (MeV)
E_p	E_n	E_u	E_{pn}	E_{pu}	E_{nu}	θ_u	ϕ_u	S
2.00	11.76	0.02	5.22	1.13	6.31	1.8	0.0	3.0
2.20	11.55	0.03	5.15	1.33	6.18	24.9	0.0	3.3
2.40	11.33	0.04	5.08	1.53	6.05	39.5	0.0	3.6
2.60	11.11	0.06	5.02	1.74	5.90	48.9	0.0	3.9
2.80	10.88	0.09	4.95	1.95	5.76	55.4	0.0	4.2
3.00	10.65	0.12	4.89	2.16	5.60	60.3	0.0	4.5
3.20	10.41	0.16	4.83	2.38	5.45	64.2	0.0	4.8
3.40	10.17	0.20	4.77	2.60	5.28	67.4	0.0	5.2
3.60	9.92	0.25	4.72	2.82	5.12	70.1	0.0	5.5
3.80	9.67	0.30	4.66	3.05	4.95	72.6	0.0	5.8
4.00	9.42	0.36	4.61	3.28	4.77	74.8	0.0	6.1
4.20	9.16	0.42	4.56	3.50	4.60	76.8	0.0	6.4
4.40	8.89	0.48	4.51	3.73	4.42	78.7	0.0	6.8
4.60	8.62	0.55	4.46	3.97	4.24	80.5	0.0	7.1
4.80	8.35	0.63	4.41	4.20	4.05	82.2	0.0	7.5
5.00	8.07	0.70	4.36	4.43	3.86	83.9	0.0	7.8
5.20	7.79	0.79	4.32	4.67	3.68	85.6	0.0	8.1
5.40	7.50	0.88	4.27	4.90	3.48	87.2	0.0	8.5
5.60	7.20	0.97	4.23	5.14	3.29	88.8	0.0	8.9
5.80	6.90	1.08	4.19	5.38	3.10	89.6	0.0	9.2
6.00	6.59	1.19	4.14	5.62	2.90	88.0	0.0	9.6
6.20	6.27	1.31	4.10	5.86	2.70	86.4	0.0	10.0
6.40	5.94	1.44	4.06	6.10	2.50	84.7	0.0	10.3
6.60	5.60	1.58	4.02	6.34	2.30	83.0	0.0	10.7
6.80	5.24	1.73	3.98	6.59	2.09	81.2	0.0	11.2
7.00	4.86	1.91	3.94	6.83	1.89	79.3	0.0	11.6
7.20	4.46	2.11	3.89	7.08	1.68	77.2	0.0	12.0
7.40	4.02	2.35	3.85	7.34	1.48	74.9	0.0	12.5
7.60	3.52	2.65	3.79	7.60	1.27	72.2	0.0	13.0
7.80	2.88	3.10	3.72	7.88	1.06	68.4	0.0	13.7
7.60	0.94	5.23	3.36	8.04	1.27	53.6	0.0	15.7

Table B.4: Kinematics for the N4-E1 coplanar star detector pair in the region where data were taken. This table was produced using the experimentally measured central detector angles $\theta_n = 18.7°$, $\phi_n = 0°$, $\theta_p = 51.3°$, $\phi_n = 180°$. Kinematic parameters pertaining the the undetected neutron are labeled with the subscript, u.

C Neutron Detector Efficiencies

The efficiencies of the neutron detectors used in this experiment were calibrated previously at TUNL using neutrons produced by the spontaneous fission of ^{252}Cf as the $^{2}H(d,n)^{3}He$ reaction [Gon98, Sal98]. These detectors were four out of a stock of at least twelve essentially identical liquid scintillator detectors produced by the Bicron Corporation and held at TUNL. One of the detectors from this stock was calibrated at the Physikalisch-Technische Bundesanstalt (PTB) in Braunschweig, Germany [Gon98]. The PTB group then modeled the characteristics of this detector using the Monte-Carlo simulations, NRESP7 and NEFF7 [Die82]. This code reproduced the measured efficiency of this detector within 1% statistical fluctuations. The efficiency simulations for this detector using various Cs-biases are shown in Figure C.1. The remaining detectors which were calibrated at TUNL required a normalization factor to bring them in line with the PTB simulation. These normalization factors were independent of the Cs-bias used. Table C.1 gives these normalization factors for the detectors used in the current experiment. A $\frac{1}{2}$Cs-bias was applied to all detectors. Table C.2 gives the simulated neutron detector efficiencies as a function of neutron energy for a $\frac{1}{2}$Cs-bias. Please note that no normalization factor has been applied to the values in this table.

Detector	Number	PTB Normalization
N1	12	0.975
N2	8	0.975
N3	11	0.975
N4	7	0.950

Table C.1: Normalization factors applied to the PTB simulated neutron detector efficiencies for the detectors used. The Bicron neutron detectors used at TUNL have numbers associated with them to keep track of which were used for what purposes. This is the meaning of the second column.

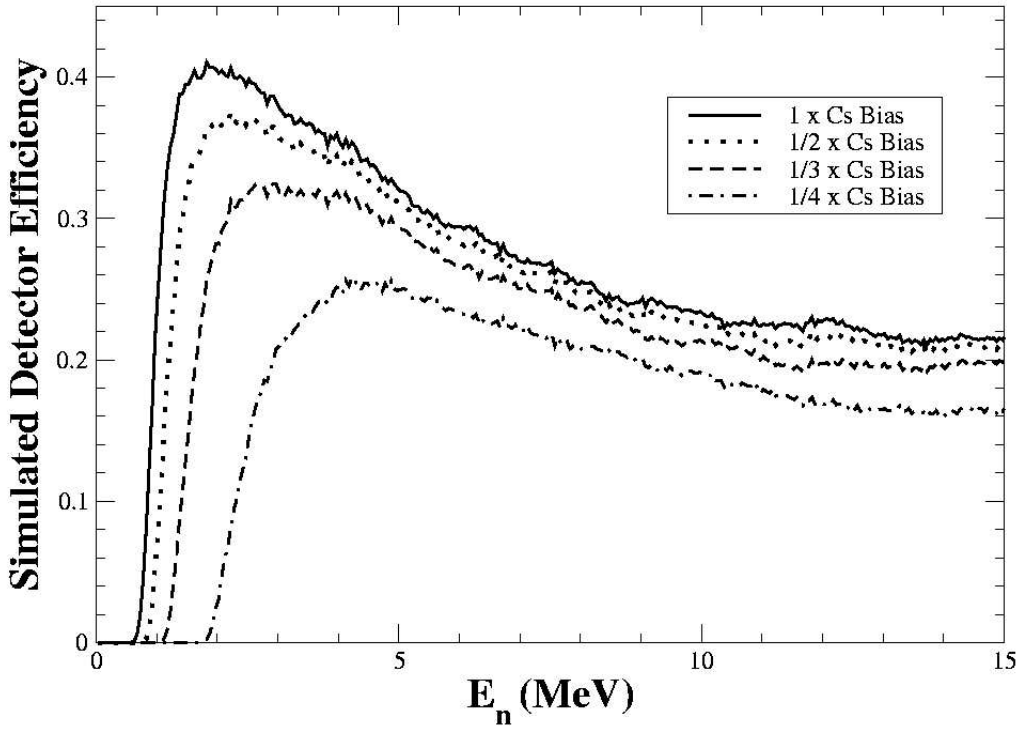

Figure C.1: Comparison of neutron detector efficiencies simulated using the PTB Monte-Carlo code, NEFF7 [Die82], for different pulse-height thresholds.

Neutron Energy	Detector Efficiency	Neutron Energy	Detector Efficiency	Neutron Energy	Detector Efficiency
0.90	0.0000	3.90	0.3166	7.00	0.2503
1.00	0.0000	4.00	0.3168	7.20	0.2493
1.10	0.0019	4.10	0.3153	7.40	0.2481
1.20	0.0156	4.20	0.3147	7.60	0.2442
1.30	0.0503	4.30	0.3131	7.80	0.2408
1.40	0.0964	4.40	0.3065	8.00	0.2362
1.50	0.1376	4.50	0.3069	8.20	0.2369
1.60	0.1822	4.60	0.3055	8.40	0.2278
1.70	0.2157	4.70	0.2986	8.60	0.2276
1.80	0.2469	4.80	0.2982	8.80	0.2221
1.90	0.2690	4.90	0.2980	9.00	0.2202
2.00	0.2818	5.00	0.2935	9.20	0.2150
2.10	0.2935	5.10	0.2915	9.40	0.2131
2.20	0.3055	5.20	0.2859	9.60	0.2124
2.30	0.3079	5.30	0.2837	9.80	0.2132
2.40	0.3130	5.40	0.2806	10.00	0.2134
2.50	0.3163	5.50	0.2804	10.20	0.2122
2.60	0.3222	5.60	0.2774	10.40	0.2082
2.70	0.3205	5.70	0.2728	10.60	0.2084
2.80	0.3187	5.80	0.2701	10.80	0.2044
2.90	0.3235	5.90	0.2679	11.00	0.2011
3.00	0.3214	6.00	0.2669	11.20	0.1981
3.10	0.3188	6.10	0.2657	11.40	0.1964
3.20	0.3199	6.20	0.2649	11.60	0.1945
3.30	0.3157	6.30	0.2612	11.80	0.1977
3.40	0.3183	6.40	0.2597	12.00	0.1974
3.50	0.3184	6.50	0.2573	12.20	0.1984
3.60	0.3166	6.60	0.2587	12.40	0.1966
3.70	0.3182	6.70	0.2564	12.60	0.1967
3.80	0.3131	6.80	0.2540	12.80	0.1952

Table C.2: Simulated neutron detector efficiency calculated using the PTB Monte-Carlo Code for a pulse height threshold of $\frac{1}{2}$xCs.

D Scattering Length

The scattering length, a is a parameter which is used to describe extremely low energy scattering from a short range potential. At these low energies, the wavelength of the particle will be much larger than the range of the potential; thus any structure in this potential will not be resolved and the scattered wavefunction may be well approximated a spherically symmetric outgoing wave ($l = 0$). In the limit of zero-energy scattering, outside the range of the potential, R, the Schrödinger equation satisfies:

$$\frac{d^2u}{dr^2} = 0. \tag{D.1}$$

The solution to this equation is a simple straight line:

$$u(r) = c(r - a), \tag{D.2}$$

where c is a constant and the scattering length, a, is defined as the radial intercept of this line. This intercept is governed by the magnitude and slope of the wavefunction just inside the range of the potential. The possible inner wavefunctions may be grouped into three general classes, as shown in Figure D.1. The first is a repulsive potential where the slope of the outside wavefunction must be positive and the value of the scattering length may take values between 0 and R as the strength of the potential is increased. The second case is an attractive potential. Here the slope of the outside wavefunction will still be positive, however the intercept will take negative values. As the strength of the attractive potential is increased, eventually a bound state will form. This is the third case where the slope of the outside wavefunction becomes negative and a must take positive values larger than R (a larger a means a more weakly bound state). The scattering length is related to the S_0 phase shift, δ_0, as follows:

$$\lim_{k\to 0} k \cot \delta_0 = -\frac{1}{a}, \tag{D.3}$$

and to the total cross section as $k \to 0$ by:

$$\sigma = 4\pi a^2 \tag{D.4}$$

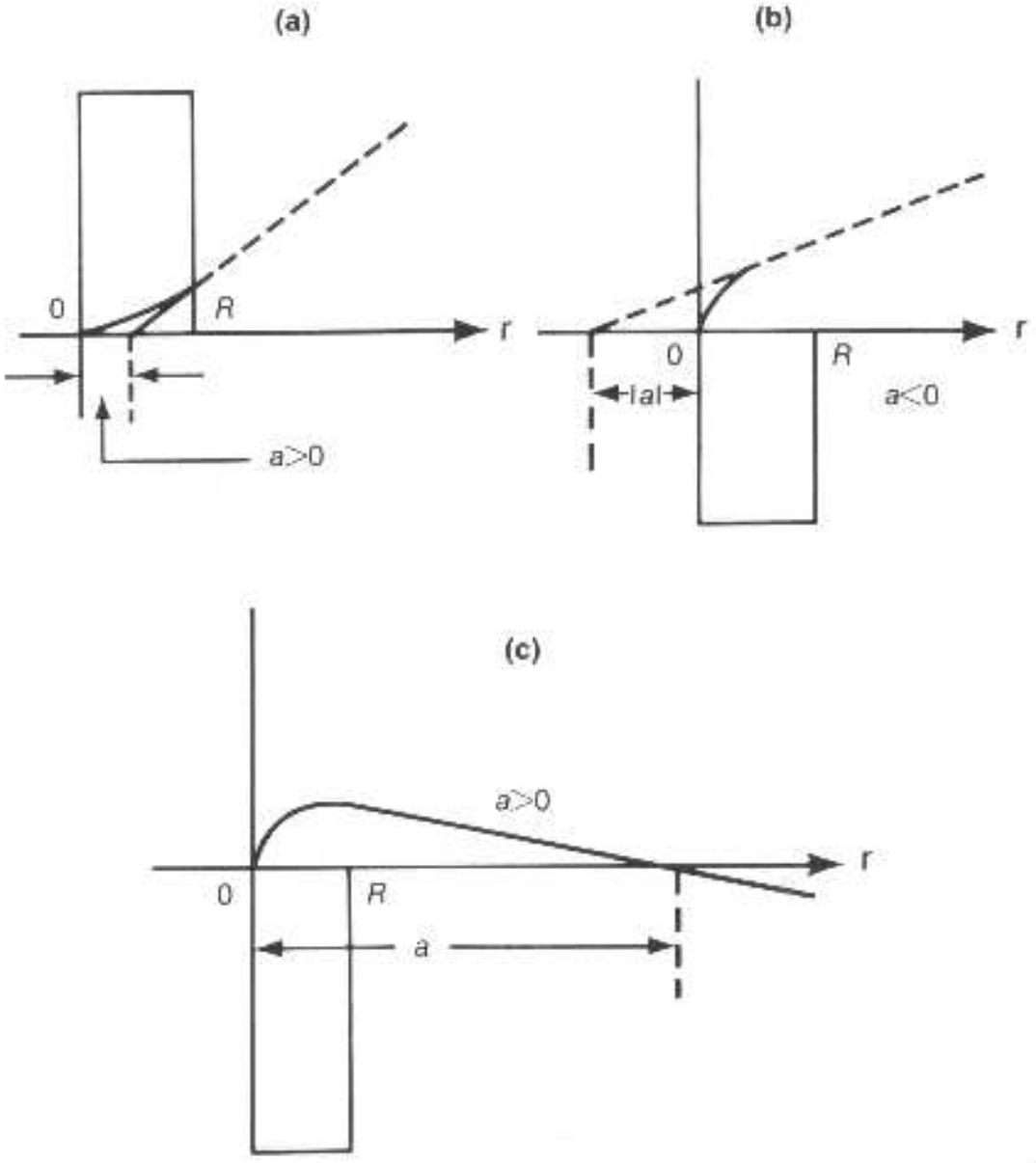

Figure D.1: Illustation of the scattering length, a. These graphs show the radial wavefunction, $u(r)$ for a particle under the influence of a square well potential of range R in the limit of zero-energy scattering. The three graphs show the results for (a) a repulsive potential, (b) an attractive potential, and (c) a strong attractive potential. The scattering length is the radial intercept of the line tangent to the wavefunction at the range of the potential [Sak94].

E Neutron Beam Characterization

The neutron beam used in this project was characterized by a series of experiments. The energy and spatial distributions of neutrons were measured and used in data analysis. Energy distributions were measured for nominal beam energies of 16.0 and 19.0 MeV. The higher energy was used in the analysis of a parallel *nd*-breakup measurement. The deuteron beam energy at the center of the gas cell was 13.15 MeV to produce 16.0 MeV neutrons and 16.33 MeV for 19.0 MeV neutrons. The reaction, ^{2}H(d,n)^{3}He (Q=+3.3 MeV), was used to produce the "prompt" neutrons. The beam also contained low energy background neutrons from the reactions, ^{2}H(d,n)dp (Q=-2.2 MeV) and ^{2}H(d,n)ppn (Q=-4.4 MeV), as well as deuteron breakup on the gold beam stop. There is an additional source of neutrons which populate the valley between the low energy breakups and the higher energy prompt peak arising from ^{2}H(d,n)^{3}He on deuterons implanted in the beam stop. All neutrons in the beam with energies less than 15.66 MeV are referred to as "source breakup" neutron in this thesis.

To determine the energy distribution of the neutron beam, an organic liquid scintillator with a cylindrical volume (5.08 cm diameter, 5.08 cm depth) was placed in the neutron beam at a center-to-center distance of 375.7 cm from the neutron production cell. The deuteron beam was "chopped and bunched" [How84] at a rate of 78.125 kHz into packets with a width of ≈3 ns. The pulsed beam allowed ToF measurement of the neutron energies using a time-to-amplitude (TAC) converter with the neutron detector pulse as its "start" and the signal from a capacitive pickoff unit located just before the gas cell as its "stop." The γ-peak in the ToF spectrum was used as a known reference time. However a small delay had to be added to the γ-ray ToF since most γ-rays were produced in the gold beam stop, but the neutrons were produced on average in the middle of the gas column. The delay was calculated as the time required for a deuteron to traverse the second half of the gas cell. The deuteron energy three-fourths of the way through the cell was used in this calculation as shown in Equation E.2. Thus the following formula was used to determine the neutron ToF:

$$t_n = t_\gamma + t_{delay} + (Ch_\gamma - Ch_n) * \left(0.1726 \ \frac{\text{ns}}{\text{ch}}\right), \tag{E.1}$$

where,

$$t_{delay} = (3.57 \text{ cm}) \cdot \sqrt{\frac{m_d}{2E_d}} \tag{E.2}$$

with m_d and E_d expressed in units of Mev/c^2 and MeV, respectively, and c=30 cm/ns. Data were first taken with 7.76 atm of D_2 in the gas cell, just as in the main experiment. The gas cell was then flushed and filled with 7.76 atm of ^{4}He. Data was taken with 0.22 atm of ^{4}He

in the gas cell as well. The results of these three types of runs are shown in Figure E.1. The runs with ^{4}He were used to determine which parts of the neutron energy spectrum arose from interactions in the gold beamstop and which were from ^{2}H(d,n) reactions. However, there are additional neutron producing reactions in the ^{4}He gas which influence these spectra. The reaction, ^{4}He(d,n)^{5}Li (Q=-4.187), produces the large low-energy peak seen in the 7.76 atm spectrum. The reaction, ^{4}He(d,p)^{5}He, followed by the decay, $^5\text{He} \rightarrow \text{n} + \alpha$, produces the slight enhancement seen at ≈5 MeV below the prompt peaks in Figure E.1.

The width of the prompt neutron peaks determined by the ToF measurements is not representative of the actual beam energy distribution. Instead this width is determined by the ≈3 ns width of the pulsed deuteron beam packets. A better estimation of the width of this peak may be obtained by calculating the deuteron beam energy loss as it passes through the deuterium gas column in the gas cell. This method provides a width of 0.34(0.28) MeV for the prompt 16.0(19.0) MeV neutron peak. The measured prompt neutron peak was integrated beginning at 12.0 MeV using the 7.76 atm ^{4}He spectum as background. These counts were then placed in a rectangular distribution with a width defined by the beam energy loss in the neutron production cell as shown in Figure E.2.

To determine the spatial distribution of the neutron beam, a thin rectangular plastic scintillator (3×25 mm facing the beam) was attached to a translation stage which scanned it across the beam in 3 mm steps. Horizontal and vertical scans were taken before and after the chamber separated by 83.2 cm along the beam axis. The detector anode signal was fed into a constant-fraction discriminator (CFD) with a threshold set just above the γ-ray background emanating from the gas cell. The CFD signal as well as the beam-current integration (BCI) were fed into a scalar counter module set to count for 20 s at each location in the scan. The counts per unit BCI were then calculated for each scan position. The results of these measurements are shown in Figure E.3. Analysis of these results show the beam to be tilted 1.1° beam-right and 0.35° up relative to the zero degree axis of the experimental setup.

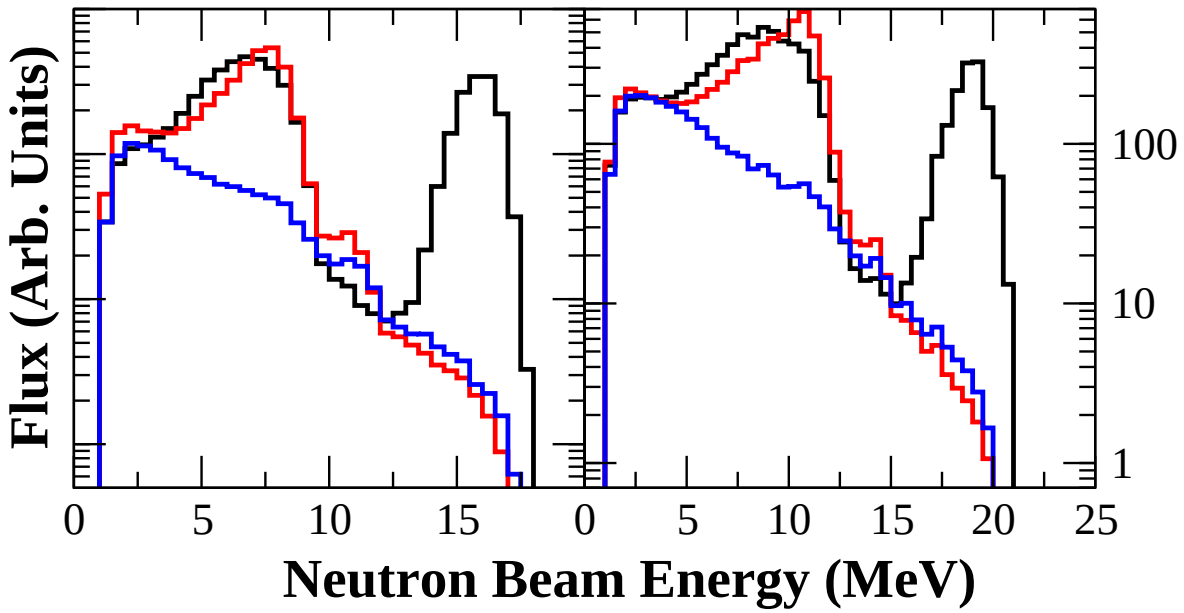

Figure E.1: Measured neutron beam spectra. The graph on the left(right) shows the 16.0(19.0) MeV results. The black histograms correspond to the gas cell filled with deuterium. The red and blue histograms are the results from the 7.76 and 0.22 atm ^{4}He measurements, respectively. The spectra have been weighted by BCI and neutron detector efficiency.

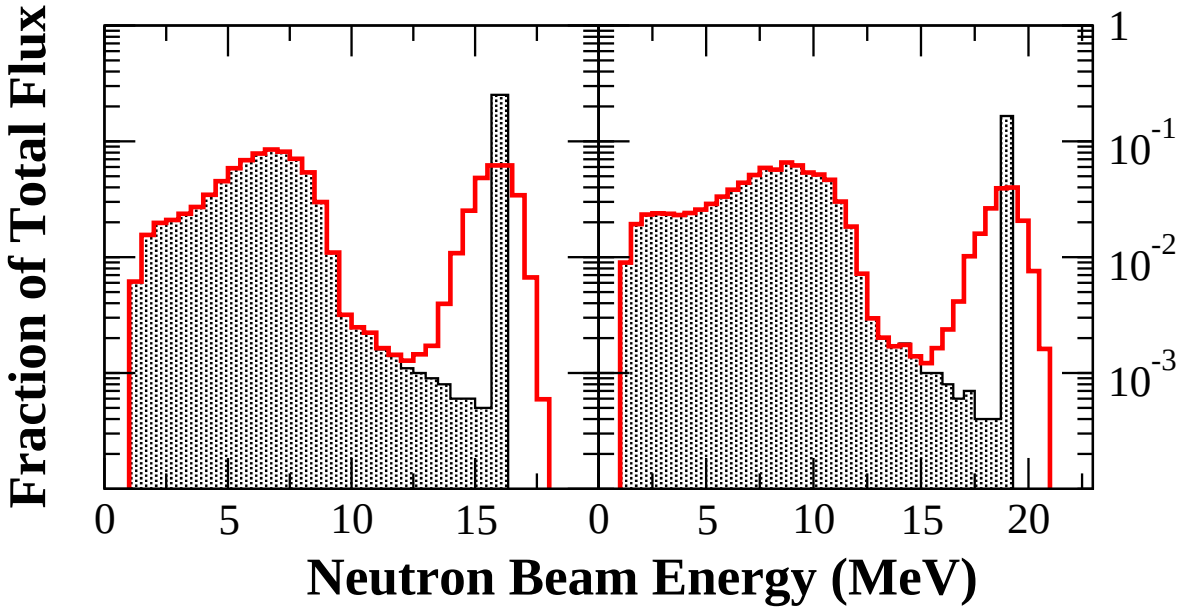

Figure E.2: Neutron beam energy distribution with the width of the prompt peak estimated by deuteron energy loss in the gas cell (black) compared with the measured results (red) where the width is determined by the pulsed deuteron beam packet length. The graph on the left(right) shows the 16.0(19.0) MeV results.

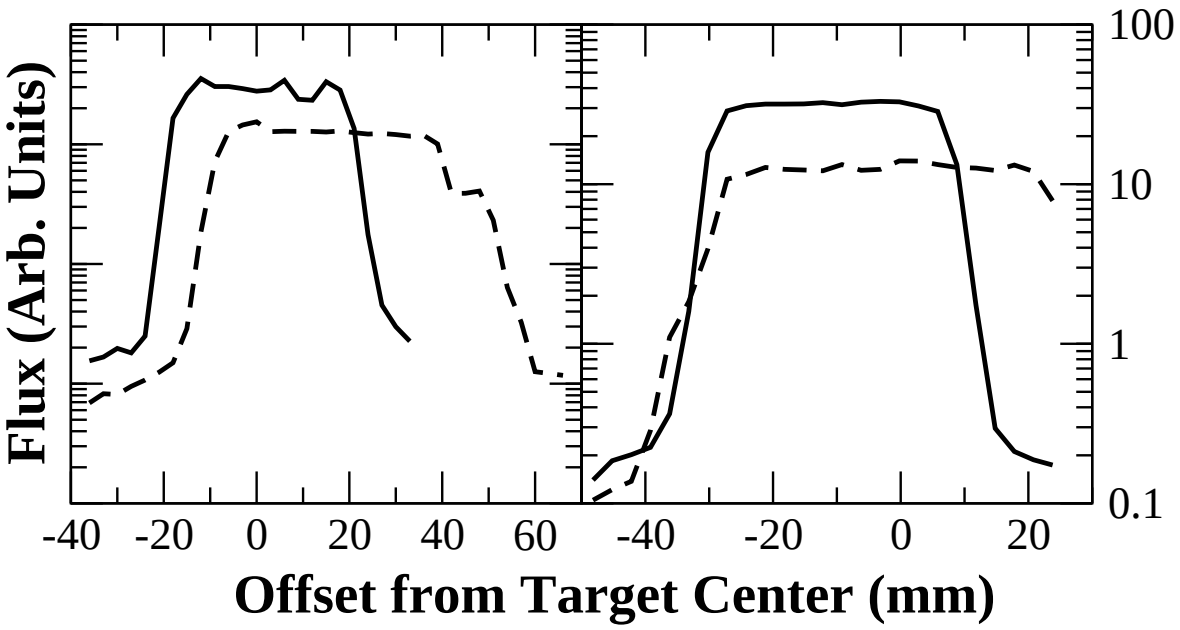

Figure E.3: Neutron Beam Spatial Distribution. The graph on the left(right) describes the horizontal(vertical) distribution. The solid lines are the distributions just after the collimator; and the dashed lines are just after the chamber. The offsets in the graphs are with respect to vertical and horizontal planes which contain the target center where positive offsets correspond to up and beam-right.

F Survey of the Experimental Setup

Upon disassembling the experimental setup, the positions of the target and detectors were surveyed. This section will outline the techniques used in and results of this survey. The target chamber and detectors were all mounted above a horizontal table which was marked with a zero degree axis. This axis supposedly denoted the beam direction, however it was found that the beam actually propagated 1.1° to the right of this axis.

The height of the target above the table was found to be 44.6±0.2 cm above the table. This distance was obtained by simply measuring the height of the target rod which was mounted horizontally as well as could be measured. Before the target chamber was removed, a plumb bob was suspended directly above the center of the target. Once the target chamber was removed the plumb bob was lowered from its fixed suspension point to the level of the table. It lined up with the zero degree line marked on the table (±0.1 cm). The position of the target along this line was marked on the table.

The distances between the neutron detectors and the target were determined slightly differently for the CST and SST detectors. The out-of-plane SST detectors had a direct line-of-sight to the target when the chamber dome was removed. A string was taped to the center of the detector face and the distance to the target was marked on the string. The length along the string was then determined with a tape measure. The thin tantalum exit window impeded the line-of-sight for the CST neutron detectors. The delicate nature of this window and the difficulty in obtaining a leak tight seal required it to remain in place. Two rulers were taped vertically to the target position and the center of the detector face. The horizontal distance between these rulers was then determined using a tape measure. All neutron detector distance measurements were repeated three times and agreed to better than ±2 mm. The distances between the target and the ΔE detectors were measured directly with a ruler and found to be 8.0±0.2 cm. The distance between the ΔE and E detectors was measured by inserting a rod down the charged particle arm until it touched the face of the thick plastic scintillator and marking the location of the ΔE detector. The rod was then measured using a tape measure. Both E-ΔE pairs were separated by 61.0±0.02 cm.

The height of the detectors above the table were determined using a tape measure. All measurements are with respect to the center of the detector faces. The E detectors were at the same height as the target, 44.6±0.2 cm. The CST neutron detectors were just slightly lower at 44.5±0.2 cm. The out-of-plane SST detectors were slightly different from one another at heights of 92.4±0.2 cm and 92.1±0.2 cm for the N1 and N2 detectors, respectively.

Detector angles were found by hanging plumb bobs from the center of the detector faces. The projection of the central detector position onto the plane of the table was then marked. A t-square was then used to project this position onto the nominal 0°-axis marked on the table. This formed a right-triangle with vertices at the target position, the detector position, and the projection of the detector position onto the 0°-axis. The lengths of the three sides of this triangle measured and used to determine the scattering angle in the horizontal plane. The angle was found using the sine, cosine, and tangent, and the three results were averaged. This was sufficient to determine the scattering angle for the detectors located in the horizontal scattering plane; E_1, E_2, N_3, and $N4$. The out-of-plane detectors, N_1 and N_2, required one additional parameter, their height above the horizontal scattering plane, to determine their scattering angle trigonometrically.

Bibliography

[Arn83] R. Arndt, L. Roper, R. Bryan, R. Clark, B. VerWest, and P. Signell, "Nucleon-Nucleon Partial Wave Analysis to 1 GeV", Physical Review **D28**, 97 (1983).

[Ber08] V. Bernard, E. Epelbaum, H. Krebs, and Ulf.-G. Meißner, "Subleading Contributions to the Chiral Three-Nucleon Force: Long-Range Terms", Physical Review **C77**, 064004 (2008).

[Ble39] J. Blewett, "The Properties of Oxide-Coated Cathodes. II", Journal of Applied Physics **10**, 831 (1939).

[Bru53] K. Brueckner and K. Watson, "Nuclear Forces in Pseudoscalar Meson Theory", Physical Review **92**, 1023 (1953).

[Car83] J. Carlson, V.R. Pandharipande, and R.B. Wiringa, "Three-Nucleon Interaction in a 3-, 4- and ∞-Body Systems", Nuclear Physics **A401**, 59 (1983).

[Coe83] H. Coelho, T. Das, and M.R. Robliotta, "Two-Pion-Exchange Three-Nucleon Force and the ^{3}H and ^{3}He Nuclei", Physical Review **C28**, 1812 (1983).

[Coo79] S.A. Coon, M. Scadron, P. McNamee, B. Barrett, D. Blatt, and B. McKellar, "Two-Pion-Exchange Three-Nucleon Potential and Nuclear Matter", Nuclear Physics **A317**, 242 (1979).

[Coo81] S.A. Coon and W. Glöckle, "Two-Pion Exchange Three-Nucleon Potential: Partial Wave Analysis in Momentum Space", Physical Review **C23**, 1790 (1981).

[Coo01] S.A. Coon and H.K. Han, "Reworking the Tucson-Melborne Three-Nucleon Potential", Few-Body Systems **30**, 131 (2001).

[Cro01] A.S. Crowell, "Cross-Section Measurements of Star Configurations in Neutron-Deuteron Breakup at 16.0 MeV", Ph.D Thesis, Duke University (2001).

[Die82] G. Dietze and H. Klein, "NRESP4 and NEFFP4 Monte Carlo Codes for the Calculation of Neutron Response Functions and Detection Efficiencies for NE213 Scintillation Detectors", Physikalisch-Technische Bundesanstalt, Bundensalle 100, W-330 Braunschweig (1982).

[Dro78] M. Drosg, "Unified Absolute Differential Cross Sections for Neutron Production by the Hydrogen Isotopes for Charged Particle Energies Between 6 and 17 MeV", Nuclear Science and Engineering **67**, 190 (1978).

[Epe02] E. Epelbaum et al., "Three-Nucleon Forces from Chiral Effective Field Theory", Physical Review **C66**, 064001 (2002).

[Epe05] E. Epelbaum, W. Glöckle, and Ulf.-G. Meißner, "The Two-Nucleon System at Next-to-Next-to-Next-to-Leading Order", Nuclear Physics **A747**, 362 (2005).

[Epe06] E. Epelbaum, "Few-Nucleon Forces and Systems in Chiral Effective Field Theory", Progress in Particle and Nuclear Physics **57**, 654 (2006).

[Epe09] E. Epelbaum, H.-W. Hammer, and Ulf.-G. Meißner, "Modern Theory of Nuclear Forces", Reviews of Modern Physics **81**, 1773 (2009).

[Est04] J.H. Esterline et al., "Gamma-Ray Induced Two-Body Breakup of ^{3}He between $E_\gamma = 10$ MeV and 15 MeV", TUNL Progress Report **XLIII**, 110 (2004).

[Fad61] L. Faddeev, "Scattering Theory for a Three-Particle System", Journal of Experimental and Theoretical Physics (U.S.S.R.) **12**, 1014 (1961).

[Fuj57] J. Fujita and H. Miyazawa, "Pion Theory of Three-Body Forces", Progress of Theoretical Physics **17**, 360 (1957).

[Gar09] A. Gardestig, "Extracting the Neutron-Neutron Scattering Length - Recent Developments", Journal of Physics G: Nuclear and Particle Physics **36**, 053001 (2009).

[Geb93] K. Gebhardt et al., "Experimental and Theoretical Investigation of the ^{2}H(n,nnp) Reaction and of the Neutron-Neutron Scattering Length", Nuclear Physics **A561**, 232 (1993).

[Gla74] D. Glasgow et al., "Shielding for Fast Neutron Scattering Experiments of High Sensitivity", Nuclear Instruments and Methods **114**, 521 (1974).

[Glö96] W. Glöckle, H. Witała, D. Hüber, H. Kamada, and J. Golak, "The Three-Nucleon Continuum: Achievements, Challenges, and Applications", Physics Reports **274**, 107 (1996).

[Gon98] D. González Trotter, "Extraction of the $^1S_0$ Neutron-Neutron Scattering Length from a Kinematically-Complete N-D Breakup Experiment", Ph.D Thesis, Duke University (1998).

[Hüb97] D. Hüber, H. Kamada, H. Witała, and W. Glöckle, "How to Include a Three-Nucleon-Force into Faddeev Equations for the 3N Continuum: A New Form", Acta Physica Polonica **B28**, 1677 (1997).

[How84] C.R. Howell, "Neutron Scattering from ^{28}Si and ^{32}S: Cross Sections and Analyzing Powers from 8 to 40 MeV", Ph.D Thesis, Duke University (1984).

[How98] C.R. Howell et al., "Towards a Resolution of the Neutron-Neutron Scattering Length Issue", Physics Letters **B444**, 252 (1998).

[Huh00a] V. Huhn et al., "New Attempt to Determine the $n-n$ Scattering Length with the ${}^2H(n,np)n$ Reaction", Physical Review Letters **85**, 1190 (2000).

[Huh00b] V. Huhn et al., "New Investigation of the Neutron-Neutron and Neutron-Proton Final-State Interaction in the $n-d$ Breakup Reaction", Physical Review **C63**, R15 (2000).

[Jan66] J. Janni, "Calculations of Energy Loss, Range, Pathlength, Straggling, Multiple Scattering, (etc.)", U.S. Federal Clearinghouse **Technical Report No. 1AFWL-TR-65-150** (1966).

[Kam83] J. Kammeraad and L. Knutson, "On the Determination of the Deuteron Quadrupole Moment by Elastic Scattering of Polarized Deuterons", Journal of Physics G: Nuclear Physics **9**, L217 (1983).

[Kie08] A. Kievsky, S. Rosati, M. Viviani, L. Marcucci, and L. Girlanda, "A High-Precision Variational Approach to Three- and Four-Nucleon Bound and Zero-Energy Scattering States", Journal of Physics G: Nuclear Physics **35**, 063101 (2008).

[Kon10] E. Konobeevski, Y. M. Burmistrov, S. Zuyev, M. Mordovsky, and S. Potashev, "Determination of the ${}^1S_0$ Neutron-Neutron Scattering Length in the nd Breakup Reaction at Energies in the Range E_n=40-60 MeV", Physics of Atomic Nuclei **73**, 1302 (2010).

[Law65] G. P. Lawrence, R. K. Beauchamp, and J. L. McKibben, "Direct Extraction of Negative Ion Beams of Good Intensity from a Duoplasmatron", Nuclear Instruments and Methods **32**, 357 (1965).

[Leo94] W. Leo, "Techniques for Nuclear and Particle Physics Experiments", Springer-Verlag (1994).

[Lip50] B. Lippmann and J. Schwinger, "Variational Principles for Scattering Processes I", Physical Review **79**, 469 (1950).

[Mac89] R. Machleidt, "The Meson Theory of Nuclear Forces and Nuclear Structure", Advances in Nuclear Physics **19**, 189 (1989).

[Mac01a] R. Machleidt, "High-Precision, Charge-Dependent Bonn Nucleon-Nucleon Potential", Physical Review **C63**, 024001 (2001).

[Mac01b] R. Machleidt and I. Slaus, "The Nucleon-Nucleon Interaction", Journal of Physics G: Nuclear and Particle Physics **27**, R69 (2001).

[Mac05] R. Machleidt and D. Entem, "Recent Advances in the Theory of Nuclear Forces", Journal of Physics: Conference Series **20**, 77 (2005).

[Mac04] R. Macri, "Star-Configuration Cross-Section Measurements of Neutron-Induced Deuteron Breakup at 10.3 and 13.0 MeV", Ph.D Thesis, Duke University (2004).

[Nak10] K. Nakamura et al., "Particle Data Group: Summary Tables", Journal of Physics G: Nuclear and Particle Physics **37**, 075021 (2010).

[Nog03] A. Nogga et al., "Three-Nucleon Bound States Using Realistic Potential Models", Physical Review **C67**, 034004 (2003).

[Nol69] J. Nolen Jr. and J. Schiffer, "Coulomb Energies - An Anomaly in Nuclear Matter Radii", Physics Letters **29B**, 396 (1969).

[Oga67] S. Ogawa, S. Sawada, T. Ueda, W. Watari, and M. Yonezawa, "One-Boson-Exchange Model", Supplement of the Progress of Theoretical Physics **39**, 140 (1967).

[Pie01] S.C. Pieper, V.R. Pandharipande, R.B. Wiringa, and J. Carlson, "Realistic Model of Pion-Exchange Three-Nucleon Interactions", Physical Review **C64**, 014001 (2001).

[Pri47] H. Primakoff, "Long Range Tensor Forces and the Magnetic Moment of the Deuteron", Physical Review **72**, 118 (1947).

[Pud97] B.S. Pudliner, V.R. Pandharipande, J. Carlson, S.C. Pieper, and R.B. Wiringa, "Quantum Monte Carlo Calculations of Nuclei with A$\leq$7", Physical Review **C56**, 1720 (1997).

[Rua07] X.C. Ruan et al., "Experimental Study of Neutron-Neutron Quasifree Scattering in the *nd* Breakup Reaction at 25 MeV", Physical Review **C75**, 057001 (2007).

[Sak94] J.J. Sakurai, "Modern Quantum Mechanics Revised Edition", Addison-Wesley Publishing Company (1994).

[Sal98] F. Salinas Meneses, "Use of the $^1S_0$ Neutron-Deuteron Scattering Length as a Probe for Three-Nucleon Forces", Ph.D Thesis, Duke University (1998).

[Sel64] S. Seltzer and M. Berger, "Energy-Loss Straggling of Protons and Mesons Tabulation of the Vavilov Distribution", Nuclear Science Series Report: Studies in Penetration of Charged Particles in Matter **39**, 187 (1964).

[Set05] H.R. Setze et al., "Cross Section Measurement of Neutron-Deuteron Breakup at 13.0 MeV", Physical Review **C71**, 034006 (2005).

[Sie02] A. Siepe, J. Deng, V. Huhn, L. Wätzold, C. Weber, and W. von Witch, "Neutron-Proton and Neutron-Neutron Quasifree Scattering in the $n-d$ Breakup Reaction at 26 MeV", Physical Review **C65**, 034010 (2002).

[Ste89] M. Stephan et al., "Neutron-Induced Deuteron Breakup Cross Section at 10.3 MeV", Physical Review **C39**, 2133 (1989).

[Sto93] V.G.J. Stoks, R.A.M. Klomp, M.C.M. Rentmeester, and J.J. de Swart, "Partial-Wave Analysis of All Nucleon-Nucleon Scattering Data Below 350 MeV", Physical Review **C48**, 792 (1993).

[Sto94] V.G.J. Stoks, R.A.M. Klomp, C.P.F. Terheggen, and J.J. de Swart, "Construction of High-Quality NN Potential Models", Physical Review **C49**, 2950 (1994).

[Str89] J. Strate et al., "Differential Cross Section of the $^2H(n,nnp)$ Reaction at $E_n = 13$ MeV", Nuclear Physics **A501**, 51 (1989).

[Taj10] S. Tajima, Private Communications (2010).

[Tak51] M. Taketani, S. Nakamura, and M. Sasaki, "On the Method of the Theory of Nuclear Forces", Progress of Theoretical Physics **6**, 581 (1951).

[Tay97] J.R. Taylor, "An Introduction to Error Analysis", University Science Books , 106 (1997).

[Tor08] W. Tornow, J.H. Esterline, and G.J. Weisel, "Energy Dependence of the Three-Nucleon Analyzing Power Puzzle", Journal of Physics G: Nuclear and Particle Physics **35**, 125104 (2008).

[Wei79] S. Weinberg, "Phenomenological Lagrangians", Physica **96A**, 327 (1979).

[Wei91] S. Weinberg, "Effective Chiral Lagrangians for Nucleon-Pion Interactions and Nuclear Forces", Nuclear Physics **B363**, 3 (1991).

[Wig33] E. Wigner, "On the Mass Defect of Helium", Physical Review **43**, 252 (1933).

[Wir95] R.B. Wiringa, V.G.J. Stoks, and R. Schiavilla, "Accurate Nucleon-Nucleon Potential with Charge-Independence Breaking", Physical Review **C51**, 38 (1995).

[Wit89] H. Witała, D. Hüber, and T. Cornelius, "Rigorous Faddeev Calculations for Elastic Neutron-Deuteron Scattering Around 8 MeV c.m. Energy", Nuclear Physics **A491**, 157 (1989).

[Wit10a] H. Witała, Private Communication (2010).

[Wit10b] H. Witała and W. Glöckle, "On the Discrepancies in the Low-Energy Neutron-Deuteron Breakup", Journal of Physics G: Nuclear and Particle Physics **37**, 064003 (2010).

[Yuk35] H. Yukawa, "On the Interaction of Elementary Particles I.", Proceedings of the Physico-Mathematical Society of Japan **17**, 48 (1935).

[Zho01] Z. Zhou et al., "The Space Star Anomaly in *nd* Breakup at 25 MeV", Nuclear Physics **684**, 545C (2001).